AD-A154 375 PLASMA RADIATION SOURCES QUASI-ADIABATIC THEORY AND NUMERICAL MODELING IN..(U) JAYCOR ALEXANDRIA VA J U GUILLORY ET AL. 16 JUL 84 JAYCOR-J800-83-003 1/2

UNCLASSIFIED DNA-6304F DNA001-79-C-0189 F/G 20/9 NL

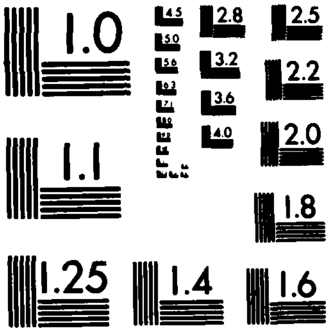
1.0
4.5
5.0
5.6
6.3
7.1
8.0
2.8
3.2
3.6
4.0
2.5
2.2
2.0
1.1
1.8
1.25
1.4
1.6

MICROCOPY RESOLUTION TEST CHART
NATIONAL BUREAU OF STANDARDS-1963-A

AD-E501681

②

AD-A154 375

DNA 6304F

PLASMA RADIATION SOURCES

Quasi-Adiabatic Theory and Numerical Modeling in the Electro-Diffusive Approximation

JAYCOR
205 South Whiting Street
Alexandria, Virginia 22304-3687

16 July 1984

Technical Report

CONTRACT No. DNA 001-79-C-0189

APPROVED FOR PUBLIC RELEASE;
DISTRIBUTION UNLIMITED.

THIS WORK WAS SPONSORED BY THE DEFENSE NUCLEAR AGENCY UNDER RDT&E RMSS CODE B323080464 T99QAXLA01482 H2590D.

Prepared for
Director
DEFENSE NUCLEAR AGENCY
Washington, DC 20305-1000

DTIC
S ELECTE D
JUN 3 1985
B

DTIC FILE COPY

85 03 29 015

Destroy this report when it is no longer needed. Do not return to sender.

PLEASE NOTIFY THE DEFENSE NUCLEAR AGENCY, ATTN: STTI, WASHINGTON, DC 20305-1000, IF YOUR ADDRESS IS INCORRECT, IF YOU WISH IT DELETED FROM THE DISTRIBUTION LIST, OR IF THE ADDRESSEE IS NO LONGER EMPLOYED BY YOUR ORGANIZATION.

UNCLASSIFIED

SECURITY CLASSIFICATION OF THIS PAGE (*When Data Entered*)

REPORT DOCUMENTATION PAGE		READ INSTRUCTIONS BEFORE COMPLETING FORM
1. REPORT NUMBER DNA 6304F	2. GOVT ACCESSION NO. AD-A154375	3. RECIPIENT'S CATALOG NUMBER
4. TITLE (*and Subtitle*) PLASMA RADIATION SOURCES Quasi-Adiabatic Theory and Numerical Modeling in the Electro-Diffusive Approximation		5. TYPE OF REPORT & PERIOD COVERED Technical Report
		6. PERFORMING ORG. REPORT NUMBER J800-83-003
7. AUTHOR(s) John U. Guillory Robert E. Terry		8. CONTRACT OR GRANT NUMBER(s) DNA 001-79-C-0189
9. PERFORMING ORGANIZATION NAME AND ADDRESS JAYCOR 205 South Whiting Street Alexandria, Virginia 22304-3687		10. PROGRAM ELEMENT, PROJECT, TASK AREA & WORK UNIT NUMBERS Task T99QAXLA-01482
11. CONTROLLING OFFICE NAME AND ADDRESS Director Defense Nuclear Agency Washington, DC 20305-1000		12. REPORT DATE 16 July 1984
		13. NUMBER OF PAGES 132
14. MONITORING AGENCY NAME & ADDRESS (*if different from Controlling Office*)		15. SECURITY CLASS (*of this report*) UNCLASSIFIED
		15a. DECLASSIFICATION/DOWNGRADING SCHEDULE N/A since UNCLASSIFIED

16. DISTRIBUTION STATEMENT (*of this Report*)

Approved for public release; distribution unlimited.

17. DISTRIBUTION STATEMENT (*of the abstract entered in Block 20, if different from Report*)

18. SUPPLEMENTARY NOTES

This work was sponsored by the Defense Nuclear Agency under RDT&E RMSS Code B323080464 T99QAXLA01482 H2590D.

19. KEY WORDS (*Continue on reverse side if necessary and identify by block number*)

Imploding Plasma
Radiation Source
Pinch
Annular Discharge

20. ABSTRACT (*Continue on reverse side if necessary and identify by block number*)

This report describes work done under DNA Contract 001-79-C-0189 from February 1982 to June 1983, and some more recent work. Part I includes treatments of a simple zero-D implosion code, analytic but very approximate scaling laws for radiation, and a discussion of preliminary work on nonlinear field penetration of plasma. Part II contains a discussion of electrodiffusive 1D modeling of annular plasma implosions. The thermoelectrical field, its role in field penetrations, the nonlocal constraints required in field diffusion (and some arising from field diffusion), flux limits and the acceleration process

20. ABSTRACT (Continued)

for annular plasmas are discussed.

TABLE OF CONTENTS

PART I

I. INTRODUCTION 3
II. DEVELOPMENT OF THE RUNIN CODE 8
  A. WIRES: EQUATIONS FOR THE IMPLOSION OF THE WIRE ARRAY - MODIFICATIONS AND UNDERLYING ASSUMPTIONS. 8
  B. BRIDGE: EQUATIONS FOR THE UNIFORM ANNULAR PLASMA IMPLOSION. 11
  C. NUMERICAL INTEGRATOR PACKAGE 12
  D. RADIATIVE LOSS AND OUTPUT TERMS FOR THE ANNULAR AND CYLINDRICAL PHASES 13
  E. CAVEATS TO THE RUNIN CODE 15
III. APPROXIMATE SCALING LAWS 16
  A. WIRE PLASMA PHASE OF ARRAY IMPLOSION 18
  B. ANNULAR PLASMA STAGE 22
  C. RADIATION SCALING AND DYNAMICS IN THE PINCH PHASE 26
  D. CAVEATS 46
  E. COMPARISON OF REQUIREMENTS FOR GENERATORS DRIVING RADIATION SOURCES AND FUSION TARGETS 49
IV. SIMPLIFIED NON-LINEAR FIELD DIFFUSION 52
  A. PROBLEM DEFINITION AND APPROXIMATIONS 52
  B. NUMERICAL SOLUTION 55
  C. INTERPRETATION OF SOLUTIONS 56
  D. CAVEATS TO THE FOREGOING NONLINEAR DIFFUSION STUDY 59
V. SUMMARY OF PART I 62
  RUNIN CODE SUMMARY 62
  A. WIRES 62
  B. BRIDGE 63
  C. SQUEEZE 63
  RADIATIVE SCALING LAWS SUMMARY 64
  REFERENCES FOR PART I 68
  ACKNOWLEDGEMENT 69

☑
☐
☐
Distribution/
Availability Codes
Dist | Avail and/or Special
A-1

TABLE OF CONTENTS
(CONTINUED)

PART II

I. OVERVIEW OF THE ELECTRODIFFUSIVE MHD MODEL FOR THE IMPLODING PLASMA RADIATOR 71

A. ARCHITECTURE OF THE IMPLOSION CODE 72

B. MILESTONES AND ROADBLOCKS 75

II. SELF-CONSISTENT CALCULATION OF THE MATERIAL DERIVATIVES (FLUIDOTS/TETDOTS) 79

A. STATEMENT OF THE PROBLEM 79

B. THE MAGNETIC FIELD COMPUTATION 82

C. APPLICATION OF THE CONSTRAINT RELATION . . . 86

D. PROCESSING SEQUENCE FOR THE MATERIAL DERIVATIVES: FLUIDOTS/TETDOTS 94

E. THE SPATIAL STRUCTURE OF CHANGE 97

III. THE INTEGRATION OF THE FLUID MESH TRAJECTORIES. 104

A. CONTINUOUSLY VARIABLE TIMESTEPS AND FILTER THEORY 104

B. RESPONSE, STABILITY AND ACCURACY 108

IV. SNOWPLOW FORMATION - THE BOOST PHASE 118

V SUMMARY OF PART II 126

REFERENCES FOR PART II 127

PART I

CHAPTER I

INTRODUCTION

This report describes modeling of imploding plasma radiation sources (at various levels of description) during the contract year 1982. The report is divided into two parts. Part I describes zero-D models, which use ordinary differential equations (and their numerical or approximate analytical solution) to describe the dynamics and radiation from imploding wire or gas-puff plasma, with the approximation that the plasmas are uniform. For completeness, Part I also includes a preliminary description of some results actually obtained at the beginning of the 1983 contract year.[1] These refer to first-order nonadiabatic corrections to formulas for radiation from quasi-adiabatic pinch plasmas.

Part I concludes with a report on analysis of a 1D idealized model for nonlinear field penetration into profile-invariant plasma where the conductivity (i.e., field diffusion rate) depends on field strength through Joule heating, etc.

Part II describes 1D MHD modeling (or more exactly, EMHD modeling, since the electric field E, rather than magnetic field, is explicitly advanced in the code), with related discoveries about the nonlinear physics and the numerical techniques for advancing the variables. Much of this code development has been carried out so as to be directly usable in 2D as well, although the 2D r-z code is not yet near completion.

---

[1] The contract reported on here and NRL Contract N00173-80-C-0202 have been merged into one new contract, DNA001-83-C-0204 covering 02-03-83 to 03-31-84.

The purpose of the formulations described in Part I is to provide semi-quantitative insight and understanding into the behavior and scaling of plasma radiation source behavior, using simplified model assumptions. The purpose of the code and physics described in Part II is to compute quantitatively the behavior of plasma radiation sources with adequate cylindrical symmetry and to provide the refinements and modifications to the simpler less quantitative scaling laws discussed in Part I, including now (e.g.,) the radial profiles and more detailed radiation transport which are omitted in Part I for simplicity.

A simple "scoping" code is discussed in Chapter II of Part I. In this code called RUNIN, the plasma motion, heating and current are described by a set of ordinary differential equations. The code follows three (or two) successive stages in the evolution of a wire array (or annular gas puff) discharge: the motion and expansion of individual wire plasmas until coalescence to an annulus, the motion of the annular plasma (with finite, time-dependent thickness, radius and temperature) until formation of a non-hollow pinch, and the compression of the assembled pinch once the annulus closes. In each stage the model plasma has uniform density and temperature. Radiation from the wire plasmas is assumed to be blackbody. The annular and pinch phases use blackbody-limited otherwise-transparent radiative cooling rates based on collisional-radiative equilibrium calculations without doing radiative transport. The physical basis of the code was discussed in JAYCOR Report J207-82-009[1].

Simple scaling laws are derived in Chapter III of Part I for the radiation from a quasi-adiabatically bouncing pinch, in which the radiative loss is a small fraction of the peak thermal energy. The dynamics of the wire-plasma and annular phases are also discussed, with some formulas given to describe initial conditions for the pinch phase. The scaling laws are used on uniform, optically-thin pinch plasma models, and corroborate I^4 dependence of the energetic radiated energy (as observed at Physics International) over a limited range of currents and plasma masses, (I=current through the plasma). A first-order correction to the minimum radius and maximum temperature of the implosion is also given, for small but non-negligible radiative energy loss dominated by energetic, transparent radiation. Caveats to the model are described.

A simple model for the nonlinear penetration of electric field into a finite plasma is discussed in Chapter IV of Part I, in which the conductivity (and thus the diffusion coefficient) is altered locally in time and space by heating and ionization induced by the diffusing field. A 1D computer simulation is described, but it is concluded that the restrictions on the model are too severe to accurately portray the realities of field penetration in imploding annular plasmas, and the reader is referred to the more advanced computational results of Part II.

This effort is intended to be primarily in support of the DNA objectives of understanding and projecting an approximate scaling of plasma radiation sources. An explicit tie-in with radiation physics work funded by DNA at the Naval Research Laboratory (NRL) can be seen from the central role played in this analysis by the curve of energetic-photon radiative power as a function of plasma electron temperature (it also depends weakly on plasma density and photon density) - such curves are supplied by the NRL effort. Less visible in this simplified analysis, but also important in the more quantitative calculations enabled by Part II of this report, are the effects of radiation transport on the energetics and the radial profiles of temperature, etc., in imploding plasmas. Here again there is interaction with the plasma radiation physics work at NRL, both in the use of transport algorithms developed at NRL, and in supplying NRL with reasonable implosion density and temperature histories for post-processing of emission spectral histories, etc. The RUNIN scoping code described in Part I of this report has been supplied to NRL, to use in conjunction with its more extensive radiation physics codes as an inexpensive, approximate time-evolution package for densities and temperatures during implosions.

Formulas are given for energetic radiative yield ($Y^{>}$) as dependent on load mass (m) and length (l), experimentally measurable current in the load (I), kinetic energy at the beginning of the assembled pinch phase (ε_1), and atomic physics parameters, such as the temperature (T_{pk}) at which the energetic radiation is maximized.

By choosing either the load mass per unit length or the current so as to optimize $Y^{>}$, one derives a formula for scaling of optimal energetic yield with load current I, in the adiabatic limit where the radiative energy loss has only a very small effect on the dynamics. Subject to the caveats described in the report, we verify the scaling

$$Y^{>} \propto I^{4}$$

found by earlier, more empirical work at Physics International.

We also show, to first order, how this scaling of $Y^{>}$ were I falls below I^4 at higher currents, due to the effects of radiation in reducing the peak attainable temperature for any given pinch initial conditions. Here 'first order' refers to the quantity $Y(r_m)$/(thermal energy), $Y(r_m)$ being the total radiative energy (energetic + less energetic photons) lost between onset of the assembled pinch phase and the time of minimum radius r_m (i.e., peak compression).

CHAPTER II

DEVELOPMENT OF THE RUNIN CODE

For the assessment of Plasma Radiation Source design feasibility, it is important to have an approximate scoping model that predicts implosion histories and scaling of radiative output with the appropriate input design parameters. To this end the RUNIN code has been written, incorporating (with modifications) the SAI "WIRES" Code describing the dynamics of an imploding array of wires, the JAYCOR "SQUEEZE" Code describing the dynamics and energetics of a pinching cylindrical plasma (with radiation the CRE ionization), and a "BRIDGE" code describing the intermediate annular plasma stage. For use in gas puff plasma modeling, the code can be started in the BRIDGE phase. This RUNIN code has been written, documented, run and debugged. It can also serve as the nucleus of a variational design optimization code[1].

A. WIRES: EQUATIONS FOR THE IMPLOSION OF THE WIRE ARRAY - MODIFICATIONS AND UNDERLYING ASSUMPTIONS

1. The equations governing the wire-plasma radius a (its thickness, not its position) in the SAI WIRES code was equivalent to the assumption that the radius has that value which gives pressure balance between the thermal pressure of the wire and the magnetic pressure of its field. The temperature is determined by assuming that the $2\pi a \ell \sigma_B T^4$ blackbody radiative cooling exactly balances the $I_N^2 R = \eta J^2 \ell \pi a^2$

ohmic heating (based on full field penetration of the 'wire'). Here σ_B is the Stefan-Boltzman constant, $2\pi a\ell$ is the surface area of a wire carrying current I_N over cross-sectional area πa^2 with resistivity η (resistance R). We have demonstrated that this gives instantaneously quite fat 'wires' at early times if I is large and T small. Since the expansion rate of the wires is limited by one or a few times the instantaneous sound speed, we have limited the radius to $a_0 + \int c_s(t)dt$ when this is less than the pressure-balance radius. Besides being more physically correct, this prevents the code from merging the wires into an annular plasma at very early times before they could have merged physically.

2. When the N wires with centers at radius r_c do finally merge, i.e., when

$$r_c \sin\frac{\pi}{N} = a \qquad [II.1]$$

(the tangency condition for a circular array of N circles of radius a), they are replaced by an annular layer (with outer radius r_1 and inner radius r_s) which has the same area as the collection of wires

$$\pi(r_1^2 - r_s^2) = N\pi a^2 \qquad [II.2]$$

and has a geometric mean radius equal to the radius of centers of the wires: $r_1 r_s = r_c{}^2$. The new velocity of the outer surface $\dot{r}_1$, is given by conservation of kinetic energy in the transition.

The use of the notation r_1 for the outer radius and r_s for the inner radius of the resulting annulus is intended to conform (at least in subscripts) to the notation of the RUNIN code, in which y_1 and y_s are the outer and inner radii respectively. The code announces the merge (both on the terminal and in the output data file) and proceeds to the integration of equations of motion for a uniform annular plasma, using a high-precision package integration routine.

The magnetic field energy in the WIRES code includes a contribution from positions inside the wire array. This is physical, but should go to zero as the wires merge to an annulus, even if the approximate equations of the WIRES code break down when the wires are close together. In the RUNIN code we have taken this contribution zero as soon as the wires merge.

Consistent with the assumption of complete field penetration of the individual wires, we have assumed uniform current density in the annular layer when it comes to calculating energy density integrals, but we have assumed in the force equations that all the J x B force is applied to the outer surface. In fact, a real physical difference between wire array implosions and foil or annular gas puff implosions may be that for wire array implosions the field penetration is fairly complete early in the wires phase and continues to be fairly complete after merging to an annulus, while in foil or gas puff implosions the current may be restricted to a relatively thin layer near the outer surface of the annulus. The full 1D MHD code described [elsewhere in this report] is capable of estimating the degree of field penetration into foils or gas puff annuli, and of showing the sensitivity of the implosion dynamics to the degree of penetration, whereas the simpler model presented in this section cannot investigate that question consistently. The actual field penetration is discussed in more detail in Chapter II of Part II of this report.

B. BRIDGE: EQUATIONS FOR THE UNIFORM ANNULAR PLASMA IMPLOSION

The equations of motion of the annular plasma result from performing $\int dr$ on the fluid equation and assuming that the density gradient $\partial n/\partial r$ remains zero except at the plasma edges. This latter assumption, equivalent to $\partial/\partial r(\nabla \cdot v) = 0$, requires $v(r)$ of the form

$$v(r) = k_1 r + k_2 r^{-1} \qquad [II.3]$$

and the conditions $v(r_1) \equiv \dot{r}_1$, $v(r_s) \equiv \dot{r}_s$ give equations for $k_1(r_1, \dot{r}_1, r_s, \dot{r}_s)$ and $k_2(r_1, \dot{r}_1, r_s, \dot{r}_s)$:

$$k_1 r_1 = \frac{1}{1-r^2}\dot{r}_1 - \frac{r}{1-r^2}\dot{r}_5 \qquad [II.4]$$

$$k_2/r_5 = -\frac{r}{1-r^2}\dot{r}_1 + \frac{1}{1-r^2}\dot{r}_5. \qquad [II.5]$$

Here $r \equiv r_s/r_1$, the ratio of inner to outer radius, which is of course time-dependent (as are k_1 and k_2). In the integrated force equation (Tidman and Colombant, 1979)^2 one has then

$$\int_{r_s}^{r_1} \frac{\partial v}{\partial t}\, dr + \int_{r_s}^{r_1} v \cdot \nabla v dr = \frac{1}{2}\dot{k}_1(r_1^2 - r_s^2) + \dot{k}_2 \ln(r_1/r_s)$$
$$+ \frac{1}{2}(\dot{r}_1^2 - \dot{r}_s^2) \qquad [II.6]$$

The internal viscous stress tensor the the velocity field of Equation [II.3] is divergenceless, so that all the force comes from the thermal and magnetic pressure gradients. For the net force we have

$$\int_{r_s}^{r_1} \nabla P dr = (n_e + n_i)\, T - \frac{B^2(r_1)}{8\pi} \qquad [II.7]$$

with $B(r_1) = 2I/cr_1$ (in cgs units).

It will be seen that if the velocity of the inner surface remains finite as it collapses to the origin, then the ℓn term in Equation [II.6] is singular as $r_s \rightarrow 0$. It is thus a mathematical feature of these approximate equations that a finite excess pressure from the outside causes $\ddot{r}_s$ to take on a momentarily infinite negative value as $r_s \rightarrow 0$. This lasts for zero duration and causes no physicl discrepancy because the singularity is integrable and $\dot{r}_1$ remains finite. It does, however, mean that the numerical integration of the equations must be done cleverly and approximately near the time of transition from annulus to plasma cylinder. Since the integrating routine used (DGEAR) shrinks its timestep when it finds larger accelerations, $|\ddot{r}_1|$ is arbitrarily limited to a reasonable value (10^{17}cm/sec^2) and the equations are carried forward approximately for the remaining short (sub-nanosecond) time until $r_s = 0$.

C. NUMERICAL INTEGRATOR PACKAGE

While the WIRES subroutine calls a simple fixed-step integrator subroutine (the same as in the original SAI WIRES code), the BRIDGE and SQUEEZE subroutines use the IMSL Library DGEAR package, a variable-timestep predictor-corrector integration routine designed for use with sets of stiff differential equations[3]. An override and exit is provided when doing the integrations in the BRIDGE phase, so that the inner radius goes to zero within some tolerance (10^{-6}cm) without going negative or shrinking the timestep indefinitely.

D. RADIATIVE LOSS AND OUTPUT TERMS FOR THE ANNULAR AND CYLINDRICAL PHASES

1. Temperature Dependence

While the use of blackbody emission is thought to be a good approximation in the WIRES phase of implosion because the temperatures are low, we have changed over in the annular BRIDGE phase and in the cylindrical SQUEEZE phase of the code to more sophisticated radiative output functions, although at present the radiation cooling and output formulae are based on transparency of the plasma to its energetically most important radiation. The collisional-radiative equilibrium (CRE) model is the basis for an emitted power per ion-electron pair, F_{rad}, modeled in detail by Duston et al.[4]. A Gaussian-spline fit to these results was obtained by Terry[5] and this fit, incorporated in subroutine CREMIT, is used in the code for the emitted power. This is overridden by the blackbody emission if that limit is exceeded. At present there is no absorbed radiation per se. A similar calculation is done for the line radiation power above a critical photon energy E_{ST}, usually taken to be 1 keV.

2. Correction for Nonuniform Temperature and Density

The plasma in a real implosion is not isothermal or isodensity, and is not fully transparent to its radiation. So the radiative loss term is not simply

$$P^0_{rad} = \pi(r_i^2 - r_s^2)\ell \cdot n_i^2 \, Z(T) \, F_{rad}(T) \qquad [II.8]$$

with average ionization state Z(T) but rather:

$$P_{rad} = \ell \int 2\pi r dr \; n_i^2(r) \; Z\{T(r)\} \; F_{rad}\{T(r)\} \qquad [II.9]$$

in the optically thin limit,

$$P^{BB}_{rad} = 2\pi \ell r_1 \sigma_B T^4_{eff} \qquad [II.10]$$

in the blackbody limit, and not expressible in closed form except in these limits.

Yet a simplified implosion model, to be useful and show correct trends, must include in some approximate way an average radiation function with about the same magnitude and dependence as the more exact problems, i.e., a suitable set of parameters $n_i(0)$, r_n, $T(0)$, r_T, $T(\infty)$ must be chosen, representing the heights and widths for the $n_i(r)$ and $T(r)$ distributions, and a function $Rad(r_1, r_s, T)$ must be constructed, so that

$$\pi \ell (r_1^2 - r_s^2) \; \bar{n}_i^2 Z(\bar{T}) Rad(r_1, r_s, T) = P_{rad} \qquad [II.11]$$

for suitable $\bar{n}_i\{n_i(0), r_n\}$, $\bar{T}\{T(0), T(\infty), r_T\}$. The proper choice of such parameters and suitable distributions for density and temperature are being investigated using the BLANKET code.

For the radiative output above 1 keV the effect of non-isothermal temperature profiles in the assembling plasma is indicated semiquantitatively by using the transparent CRE model with Gaussian-plus-constant temperature profiles in a Gaussian density profile. Figure II.1 shows the ratio of radiated power above 1 keV for this distribution, in aluminum, to that for an isothermal aluminum plasma with the same Gaussian density profile, as a function of the relative width (r_T) of the temperature profile. The temperature distributions are chosen in this case to have the same central temperature, and the temperature of the cooler outer

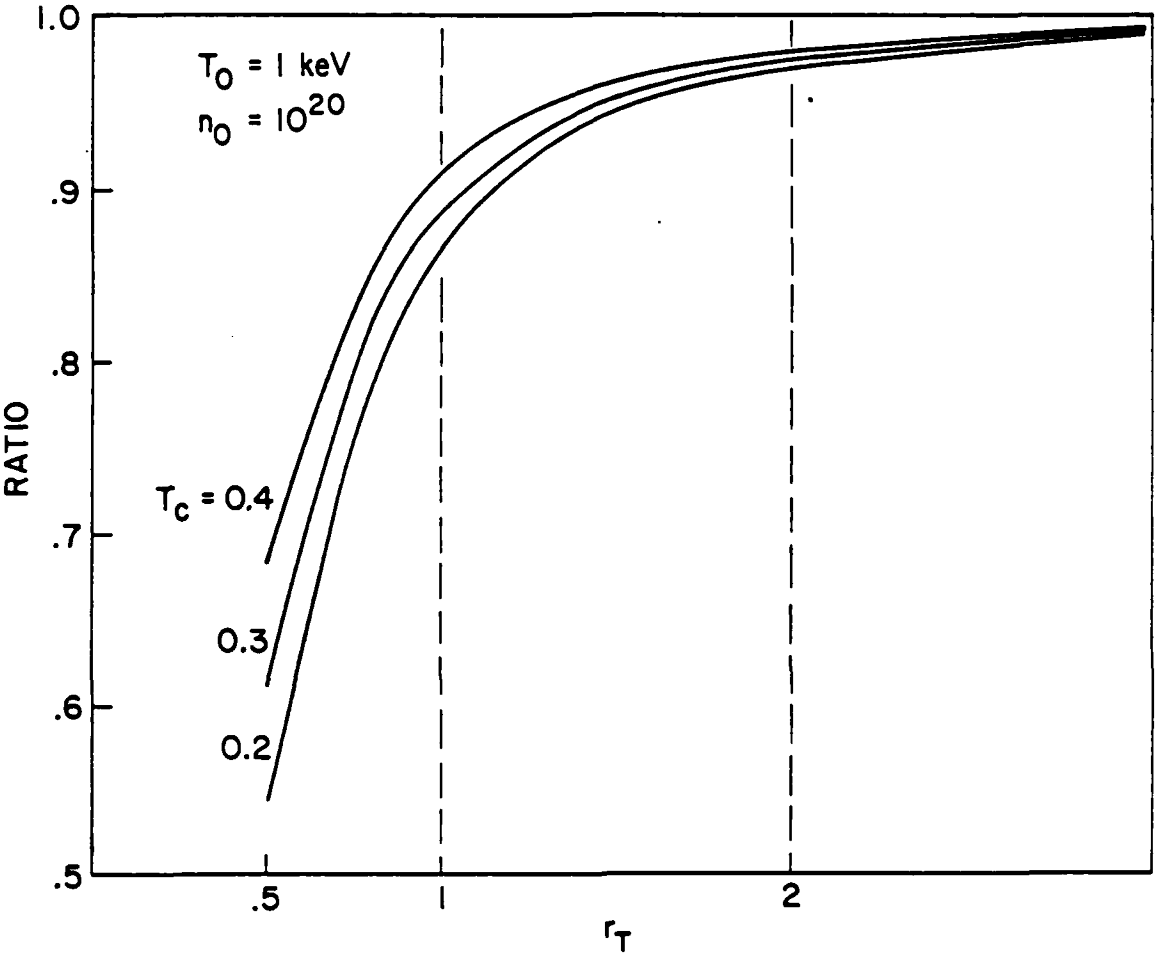

Figure II.1. *Ratio of radiated power above 1 keV for Gaussian-plus-constant temperature distribution to that from a uniform temperature distribution. Both distributions are assumed for plasma cylinder with Gaussian density profiles of unit width, and the parameter r_T measures the relative width of the temperature distribution ($r_T = \infty$ for isothermal limit).*

region is varied as a parameter. For use with the RUNIN code, where the energetics are described by a single temperature, comparisons are made with the same average temperature rather than with the same central temperature.

E. CAVEATS TO THE RUNIN CODE

The code described above models the dynamics of uniform plasma, either as (1) identical symmetrically-placed wire plasmas of circular cross section with forces acting at their centers, or (2) as an annulus of uniform density with force acting on the outer surface and model equations for the motion of the inner radius, or (3) as a uniform z-pinch driven at its outer surface by the net pressure (thermal minus magnetic) but ohmically heated as though carrying uniform current (a feature easily generalized if the current-carrying area is known). The circuit equation coupling the plasma load current to the generator voltage includes diode inductance and resistive impedance but does not presently include any currents not drawn in the load. The radiative loss is assumed either transparent or (when this exceeds blackbody) blackbody-limited. In the pinch phase this is probably a fair description, although the assumption of uniform temperature and density gives an overestimate of the energetic radiation (as just discussed in Section D). In the case of annular plasmas with moderately high mass and large radius the radiation formula is less believable and tends to over-cool the plasma.

Time-integrated pinhole and streak photos of wire array implosions appear to indicate that for massive enough arrays there is considerable plasma blowoff inward from the denser wire plasmas, forming either low-density plasma implosions or plumes[6]. This phenomenon, though interesting, is not within the scope of the WIRES model, which assumes uniform wire plasmas. Because of the observed advantages of gas-puff implosions, this wire blowoff phenomenon has not been further investigated here, even though it represents a significant deviation from the WIRES model.

One-D MHD codes allowing radial resolution sometimes show the formation of a density and temperature spike on the axis when the plasma annulus closes[7]. This is entirely reasonable and physical, but represents another feature not describable by a uniform-plasma model. In this case, however, we hope to generalize the simplified model to allow such a central compressed zone because the dynamics of gas puff runs may be seriously affected as the dense central spike is radiatively cooled to allow further compression.

CHAPTER III

APPROXIMATE SCALING LAWS

A. WIRE PLASMA PHASE OF ARRAY IMPLOSIONS

The very-early-time behavior of wire array implosions, involving the phase transitions of the material and the associated "pause" (dip) in the conductivity, is discussed in the literature on exploding wires and is not treated here. For practical modeling of the implosion dynamics, we start with an initial temperature at which the plasma has no more neutrals and is not dominated by strong coupling but has classical conductivity determined by Coulomb collisions.

After an initial heating expansion, the individual wire plasmas reach a local dynamic thermal equilibrium in their own reference frames. For the case of N imploding wires, local Bennett equilibrium, (i.e., pressure balance) gives an equilibrium temperature T:

$$[1+Z(T)]T = \frac{m_i}{2} \frac{I^2(t \leq t_1)}{\mu N c^2} \equiv \frac{m_i}{2N} b(t) \qquad [III.1]$$

or

$$\frac{1+Z(T_1)}{A_m} T_1(eV) = 52 \left[\frac{10^{-4}}{\mu(g/cm)}\right] \frac{I_{MA}^2(t_1)}{N} \qquad [III.2]$$

where m_i is the mass of an ion, μ is the total load mass (all N wires) per unit length, A_m is the atomic number of the load and I_{MA} is the total current (in MA) in all the wires. The degree of ionization Z(T) for aluminum at densities of order 10^{21} ions/cm^3 is shown in Figure III.1. The

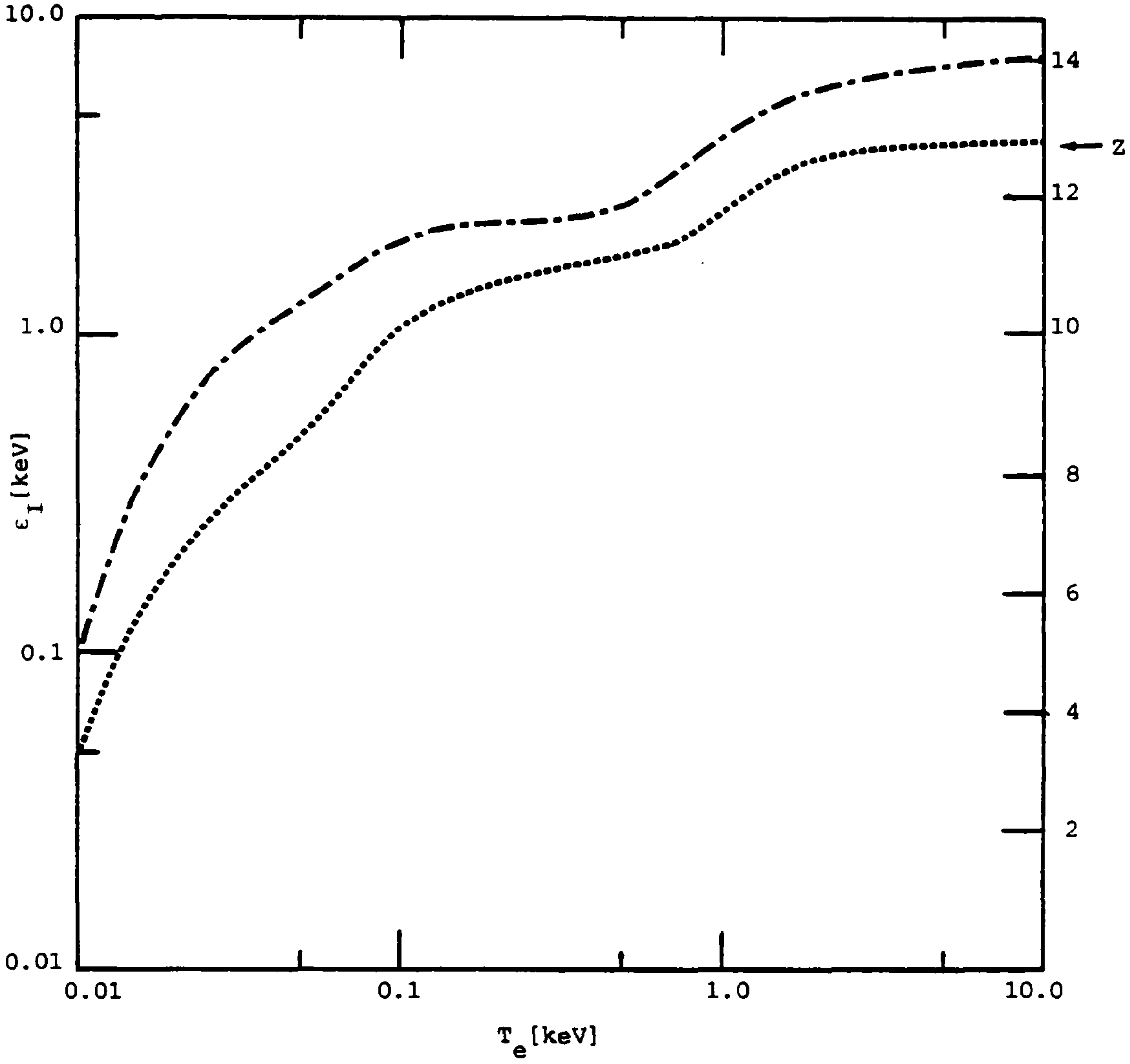

Figure III.1. Degree of ionization Z (right-hand scale) and ionization energy ε_I (left-hand scale) versus electron temperature for aluminum in CRE at 10^{21} ions/cm^3.

individual wire-plasma radius ρ expands until blackbody radiative loss equals the ohmic heating power and prevents further heating except by increasing current. This occurs at a wire-plasma radius given by

$$(2\pi\rho\ell)(\sigma_B T^4) = \left(\frac{\ell}{\pi\rho^2\sigma}\right)\left(\frac{I}{N}\right)^2 \qquad [III.3]$$

with σ the conductivity. Once the temperature is high enough that σ is determined by Coulomb collisions,

$$\sigma = \left(\frac{3}{16\sqrt{\pi}}\right)\left(\frac{m_e}{Ze^2}\right)\left(\frac{1}{\ell n\Lambda}\right)\left(\frac{2T}{m_e}\right)^{3/2} = K_\sigma T_{ev}^{3/2} Z^{-1} \qquad [III.4]$$

(so defining the constant K_σ). When these wire plasmas just merge, their centers are at radius $\rho\csc(\pi/N)$ and the resulting annular layer has outer radius given by

$$r_1^2 = \left[(N/2) + \sqrt{(N/2)^2 + \csc^4(\pi/N)}\right]\rho_1^2 \qquad [III.5]$$

with

$$\rho_1 = \left[\frac{Z(T_1)I_1^2}{2\pi^2 K_\sigma \sigma_B N^2}\right]^{1/3} T_1^{-11/6} \qquad [III.6]$$

in terms of the current I_1 and temperature T_1 at time t_1 (i.e., merge). (The geometrical factor in brackets is 8 for 6 wires and 22 for 12 wires.) Numerically,

$$\rho_1(\mathrm{cm}) = 172\left(\frac{I_1(\mathrm{MA})}{N}\right)^{2/3} Z(T_1)^{1/3} T_{1(ev)}^{-11/6}, \qquad [III.7]$$

and using the preceding information for T(I) in this expression one has

$$\rho_1(\mathrm{cm}) = .123\ I_{1(\mathrm{MA})}^{-3}\left[\frac{\{1+Z(T_1)\}}{10^{-4}A_m}\right]^{11/6} N^{7/6}\{Z(T_1)\}^{1/3}. \qquad [III.8]$$

But this scaling of ρ_1 and r_1 with I^{-3} [or about $I^{-1.6}$ when the Z(T(I)) dependence is included] holds only over a limited range of load mass and current.

As long as the wire-plasma radius ρ is not clamped by blackbody loss, it expands at a rate proportional to the sound speed, i.e., $\dot{\rho} \propto \{(1+Z(T)\}^{1/2} I \propto I\mu^{1/2}$, until the plasmas merge. With $\dot{\rho} \propto I\mu^{\pm 1/2}$ and the radius of centers r_c moving as $r_c \ddot{r}_c \propto I^2/\mu$, the merge condition $\rho = r_c \sin(\pi/N)$ determines the annulus formation in a dynamic way, if this merge occurs before radiation can limit ρ. For constant current the merge condition for non-equilibrated ρ (i.e., for high current) is

$$\frac{\rho}{\mathrm{erf}\sqrt{\ell n\{r_0/\rho \ \csc(\pi/N)\}}} = \sqrt{\pi/2}\ r_0/2N \qquad [III.9]$$

where r_0 is the initial array radius. For N=6 wires this gives $\rho = 0.1\ r_0$ and $r_c = 0.3\ r_0$ at merge. Thus, if radiation does not limit the wire-plasma radii, the merge occurs before very significant implosion has taken place, because the superheated wires expand rapidly. One then has an annular plasma implosion (starting with inner radius/outer radius = 1/2 for 6 wires) for more of the implosion than if the wire plasma size had been radiation limited.

From the code and the scaling just discussed, we can identify the following partially overlapping stages in the WIRES phase of a wire-array implosion:

(1) Ohmic heating dominates; wires expand and heat;

(2) Ohmic heating = PdV cooling ($\propto \dot{\rho}$); wires expand;

(3) Bennett equilibrium; $P_{th}-P_B=0$; $\{1+Z(T)\}T \propto I^2/\mu N$. Radiative cooling adjusts wire radius if T is low enough for the radiation to be blackbody;

(4) Blackbody/Bennett equilibrium: $\{1+Z(T)\}T \propto I^2/\mu N$ and

$$\rho \propto Z(T)^{1/3} I^{2/3} T^{-11/6} N^{7/6}, \quad \mu^{11/6} I^{-1.6} N^{7/6}.$$

(Not applicable if T becomes high enough for quasi-transparent radiative loss.)

Merging of the wire plasmas may interrupt the process at stage (2), (3) or (4), or there may be a further stage if the wires overheat.

In the simple physics of the WIRES phase of the RUNIN code, only stages (1) and (4) are explicitly included. Figure III.2 shows these stages, occupying roughly equal fractions of the WIRES phase at constant driving voltage.

The modeling and scaling of this wires phase is important to the radiation and dynamics in the later pinch phase only through the way it scales the initial conditions of the pinch phase (and in general through the duration of the wires phase, if the generator pulse time is limited).

The radiative yield of the pinch depends on the initial radius and temperature (at the beginning of the pinch phase) as r^{-1} $T^{-1/2}$. While I^2/μ is low enough, this goes as $\mu^{-4/3}$ I^2.

B. ANNULAR PLASMA STAGE

The merging of wires produces a somewhat irregular annular plasma; ignoring the irregularities, one can derive

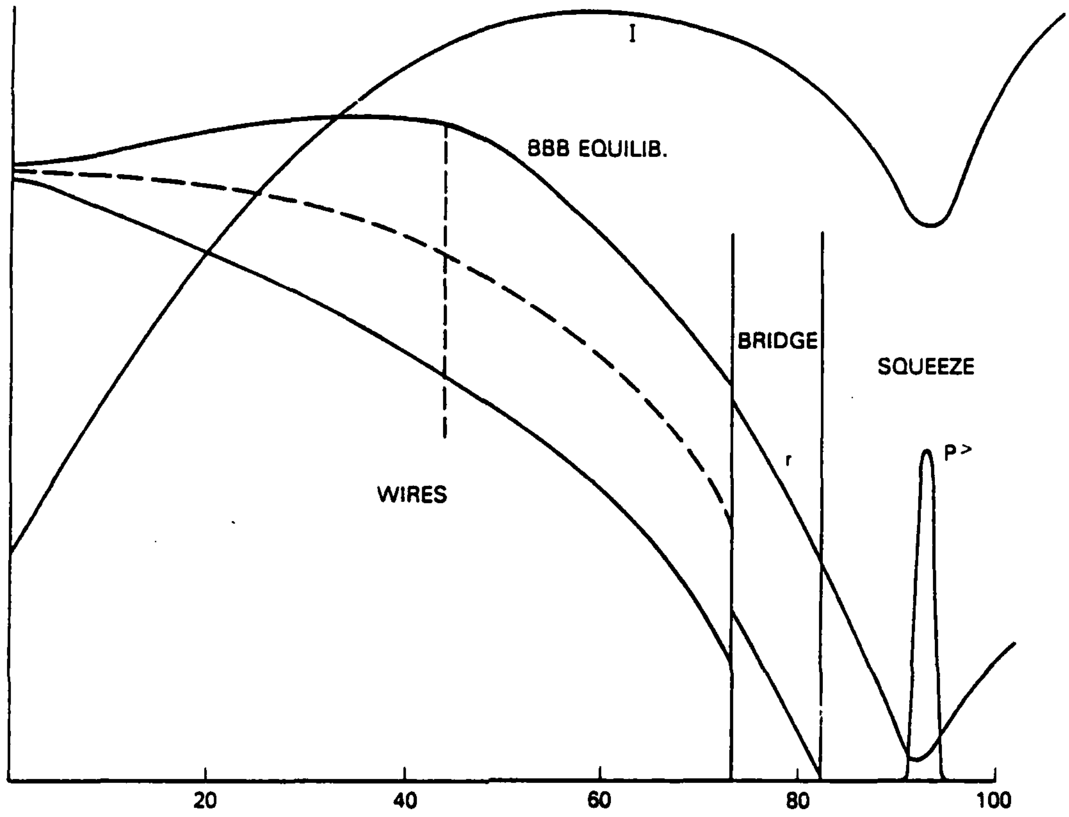

Figure III.2. Radial positions, current and energetic line radiation versus time (in ns) for a typical RUNIN code run. The wires expand until radiative cooling balances ohmic heating (dashed vertical line marks the onset of such Blackbody-Bennett equilibrium). Inner and outer extent of the wires are shown in the WIRES stage (radius of centers shown dashed); inner and outer radii of the annulus are shown in the BRIDGE stage. Pinch stage (SQUEEZE) onset occurs when inner radius goes to zero. The run shown was for constant 3 MV voltage.

differential equations for the inner and outer radii and the temperature in various simplified models. The same models and equations can be applied to the annular plasma formed by the pinching of an annular gas puff from a supersonic ring nozzle. Even with the simplest physical models, however, it has not been possible to do the sort of analytic modeling here that has been possible for the later pinch phase of the implosion. Here then the RUNIN code, or specifically its BRIDGE subroutine, provides the only simple guide. The code has been used to show, for example, that the ratio of final to initial radii and temperatures for the annular phase are very insensitive to the initial radius.

To develop simple rules for expressing variables at the end of the annular phase in terms of those at the beginning of the annular phase, the BRIDGE subroutine was run for a range of input variables. The "output variables" chosen for examination were ratios of final to initial radius, temperature, kinetic energy, and $r\sqrt{T}$, a variable which occurs in the formula for radiative energy loss in the case of transparent radiation.

Table III.1 shows the percentage variation in the output variables divided by the dynamic range (maximum value/minimum value) of the input variables, in the absence of radiation. None of the output variables depend sensitively on initial radius r_i. The kinetic energy ratio $\varepsilon_f/\varepsilon_i$ is the only output variable to have an interesting dependence on the initial velocity v_i of the annulus outer radius (i.e., on the initial kinetic energy ε_i of the annulus); the ratio of initial to final values of r, T, and especially $r\sqrt{T}$ are insensitive to v_i. The $r\sqrt{T}$ ratio (final to initial, for

	Dependent Variables			
Independent Variables	$\frac{r_f}{r_i}$	$\frac{T_f}{T_i}$	$\frac{KE}{KE_i}$	$\frac{r_f\sqrt{T_f}}{r_i\sqrt{T_i}}$
r_i	0	0	0.6/2	0
v_i	-.16/30	.13/30	-318/30	.09/30
T_i	.18/4	-.34/4	-.67/4	-.09/4

Table III.1. *Variation in ratios of final to initial dynamical quantities (shown by numbers in numerators) over dynamic range of initial conditions for the plasma annulus (shown by factors in denominators; a factor of 30 in v_i, for example, indicates a factor of 30 change, about some nominal value typical of the inward speed at the time the annulus is formed). Subscript f refers to the time at which the center of the annulus closes. A zero indicates very weak dependence.*

the annular phase) is also insensitive to the initial temperature of the annular plasma, T_i, although the r and T ratios depend on T_i.

C. RADIATION SCALING AND DYNAMICS IN THE PINCH PHASE

1. The Nearly-Adiabatic Uniform Radiator

The RUNIN code indicates that the temperature versus radius behavior of the pinch phase lies fairly close to the adiabatic law, for low-mass loads and low currents. The rate of doing PdV work greatly exceeds both ohmic heating and radiative loss except for a very brief interval near minimum radius. In addition the code indicates, in agreement with experiments, that the current does not change by a large factor during the compression. These facts suggest an approximate set of differential equations which can be treated analytically, with some approximations, to yield formulas for the output of energetic radiation and for its optimization. This section of the report treats first the zero-order formulas that result for a pinch in the adiabatic limit, and then the first-order correction when the radiative energy loss deepens the implosion perceptibly but not so much as to make the r-T trajectory deviate far from the adiabatic one for very long during the implosion. The utility of these formulas lies in the understanding they provide of the central qualitative concept of how to design and optimize an imploding radiator, and in their scaling with several variables at once - load mass, atomic mass number, initial conditions at the assembly of the plasma pinch, total current delivered to the load, etc. They reflect the facts that overdriving or underdriving the load can result in a radiation pulse that is too short or too cool, or occurs at a less-than-optimal density; they indicate what the optimal load current is for given conditions at the formation of the pinch, and how it depends on the load variables, how sensitive the radiation loss is to deviation from optimum, and what the peak attainable yield is as a function of the variables, subject of course to the limitations and approximations of the model. Finally, a discussion is provided of the limitations of the model, and of what happens to the predicted versus actually expected radiative behavior.

We arrive at simple formulas in two ways: first, by simple dimensional evaluation of the time-integral of the radiated power, and second, by a more careful evaluation based on expansion of the integrand. Both techniques presuppose that the plasma is nearly transparent to the energetic radiation, and that is consistent with the load masses of present and near-term experiments. We note that similar techniques apply to neutron production from fusion targets inasfar as the targets remain uniform cylindrical or spherical plasmas, but to radiatively driven implosions only inasfar as the radiation pressure varies nearly inversely with load radius.

A uniform pinch with mass m, atomic mass m_i, radius r, length ℓ, and temperature $T_i = T_e = T$ is governed approximately by the dynamical equation

$$m\ddot{r} = 2\pi r \ell (P_{thermal} - P_{mag}), \qquad [III.10]$$

with

$$P_{thermal} = n_i (1+Z)T, \qquad n_i = \frac{(m/m_i)}{\pi r^2 \ell} \qquad [III.11]$$

and

$$P_{mag} = \frac{1}{8\pi}\left(\frac{2I}{cr}\right)^2 \text{ in cgs units} \qquad [III.12]$$

Here Z(T) is the degree of ionization and I is the pinch current. This equation has the form

$$r\ddot{r} = aT - b \qquad [III.13]$$

when Z and I are nearly unchanged during the course of the pinch. Here

$$a \equiv 2(1+Z)/m_i \qquad [III.14]$$

and

$$b \equiv \frac{\ell I^2}{mc^2}. \qquad [III.15]$$

When ohmic heating is negligible (as with short-duration pinches with high conductivity) the temperature is governed approximately by

$$\dot{T} = -\{(C\dot{r}/r) + f\}T \qquad [III.16]$$

where C is an approximately constant adiabatic index, and the radiative loss function f(r,T) will be neglected in the adiabatic limit and used as a perturbation in deriving the first-order corrections. The temperature model equation arises from equating $P_{th}\dot{V}$ power, less radiative loss, with the time derivative of $3/2N_i(1+Z)T + N_i\epsilon_i$, where ϵ_i is the mean ionization energy (as a function of T) and $N_i = m/m_i$ is the total number of ions being compressed. The thermal pressure is $P_{th} = n_i(1+Z)T$, and

$$\frac{d}{dt}\left[\frac{3}{2}(1+Z)T + \epsilon_i\right] = \left[\frac{3}{2}\left(1+Z+T\frac{\partial Z}{\partial T}\right) + \frac{\partial \epsilon_i}{\partial T}\right]\dot{T}, \qquad [III.17]$$

while $\dot{V} \equiv 2\pi \ell r \dot{r}$. When f is negligible this $\dot{T}$ equation can be integrated to give the adiabatic law,

$$T/T_1 = (r_1/r)^C, \qquad [III.18]$$

with r_1 and T_1 the initial values at time t_1 when the pinch phase begins. This form for T is substituted into the force equation, which can then be integrated once to give

$$C\dot{r}^2 = C\dot{r}_1^2 - 2a(T-T_1) + 2b\ell n(T/T_1) \qquad [III.19]$$

or its equivalent form involving r instead of T.

The energetic radiative yield is the integral

$$Y^{>} = \frac{(m/m_i)^2}{\pi \ell} \int \frac{g\{T(t)\}dt}{r^2(t)} , \qquad [III.20]$$

in the transparent limit. The function g(T), i.e., the energetic radiation per pair of ions, is known for collisional radiative equilibrium, and it is assumed that the dynamical changes are slow enough that changes in radiative power track them without appreciable delay. The $\pi \ell r^2$ denominator comes from the assumption of uniform density and temperature, and gives a resonance shape to the integrand, which peaks near the time of peak compression. If the maximum temperature T_m is near the peak, T_{pk}, of g(T), then the integrand peaks when T reaches T_m and r reaches r_m, the minimum radius.

In the simplest approximation one evaluates the integral using the resonance approximation,

$$\int \frac{g(T)dt}{r^2} = \frac{g(T_m)\tau}{r_m^2} , \qquad [III.21]$$

where the pulse width τ is found approximately by treating $r(t)$ as quadratic about peak compression;

$$r = r_m + \frac{1}{2}\ddot{r}_m t^2 \to \tau = (r_m/\ddot{r}_m)^{1/2} \qquad [III.22]$$

so that

$$\frac{\tau}{r_m^2} = \frac{1}{r_m\sqrt{(r\ddot{r})_m}} = \frac{1}{r_m(aT_m - b)^{1/2}} \qquad [III.23]$$

Generally $aT_m \gg b$ during most of the pinch phase. To the extent that $r(T)$ follows the adiabatic law, one has $r_m \propto T_m^{-1/C}$, leaving only a weak dependence of τ/r_m^2 on T_m. This gives

$$Y^> \sim \frac{(m/m_i)^2}{\pi \ell a^{1/2} r_1 T_1^{1/C}} \; T_m^{(1/C-1/2)} g(T_m) \qquad [III.24]$$

in the adiabatic resonance-approximation limit. Recalling that $a = 2(1+Z)/m_i$ and using $Z \gg 1$ and $Z/m_i = 1/2m_p$ (with m_p the proton mass), one can write

$$Y^> \propto (m/\ell)^2 \; \ell m_i^{-2} T_m^{1/C-1/2} g(T_m) \qquad [III.25]$$

To the extent that $1/C - 1/2$ is small, this is clearly maximized (for given r_1, T_1) if the driving current and initial conditions are such as to make the maximum temperature T_m coincide with the peak of the energetic-radiation curve $g(T)$.

Since in the adiabatic limit T_m is reached together with r_m when $\dot{r} = 0$, we have from the equation for $C\dot{r}^2$ an equation for T_m:

$$a(T_m - T_1) - b\ln(T_m/T_1) = \frac{1}{2} C\dot{r}_1^2, \qquad [III.26]$$

A useful form of this for iteration is

$$T_m = T_1 + \frac{C}{2a}\dot{r}_1^2 + \frac{b}{a}\ln(T_m/T_1), \qquad [III.27]$$

since the $\ln$ term varies slowly. The $\dot{r}_1^2$ term represents kinetic energy provided prior to t_1 (which may also depend on a and b), and the $\ln$ term represents conversion of magnetic field energy to thermal energy since time t_1.

Prior to time t_1 the motion is not given by the same differential equations, is generally not adiabatic, and generally does not involve nearly-constant current. The kinetic energy acquired by time t_1 does, however, scale with b (i.e., with I_m^2) for any given pulse-shape of I(t) delivered to the load. Thus if $T_m \gg T_1$, then T_m is approximately proportional to b, i.e., to $\ell I^2/m$. So, while refinements can and will be made to this, one has a rough rule of thumb that for given r_1 and T_1, the current I_{opt} required to drive T up to T_{pk} scales nearly as $(\mu T_{pk})^{1/2}$, where $\mu \equiv m/\ell$, in the adiabatic limit; and $Y^>$ scales roughly as $\mu^2 \ell m_i^{-2} g(T_{pk})$. Both scalings are equally valid if I_{opt} is replaced by I_m and T_{pk} by T_m, so that one has

$$Y^> \propto I^4 \ell m_i^{-2} g(T_m) T_m^{-2} \qquad [III.28]$$

(aside from $\ln$ terms), in the adiabatic limit. With less than optimal current, i.e., where T_m is on the shoulder of the g(T) curve so that g(T) is increasing roughly as a power of T, one may even find a region where $g(T_m)T_m^{-2} \propto T_m^0$ and so experiments in this domain could fall along a curve $Y^> \propto I^4\ell$, even at constant m.

We will see later that the current required to reach a given T_m is larger in the nonadiabatic case. This will be only slightly offset by the fact that r_m will be smaller, giving larger values of $\int g/r^2$ once the desired T_m is reached. In the totally lossy case, the plasma cools as fast as it can be compressively heated, and temperatures on the order of T_{pk} cannot be reached. In that case $Y^>$ is generally small. This can happen if the load is sufficiently massive.

The evaluation and optimization of $Y^>$ can be refined somewhat within the adiabatic limit. One can make a better approximation to $\int g(T)dt/r^2$ and one need not argue that $T_m^{opt} = T_{pk}$. To evaluate the integral, one first constructs $\dot{T}/T$ as a function of $\phi = \ln(T/T_1)$, using the expressions for $r(T)$ and $\dot{r}(T)$, and then uses this to change the integration variable from t to ϕ. One then expands the singular denominator of the new integrand about its branch point at $T = T_m$, using the method of fractional derivatives (rather than simply expanding r^2 as $r_m^2 + 1/2\ \ddot{r}_m t^2$). Then, because the g(T) curve is nearly parabolic in a log(g)-log(T) plot, one can use the model

$$\ln g = \ln g_{pk} - B[\ln(T/T_{pk})]^2 \qquad [III.29]$$

(with fit parameter B) to do the resulting integral. Carrying out this procedure, we have

$$\int \frac{g(T)}{r^2} dt = \frac{\sqrt{2}}{C} \frac{1}{r_1} g_{pk} e^{-B\phi_{pk}^2} \int_0^{\phi_m} \frac{e^{A\phi - B\phi^2} d\phi}{\sqrt{\epsilon_1 + b\phi - aT_1(e^{\phi} - 1)}} \qquad [III.30]$$

with $\phi = \ln(T/T_1)$, $A = C^{-1} + 2B\phi_{pk}$, $\epsilon_1 = \frac{1}{2} C\dot{r}_1^2$, and

$$\epsilon_1 + b\phi - aT_1(e^{\phi} - 1) = 0 \text{ defining } \phi_m. \qquad [III.31]$$

Letting $w = \sqrt{\phi_m - \phi}$ and expanding the radicand about $w = 0$,

$$\varepsilon_1 + b\phi - aT_1(e^{\phi} - 1) = (aT_m - b)w^2, \qquad \text{[III.32]}$$

the integral on the right becomes

$$P(b,\phi_m) \int_0^{\sqrt{\phi_m(b)}} Q(w)dw \qquad \text{[III.33]}$$

with

$$P(b,\phi_m) = \frac{2\exp(A\,\phi_m - B\,\phi_m^2)}{\sqrt{aT_1\exp(\phi_m) - b}} \qquad \text{[III.34]}$$

and

$$Q(w) = \exp\{-(A - 2B\phi_m)w^2 - Bw^4\}. \qquad \text{[III.35]}$$

One can now optimize $P\int Qdw$ for given r_1 and T_1 by setting its derivative with respect to b equal to zero; doing so gives (after some algebra)

$$(x + \Delta)(x + \alpha)(x - \varepsilon) + (\Delta - \alpha)/4B = 0, \qquad \text{[III.36]}$$

where

$$x = \ell n(T_m/T_{pk}), \qquad \text{[III.37]}$$

$$\Delta = \phi_{pk} + d\varepsilon_1/db, \qquad \text{[III.38]}$$

$$\alpha = \phi_{pk} + \varepsilon_1/b + aT_1/b - 1, \qquad \text{[III.39]}$$

and

$$\varepsilon = (2C^{-1} - 1)/4B. \qquad \text{[III.40]}$$

When T_m is near T_{pk} as expected physically, x is small and the optimal value of x is

$$x_{opt} = \frac{N\alpha\Delta - 1}{4B\alpha\Delta - N(\alpha + \Delta)} \qquad [III.41]$$

with

$$N \equiv 2C^{-1} - 1. \qquad [III.42]$$

This gives the optimal value of $b \equiv \ell I^2/mc^2$:

$$b_{opt} = \frac{aT_{pk}\, e^{x} - aT_1}{(\varepsilon_1/b) + \phi_{pk} + x} \qquad [III.43]$$

with $x = x_{opt}$. Expanding this for small x, one has

$$b_{opt} = (aT_{pk}/\Delta)\left[1 + \left(\frac{\Delta-1}{\Delta}\right)\left(\frac{N\alpha\Delta - 1}{4B\alpha\Delta - N(\alpha+\Delta)}\right)\right] \qquad [III.44]$$

where the 1 dominates the bracket. In physical terms, if one drops the small correction,

$$I^2_{opt} = \left(\frac{m}{\ell}\right) \frac{2(1+Z)}{m_i} \frac{c^2\, T_{pk}}{\Delta} \qquad [III.45]$$

or

$$I_{opt}(MA) = 0.3 \times 10^3\left[\frac{m}{\ell}\left(\frac{g}{cm}\right)T_{pk}(keV)\Delta^{-1}\right]^{1/2} \qquad [III.46]$$

with

$$\Delta = \varepsilon_1/b + \ln(T_{pk}/T_1) \qquad [III.47]$$

and ε_1/b is assumed independent of b. The radiation integral with the optimal driving current can be evaluated using

$$\int_0^\infty \exp[-(C^{\pm 1} - 2Bx)w^2 - Bw^4]dw \equiv \frac{1}{2}\, \psi^{1/4} e^{\psi}\, K_{1/4}(\psi)(2B)^{-1/4}$$

$$\psi \equiv \left(\frac{1}{2}\, C^{-1} - Bx\right)^2/2B \qquad [III.48]$$

which is approximately $0.91B^{-1/4}$ when $C^{-1} - 2Bx \leq 1/2$. This gives

$$Y_{opt}(J) \approx 0.2\mu^2 \ell A_m^{-2} \left(\frac{T_{pk}}{T_1}\right)^{N/2} \left[\frac{\Delta A_m}{\alpha(1+Z)C\sqrt{B}}\right]^{1/2}$$

$$\left[\frac{g_{pk}(W\ cm^3)}{10^{-42}}\right] \left[r_1(cm)\sqrt{T_1(eV)}\right]^{-1} \qquad [III.49]$$

with μ the total mass per unit length (gm/cm) and A_m the atomic mass in AMU. We note here that $\alpha \approx \Delta - 1 \sim 3$ and $A_m/(1+Z) \approx 2$. The initial radius at assembly, r_1, is expected to be of order 0.3 cm in typical experiments. The index N is roughly 1/2.

Before refining these estimates for the adiabatic limit, let us consider the magnitudes they imply. To do this, we recall section A of this chapter, and model the $t<t_1$ cool collapse phase as having $(1+Z)T$ approximately proportional to $I^2(t)$ once a Bennett quasi-equilibrium is reached. The plasma initially heats and expands until reaching such an equilibrium, although the equilibrium may not always be reached before time t_1. This collapse-phase model is especially appropriate for wire array implosions where a clear Bennett-pinch quasi-equlibrium exists for each wire. Referring to this equilibrium temperature as $T_0(I)$, its near-constancy for constant I gives us $T_1 \approx T_0$ in the constant-current case. Physically, the near-absence of heating in this phase reflects the fact that although the plasma is accelerated inward by the field, there is nothing except magnetic field for it to push against to compress and heat, as long as the acceleration timescales are long compared with the sound transit time across the plasma(s) (i.e., as long as there is no shock heating).

For wire array implosions, to the extent that the current I_{MA} in the pinch phase is related to the typical current I_w in the WIRES phase, and to the extent that the annular BRIDGE phase does not strongly heat or cool the plasma, one can relate r_1 and T_1 at the beginning of the pinch phase to the driving terms in the WIRES phase. Over the limited range of total wire currents I_w for which pressure-balance Bennett equilibrium is achieved in the WIRES phase one has for aluminum 6-wire arrays

$$[1+Z(T_1)]T_1(\mathrm{keV}) \approx 2.25 \times 10^{-5} I_w^2/\mu(\mathrm{g/cm}) \qquad [\mathrm{III}.50]$$

with I_w in MA, from Equation [III.2]. Over the even-more-limited range of I_w for which blackbody cooling balances Ohmic heating one has

$$r_{1_w}(\mathrm{cm}) \sim 1.5 \times 10^5 \; I_w^{-3} Z^{1/3} [\{1+Z(T_1)\}\mu]^{11/6} \qquad [\mathrm{III}.51]$$

for a 6-wire aluminum array merging at radius r_{1_w}. (Again I_w is in MA, and the formula probably does not apply much above $I_w^2/\mu = 10^4$.) The BRIDGE phase further compresses this outer radius by a factor of order 0.6 before it assembles into the pinch phase.

The ratio of maximum to initial temperatures in the pinch phase, T_m/T_1, based on the quasi-adiabatic approximation, is shown versus the normalized quantity

$$K_0 = \frac{C\dot{r}_1^2}{2aT_1} \qquad [\mathrm{III}.52]$$

in Figure III.3, for various values of $\Gamma \equiv b/aT_1$. For aluminum,

$$\Gamma = 10^{-4}(I_{MA}^2/\mu)/T_1(\mathrm{keV}). \qquad [\mathrm{III}.53]$$

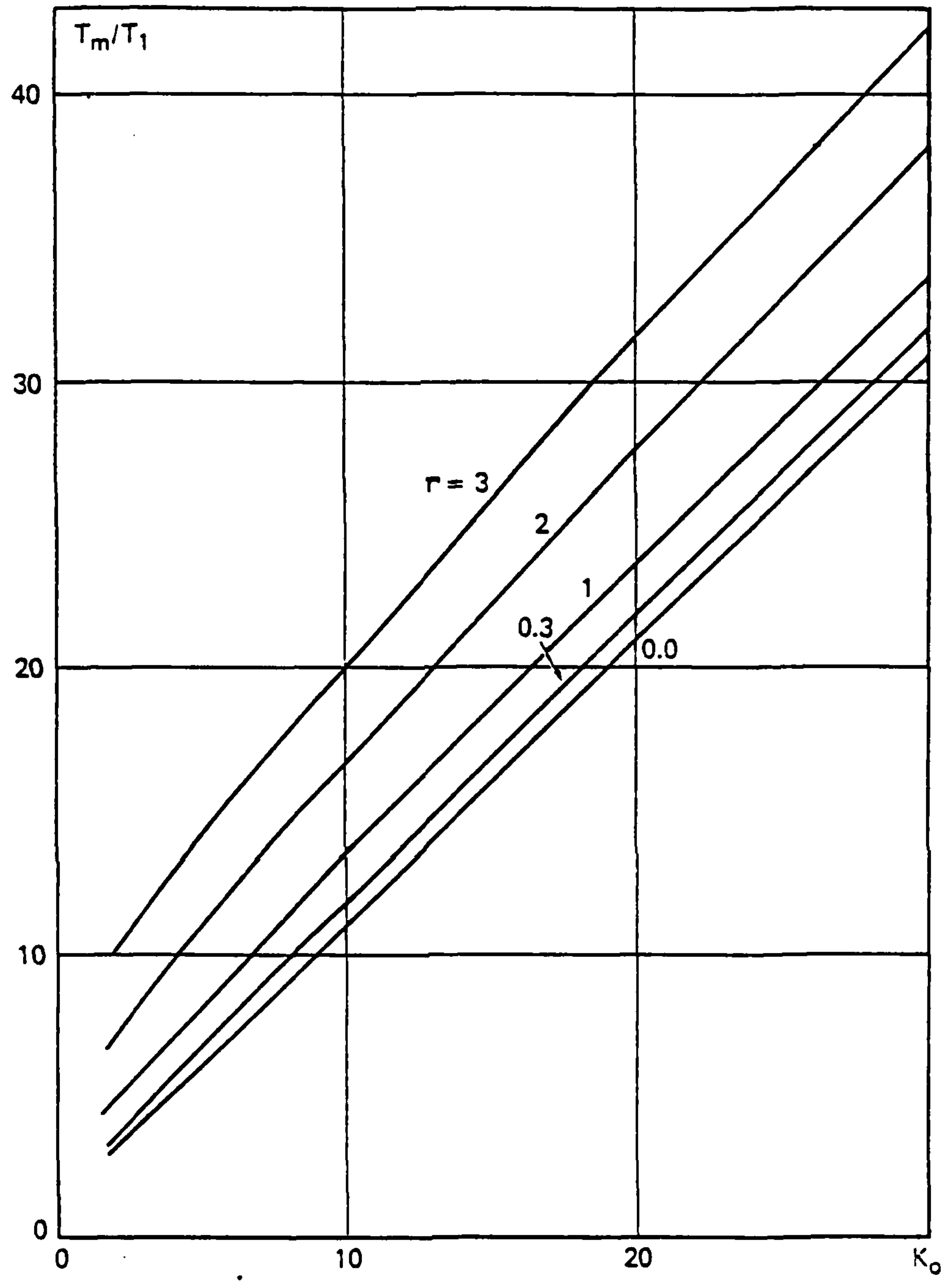

Figure III.3. Ratio of peak temperature to initial pinch temperature, as a function of initial kinetic energy (scaled to thermal), for various normalized currents, in the quasi-adiabatic limit.

For any given generator voltage pulse shape one expects both $\dot{r}_1^2$ and T_1 to be roughly proportional to b or I^2/μ, so that neither K_0 nor Γ should vary greatly as I^2/μ is changed. What variation there is should come about because of changes in the wire merge conditions and duration of the annular phase. K_0 is ratio of kinetic to thermal energy content at the beginning of the pinch phase, while Γ is a ratio of magnetic to thermal energy at that time.

2. Singular-Perturbation Expansion for Nonadiabatic Trajectories

The energetic radiation output (Equation III.20) for the nonadiabatic problem can be calculated by expanding g(T) and r(t) about the peak compression, $r=r_m$, which we take for convenience to occur at t=0. We keep in mind the useful case where the nonadiabatic trajectory given by

$$\begin{aligned} \ddot{r} &= (aT - b)/r \\ \dot{T} &= T(-C\dot{r}/r - f), \end{aligned} \qquad \text{[III.54]}$$

is near the adiabatic one given by the special case f=0; in the (ℓnr, ℓnT) plane the trace of the adiabatic trajectory is up and back along the line segment $\ell n(T/T_1) = -C\ell n(r/r_1)$. The nonadiabatic one is a loop, as shown in Figure III.4, except at late times (when it may re-compress).

Equations [III.54] give first integrals.

$$T/T_1 = (r/r_1)^{-C} \exp\left[-\int_{t_1}^{t} f\{r(t),t\}dt\right] \qquad \text{[III.55]}$$

and

$$C\dot{r}^2 = C\dot{r}_1^2 - 2a(T-T_1) + 2b\ell n(T/T_1) - 2\int_{t_1}^{t}(aT-b)f dt. \qquad \text{[III.56]}$$

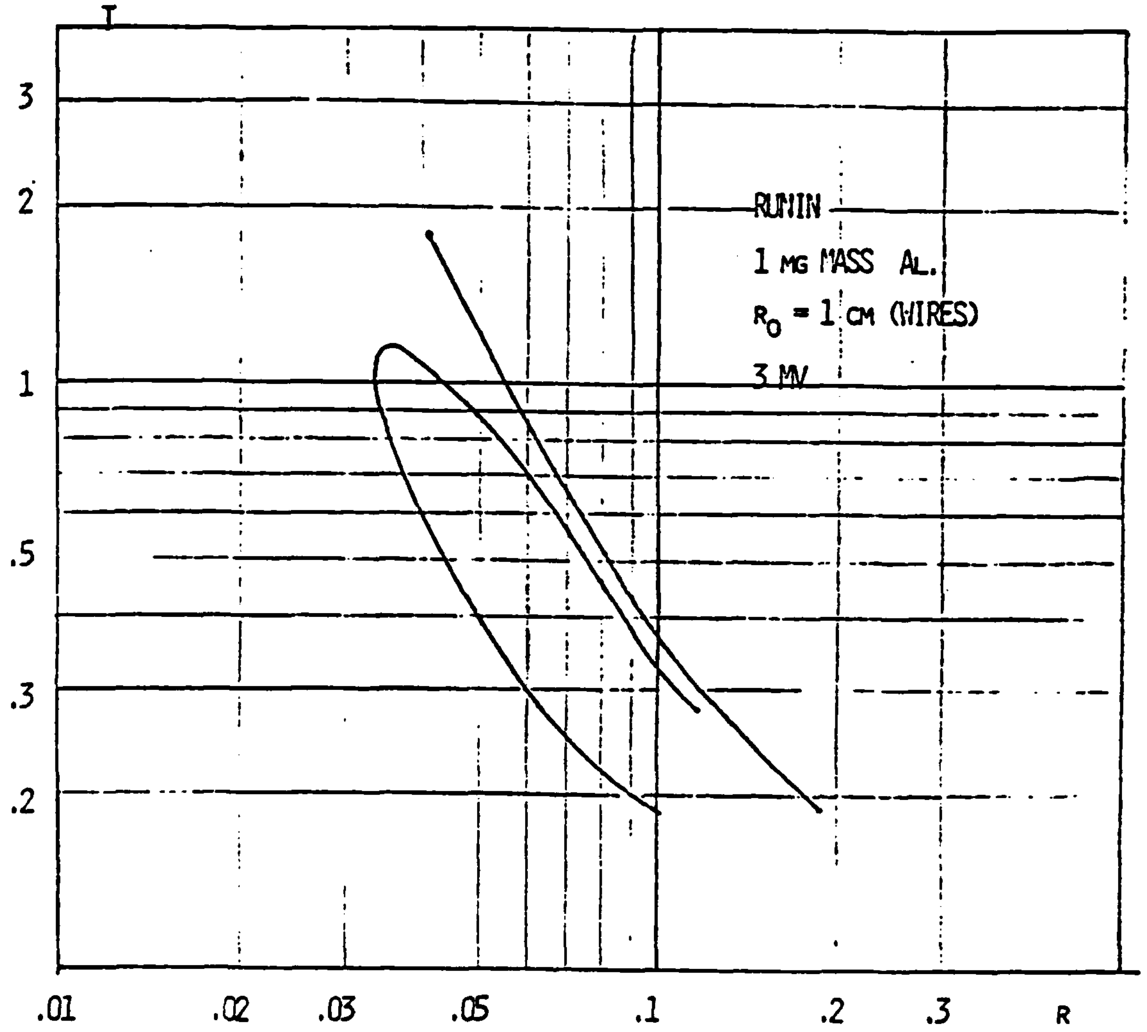

Figure III.4. ℓn T versus ℓn r trajectory loop, compared with adiabatic trajectory, both calculated for a constant voltage driver using the RUNIN code.

These can be written as

$$T/T_1 = (r/r_1)^{-C}\{1-\varepsilon_1(T,\ T_1,\ a,\ b,\ C,\ m)\} \qquad [III.57]$$

and

$$\dot{r} = (F - \varepsilon_2)^{1/2}, \qquad [III.58]$$

where

$$\varepsilon_1 \equiv \int_{t_1}^{t} f\ dt \qquad [III.59]$$

and

$$\varepsilon_2 \equiv C^{-1}\int_{t_1}^{t} (aT - b)f\ dt \qquad [III.60]$$

and F is the function $\dot{r}^2$ for the adiabatic case,

$$F = \dot{r}_1^2 - (2a/C)(T-T_1) + (2b/c)\ \ell n(T/T_1). \qquad [III.61]$$

The radical in [III.58] cannot be expanded directly for small ε_2 because F=0 at peak compression in the adiabatic case. We will return to these formulas when computing the values of r and T at peak compression.

For the radiative yield we expand the numerator and denominator of

$$\int \frac{g\{x(t)\}dt}{r^2(t)} \ :$$

about the time t=0 when r has its minimum value r_m:

$$r(t) = r_m + \frac{1}{2}\ddot{r}_m t^2 + \frac{1}{6}\dddot{r}_m t^3 \qquad [III.62]$$

$$g\{x(t)\} = g_m + g'_m\dot{x}_m t + \frac{1}{2}(g''_m\dot{x}_m^2 + \ddot{x}_m g'_m)t^2 + \ldots [III.63]$$

where we have used $x \equiv \ell n(T/T_{pk})$. The subscript m indicates evaluation of a quantity at time 0 when $r=r_m$. (In the non-adiabatic case T has largely reached its maximum and is decreasing by the time r reaches its minimum value r_m.) Figure III.5 shows the shape $1/r^2(t)$ for the adiabatic and nonadiabatic (dashed) cases. The t^3 term in r(t) is due entirely to the radiative energy loss.

Using the nonadiabatic Equations [III.54] we can evaluate the time derivatives at t=0 ($\dot{r}=0$):

$$\ddot{r}_m = (aT_m-b)/r_m \qquad [III.64]$$

$$\dddot{r}_m = a\dot{T}_m/r_m=-af(r_m,T_m)T_m/r_m=-aG(x_m)/(\pi\ell r_m^3) \qquad [III.65]$$

$$\dot{x}_m \quad \dot{T}_m/T_m = -f(r_m,T_m) = -G(x_m)/(\pi\ell r_m^2T_m) \qquad [III.66]$$

$$\ddot{x}_m = \ddot{T}_m/T_m - (\dot{T}_m/T_m)^2 = -C(aT_m-b)r_m^{-2}$$
$$-G'(x_m)\dot{x}_m(\pi\ell r_m^2T_m)^{-1} - \dot{x}_m^2 \qquad [III.67]$$

[since $\ddot{T}_m = -C(\ddot{r}_m/r_m)T_m - \frac{d}{dt}(fT)|_m$], where we have used the fact that T_m should be hot enough that most of the radiation energy loss at peak compression is through the transparent hot component described by power $g(x)/(\pi\ell r^2)$:

$$T_mf(r_m,T_m) = G(x_m)/(\pi\ell r_m^2)$$

$$[III.68]$$

$$\text{with } G(x_m) = (m/m_i)g(x_m)/Z_2$$

Thus the term $G_m'\dot{x}_mt$ in Equation [III.63] is of order $GG' \sim G_m^2\dot{x}_m^2$, the $G_m''\dot{x}_m^2$ term is of order G^3, and the $\ddot{x}_mG_m$ is of order $G' \sim G_mx_m$.

With these expansions of g(t) and r(t), the integral $\int(g/r^2)dt$ has the form

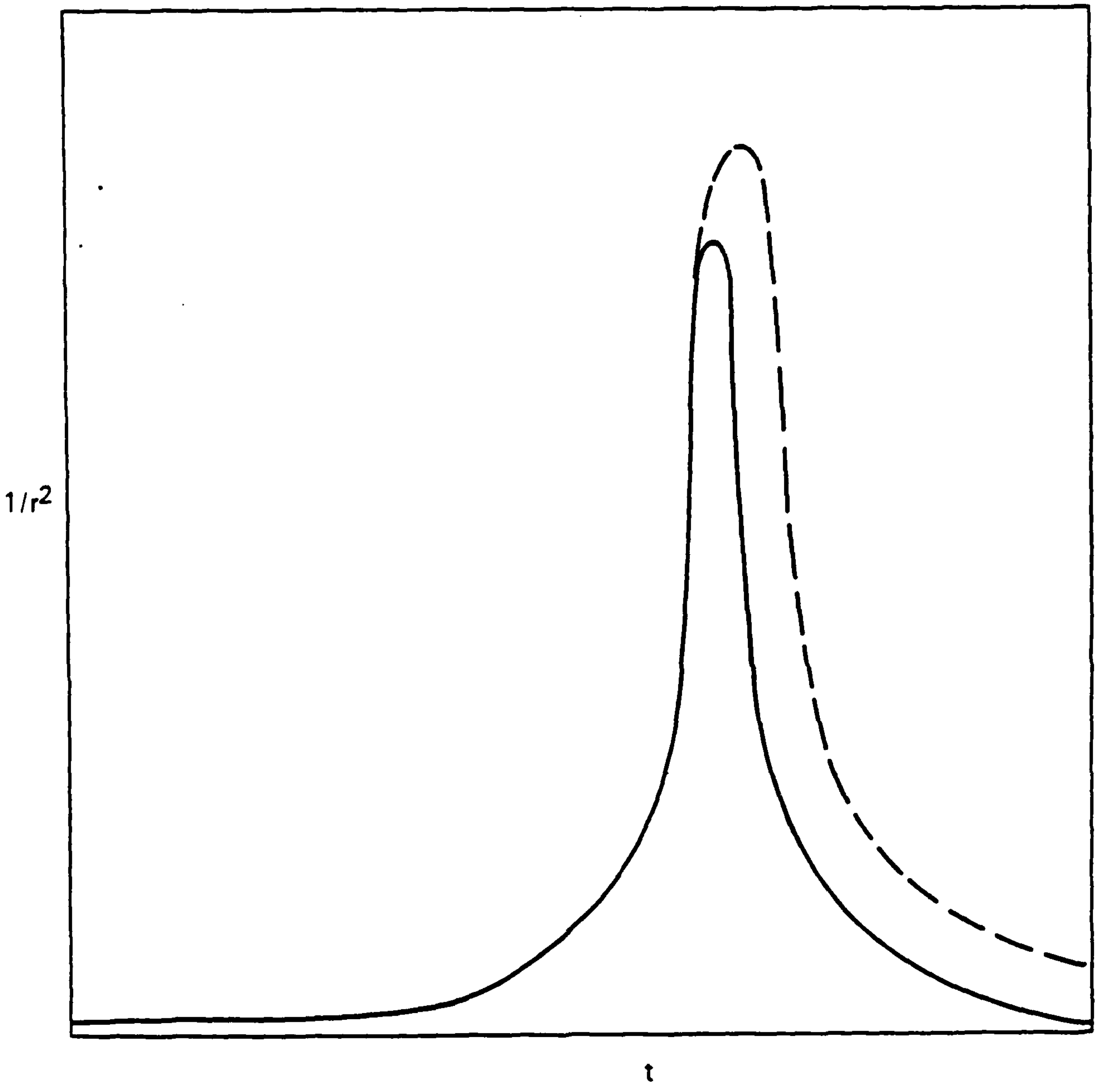

Figure III.5. $1/r^2$ versus time for adiabatic (solid curve) and nonadiabatic (dashed curve) pinch bounce.

$$\int \frac{(A_1 - B_1 t \; C_1 t^2)}{(A_2 + B_2 t^2 - C_2 t^3)^2} \; dt. \qquad [III.69]$$

This is done by (a) expanding the denominator since c_2 is small,

$$(A+Bt^2-Ct^3)^{-2}=(A+Bt^2)^{-2}+2Ct^3(A+Bt^2)^{-3}+O(C^2t^6),$$

(b) approximating the integration limits by $-\infty$ to $+\infty$, (c) ignoring odd functions of t in the integrand since they integrate to zero, and (d) using the formulas

$$\int_{-\infty}^{\infty} \frac{dt}{A + Bt^2} = \pi(AB)^{-1/2},$$

$$\int_{-\infty}^{\infty} \frac{dt}{(A + Bt^2)^2} = \frac{\pi}{2A} (AB)^{-1/2},$$

$$\int_{-\infty}^{\infty} \frac{dt}{(A + Bt^2)^3} = \frac{3\pi}{8A^2} (AB)^{-1/2},$$

and

$$\int \frac{t^m dt}{(A + Bt^2)^p} = \frac{1}{B} \int \frac{t^{m-2} dt}{(A + Bt^2)^{p-1}} - \frac{A}{B} \int \frac{t^{m-2} dt}{(A + Bt^2)^p}.$$

The result is

$$(\pi/2)(A_2B_2)^{-1/2}\{(A_1/A_2)-(C_1/B_2)-(3B_1C_2/2B_2^2)\} \qquad [III.70]$$

or

$$\int (g/r^2)dt = \frac{\pi/\sqrt{2}}{r_m(aT_m-b)^{1/2}} \left[g_m - Cg'_m - \frac{a/(\pi\ell)^2}{(aT_m-b)^2} \frac{G_m^2 g'_m}{r_m^2 T_m} - \frac{g_m(G_m'^2 - G_m G'_m + GG''_m)}{r_m^2 T_m^2 (aT_m-b)(\pi\ell)^2} \right] \qquad [III.71]$$

Modeling g by $g_{pk}\exp(-Bx^2)$ as before and neglecting b compared with aT_m, one has

$$\int (g/r^2)dt = \frac{\pi/\sqrt{2}\; e^{-Bx^2} g_{pk}}{r_m(aT_m)^{1/2}} \left[(1 - 2CBx) + \frac{G_{pk}^2 \exp(-2Bx^2)}{ar_m^2 T_m^3 (\pi\ell)^2} (1 - x - 4Bx^2) \right] \qquad [III.72]$$

evaluated at $x = x_m \equiv \ell n(T_m/T_{pk})$.

The values of r_m and T_m are not the same as in the adiabatic case (both are smaller). Subracting the first integrals of the adiabatic motion equations from those of the nonadiabatic case gives

$$\Delta x + c\Delta(\ell nr) = - \int f(r,T)dt \qquad [III.73]$$

$$\Delta x - \frac{a}{b} T_{pk}\Delta(e^x) = b^{-1} \int (aT-b)f(r,T)dt \qquad [III.74]$$

where Δ indicates the change from the adiabatic case with the same b value. Evaluating these at r_m ($t=0$, $x=x_m$) and replacing the lower integration limit by $-\infty$, we can use techniques similar to (a)-(d) above, to find (after some algebra):

$$\varepsilon_1 = \int_{-\infty}^{0} f(r,T)dt = \frac{1}{2\sqrt{2}\ell} \left(\frac{1+C+2CBX_m}{T_m}\right) \frac{1}{r_m\sqrt{aT_m}} \frac{G_m}{r_m^2}$$

$$= \frac{1}{2} \frac{(1+C+2CBX_m)}{(1+CBX_m)} \frac{Y^{>}}{(m/m_i)Z_2T_m} , \qquad [III.75]$$

$$C\varepsilon_2 = \int_{-\infty}^{0} (aT-b)f\,dt = \frac{1}{2\sqrt{2}\ell} \frac{a}{r_m\sqrt{aT_m}} \frac{G_m}{r_m^2}$$

$$= aT_m\left(\frac{1}{1-CBX_m}\right)\cdot\frac{1}{2} \quad \frac{Y^{>}}{(m/m_i)Z_2T_m} \qquad [III.76]$$

to first order in G.

Since m/m_i is the total number of ions and $Z_2 \doteq 3/2(1+Z)$, the ratio

$$Y \equiv \frac{Y^{>}}{(m/m_i)Z_2T_m} \qquad [III.77]$$

is just the radiative energy loss during the pinch phase as a fraction of the peak thermal energy of the load. Then Equations [III.75] and [III.76] can be used in [III.73] and [III.74] to find

$$\left.\begin{aligned} \Delta x &= -\frac{(1 + C + 2CBX_m)}{(1 + CBX_m)}\,\frac{Y}{2} \\ \Delta r &= 0 \end{aligned}\right\} \text{ to first order in Y,} \qquad [III.78]$$

i.e.,

$$T_m(b) = T_{mad}(b)\ \exp[-(Y/2)(1+C+CBX_m)/(1-CBX_m)] \qquad [III.79]$$

and

$$r_m(b) = r_{mad}(b) \qquad [III.80]$$

to first order in Y. (T_{mad} is the maximum T predicted in the adiabatic case, and r_{mad} is the minimum radius in the adiabatic case.) To first order in Y then, the deviation from the adiabatic trajectory due to radiative energy loss reduces the temperature at maximum compression, for any given $b=I^2/\mu c^2$, but does not appreciably change the minimum radius of the pinch. (The radius change is second order in Y.)

Subject to the limitations of the uniform-plasma model (etc.), the RUNIN code allows assessment of these results, whereas the analytic scaling laws for the quasi-adiabatic radiator do not apply when the radiative loss proceeds as fast as thermal gain. Because of this, the RUNIN code will shortly be used for investigating the branching ratio, $P_{rad}/[d(nT)/dt]$, as a function of n_i, T, and the total input power $-d/dt \int 1/2 \rho V^2 d^3 r$, and for scoping optimal conditions at high currents. Related analytic work will be carried on in that conjunction, to obtain approximate scaling laws for the efficient-radiator case as well.

D. CAVEATS

Results such as these derived from simplified approximate models, deserve caution in their application to real laboratory systems. We list here the major assumptions in the foregoing scaling laws and cautions appropriate to them.

1. Uniform Plasma

If only a fraction of the total plasma volume radiates at the indicated temperature, not only must the energetic radiation estimates be reduced proportionally, but the non-adiabatic corrections must be generalized due to the additional lower-temperature radiation from the cooler plasma fraction.

2. Inefficient Coupling of Kinetic Energy to Radiation

First-order corrections to a quasi-adiabatic pinch are appropriate only if the energy losses due to radiation are not extremely large. The total low-energy radiative loss from a cool ohmically heated discharge can exceed the thermal energy content of the plasma at any one time, and in fact that is an efficient way to design long-pulse low-energy-radiation sources; but it is clearly not describable by the formalism used here to estimate radiation from a somewhat damped pinch bounce.

3. Energetic Radiation Dominates Losses in the Pinch Phase

The use of the approximation $\dot{Y} \approx \dot{Y}^{>}$ in formulas is not a necessity, but is done for simplicity and is appropriate for a uniformly hot plasma near the peak of the radiative loss function. Formulas [III.78] must be interpreted cautiously when applying to typical laboratory cases where the energetic radiation during the pinch phase may be a smaller fraction of the total radiative loss.

4. Constant Current

Although one can model non-constant currents through suitable choice of driver functions b(t) (replacing the constant b in the analysis), we have not done so in this presentation. As one can see from RUNIN code runs, the assumption $I = \text{const.}$ is only very approximately satisfied during the pinch phase.

5. Dependence of Pinch Results on Initial Conditions

The wires and annular phases of the implosion determine the initial conditions for the pinch phase, and inasmuch as they depend on the generator current (assuming fixed current versus time profiles with variable amplitude), the optimizations for pinch radiation done at fixed initial state are not applicable for the total problem.

6. Ohmic Heating

While ohmic heating is negligible for strong implosions of low-mass loads, high-mass loads accelerate more slowly and may have much lower PdV heating rates. The smallness of the ohmic heating is also dependent on the assumption of fairly complete current penetration during the wires or annular phases; if the current is confined to a very thin sheath, ohmic heating power increases: $P_\Omega = 2\pi\ell\int\eta J^2 r\,dr = 2\pi\ell I^2/\sigma A_{curr}$ with conductivity $\sigma(T)$ and current-carrying area A_{curr}.

These cautions are pointed out as reservations which could be major in some implosions and some parameter ranges, but which are probably not so major in typical present-generation experiments. An attempt has been made to make simplifications to provide transparent calculations, without throwing out the more important physics affecting the scaling. We have also provided a quantitative evaluation of one important deviation from the idealized formulas (namely that due to radiative cooling). Other deviations, particularly at the higher load masses implied for very-high-current experiments are less easy to quantify; for example some of the opacity and radiation blanketing effects do not appear to be representable by simple algebraic formulas, thus necessitating (so far) case-by-case code calculations.

E. COMPARISON OF REQUIREMENTS FOR GENERATORS DRIVING RADIATION SOURCES AND FUSION TARGETS

Inelastic processes leading to nuclear fusion are strongly exothermic, whereas those leading to radiation are endothermic. Because of this difference, the nonadiabatic trajectories in lnr-lnT space for radiation and fusion targets curve away oppositely from the adiabatic trajectories. More important a fusion spark, i.e., a central region with enhanced temperature, tends to expand and propagate the fusion burn whereas central radiating spark (enhanced density, or temperature within limits) tends to radiatively cool and allow further compression, leading to a radiative pulse of increasing intensity, but decreasing energy per photon, and a non-propagating radiative burn because of the high photon transparency at low masses. (Thus quasi-adiabatic calculations tend to be overly pessimistic for fusion sources but overly optimistic for K-line radiation sources. The applicability of uniform-plasma approximations is poor for fusion burn, better but still questionable for radiation production.)

Another very important difference is that the critical temperature required for fusion reactions to proceed appreciably is much higher than that for the production of energetic radiation in a plasma of intermediate z, e.g., argon or aluminum; and the critical fusion temperature is an ion temperature whereas the radiation requires only sufficiently hot electrons which are generally easier to obtain. Subtracting D-T Bremsstrahlung energy loss from D-T fusion energy gain, the g(T)-equivalent energy production curve for a fusion neutron source has a broad maximum at 20-30 keV ion temperature, while aluminum K-line radiation peaks at 1 keV and argon at 2.4 keV. For present or near-term energy sources available to drive laboratory-scale implosions, this makes radiation sources much easier to achieve than fusion.

Hydrodynamic timescales in a fusion pellet are also faster than in a radiation source plasma because of the lower atomic weight of the fuel. This may result in power delivery requirements for fusion targets which are higher not only because of the need to achieve much higher temperatures but also because of the need to deliver the energy more abruptly to avoid pre-heating and/or ablating the fuel during the run-in phase of the liner or pellet.

In both fusion and radiation targets, pre-heat of the central region during the run-in phase is to be avoided because it reduces the peak achievable n^2; i.e., the greater the central pressure just before collapse of the liner/annulus/pellet, the softer the compression. Since blackbody radiation from the imploding plasma annulus can be a major contributor of central plasma preheat it is a truism that the annulus or shell should be kept as cool as possible during the run-in phase. But in fact one has rather little control of the ohmic heating of the shell or annulus except to deliver most of the driving power near the end of the run-in. In laser-driven implosions this is achieved by pulse tailoring; in electro-magnetically driven implosions it is more difficult because (1) the effective driver coupling is reduced once the implosion velocity is high (the effective electric field driving J for the JxB force is E+VxB/c, and although E increases, V and B tend to increase faster and cancel the E) and (2) voltage pulse tailoring on 10 ns timescales is technologically more difficult.

CHAPTER IV

SIMPLIFIED NON-LINEAR FIELD DIFFUSION

Electric or magnetic field diffusion into an initially unmagnetized plasma slab was modeled for a fixed plasma with temperature-dependent conductivity (e.g., $\propto T^{3/2}$) and with ohmic heating balanced by radiative heat loss of the form $Rn^{\beta}T^{\alpha}$ (R,α,β constants). Except if $\alpha = 3/2$, the temperature is then given by $JE = Rn^{\beta}T^{\alpha}$. The diffusion equation for the electric field E then takes the form

$$E'' - n^{-p}E^{q}\dot{E} = 0,$$

where p and q are related to α and β. This equation was solved for model n(r) profiles.

A. PROBLEM DEFINITION AND APPROXIMATIONS

The diffusion of magnetic field into a plasma is affected if the accompanying electric fields alter the plasma conductivity. Since ohmic heating raises the plasma temperature, the self-consistent field profile and the field penetration history can be quite different from the ususal diffusion model, but can be calculated if a suitable equation for T_e is available.

In general, two effects complicate the physics of the field penetration: fluid motion, i.e., momentum exchange with the field; and thermal conductivity, which makes the temperature equation a partial differential equation as well as the field equation.

But in certain limiting cases, including large ion mass, the plasma motion, including v x B back-EMF effects, can be ignored. And if thermal conductivity is sufficiently small so that inelastic excitation collisions dominate the heat loss, we get a local ordinary differential equation or algebraic equation for T_e, coupled to the partial differential equation for the field.

In a very simple case with fixed ions, quasineutral plasma, and negligible thermal conductivity, one may assume a quasistatic heat balance between ohmic heating and excitation cooling (the excitation energy is assumed radiated away in optically thin radiation):

$$\frac{3}{2}\frac{\partial}{\partial t}(n_iT_i + n_eT_e) = J.E - n_e\varepsilon_x\nu_x(T_e, n_o) \qquad [IV.1]$$

where $J = \sigma(n_e, T_e)E$ is the induced current density with conductivity σ (not necessarily scalar), ε_x is the excitation energy per ion (or atom), ν_x, the excitation rate, which depends on the number density n_o of ions or atoms than can be excited. If ionization is allowed as well as excitation, one has

$$\frac{3}{2}(n_i\dot{T}_i + n_e\dot{T}_e + \dot{n}_eT_e) = J.E - n_e\varepsilon_x\nu_x(T_e, n_o) - n_e\varepsilon_i\nu_i(T_e, n_o) \qquad [IV.2]$$

If the diffusion timescale is slow compared with the ionization and excitation times one can think of n_e as determined by T_e, i.e., when

$$\dot{n}_i = 0,$$

$$\dot{n}_e = \frac{\partial n_e}{\partial T_e}\dot{T}_e;$$

$$\frac{\partial}{\partial t}(n_eT_e) = n_e\dot{T}_e\left(1 + \frac{\partial \ln n_e}{\partial \ln T_e}\right) \qquad [IV.3]$$

with the logarithmic derivative term a function of T_e. We take $T_i = T_e = T$.

For $\sigma(n_e, T_e)$ we have $\sigma = (e^2/m)\,(n_e/\nu_m)\,F(\omega_c/\nu_m)$, with

$$\nu_m = n_e K_c' T_e^{-3/2} + n_n K_n' T_e^{1/2}, \qquad [IV.4]$$

$\omega_c = eB/mc$, K_c' and K_n' constants, and F approaching unity for small ω_c/ν_m. The last term of ν_m applies if neutrals are present. For the fully ionized plasma, σ has the form

$$\sigma = K_c T_e^{3/2}\,\bar{F}(\omega_c/n_e K_c' T_e^{-3/2}); \qquad [IV.5]$$

on the other hand, if neutral collisions dominate ν_m, then σ has the form $\sigma = K_n n_e T_e^{-1/2}$. To allow either case we let $\sigma = K n_i^{\gamma} T_e^{\delta}$, and assume $n_e \propto T_e^{\varepsilon} n_i(x)$ with some power ε, but restrict the magnetic field to values small enough that $\omega_c/\nu_m \lesssim 1/4$ so that $\bar{F} = 1$ and the conductivity is approximately scalar.

With the approximation that σE^2 and cooling $K_x n_i^{\beta} T_e^{\alpha}$ are nearly in balance, we can treat situations where $n_e \dot{T}_e \ll \sigma E^2$ and $K_x n_i^{\beta} T_e^{\alpha}$. Then, except if $\alpha = \delta$, we have

$$T_e(X,t) = \left(\left(\frac{K}{K_x}\right) n_i^{\gamma-\beta} E^2\right)^{\frac{1}{\alpha-\delta}} \quad \text{and}$$

$$J = K\left(\frac{K}{K_x}\right)^{q-2} n_e^{-p} E^{q+1} \qquad [IV.6]$$

where $q = \dfrac{2\delta}{\alpha-\delta}$ and $-p = \gamma + \delta\,\dfrac{\nu-\beta}{\alpha-\delta}$.

(A similar result {with different powers p and q} was also obtained for the "anomalously resistive" case where $J/n_e e$ is limited by the sound speed). So when n_e/n_i varies roughly as T^{ε} we have

$$\dot{J} = \sigma\dot{E} + \dot{\sigma}E = \left(\left(\frac{\alpha+\delta}{\alpha-\delta}\right) K \left(\frac{K}{K_x}\right)^{q/2}\right) n^{-p} E^{q} \dot{E}. \qquad [IV.7]$$

This leads to a PDE of the form

$$E^{q}\dot{E} = C\, n^{p}(x)\, \partial_{x}^{2} E, \qquad [IV.8]$$

(the dot indicates $\partial/\partial t$), to which we apply boundary conditions $E(-\infty) = E_o$ and $E(+\infty) = 0$, and initial conditions

$$E_o(x) = \begin{cases} E_o \text{ for } x < x_1 < 0 \\ E_o \exp-(x - x_1)^2/\Delta^2) \text{ for } x > x_1 \end{cases} \qquad [IV.9]$$

choosing x_1 close enough to where $n(x) = 0$ so that the $\ddot{E}$ wave term is still negligible compared with the $\dot{\sigma}E$ and/or $\dot{E}\sigma$ terms. A 1D slab model was used and $n_i(x)$ was given time-dependent function of x. In the wave-diffusion equation, $\nabla x \nabla x E + \ddot{E}/c = -(4\pi/c^2)(\dot{\sigma}E + \dot{E}\sigma)$, the $\ddot{E}$ wave term was dropped. We assumed one of two forms for $n_i(x)$; a step function $n_i = n_{io}H(x)$, or a Guassian, $n_i = n_{io}\exp(-x^2/h^2)$.

B. NUMERICAL SOLUTION

The resulting nonlinear diffusion equation for these simple approximate cases was solved using a 1D finite-difference computer code, fully flux-conserving, employing a fully implicit method with tridiagonal matrix inversion. The code was run for a time equal to four initial magnetic diffusion times for the Gaussian plasma, on a fifty-point uniform spatial grid. Because the wave term was not kept, the solutions are not quantitatively correct far from the plasma. The Courant stability condition, $\Delta t < \Delta x^2/D$, was not satisfied at the foot of the pulse when $D(E)$ had a pole at $E = 0$, but the model equations are not strictly valid in that limit because the conductivity and temperature do not actually go to zero when E goes to zero at the diffusion front. On the timescales of interest, this failure to satisfy the Courant condition at the front did not make important changes in the overall field diffusion history.

C. INTERPRETATION OF SOLUTIONS

The solutions for an ionizing Argon plasma with Coulomb collisions and excitation of ion lines ($\beta=2$, $\gamma=0$, $\delta=3/2$) are compared with the solutions of the standard textbook case, $\dot{\sigma} = 0$, in Figure IV.1 and IV.2. Where n_i is not small, the buildup of plasma conductivity (for $\alpha > 3/2$) tends to short out the field penetration and steepen the gradient of E. In the absence of other effects, we would interpret this as evidence that (1) the bulk field diffusion in such a plasma is slower than the rate indicated by the magnetic diffusion time $4\pi\sigma_o h^2/c^2$ but (2) the diffusion of the "foot" of the field profile is much faster than for the constant-σ case because the conductivity and temperature are low near the foot.

For α less than about 3 in the radiation/excitation T^α dependence, the nonlinearity of the diffusion, E^q, with $q = 3/(\alpha-3/2)$, can be quite strong and sensitive to α; for Argon at $n_i \sim 10^{20}\,\mathrm{cm}^{-3}$ and $T_e = 50\text{-}150$ eV, q was 0.91 and the nonlinearity was moderate.

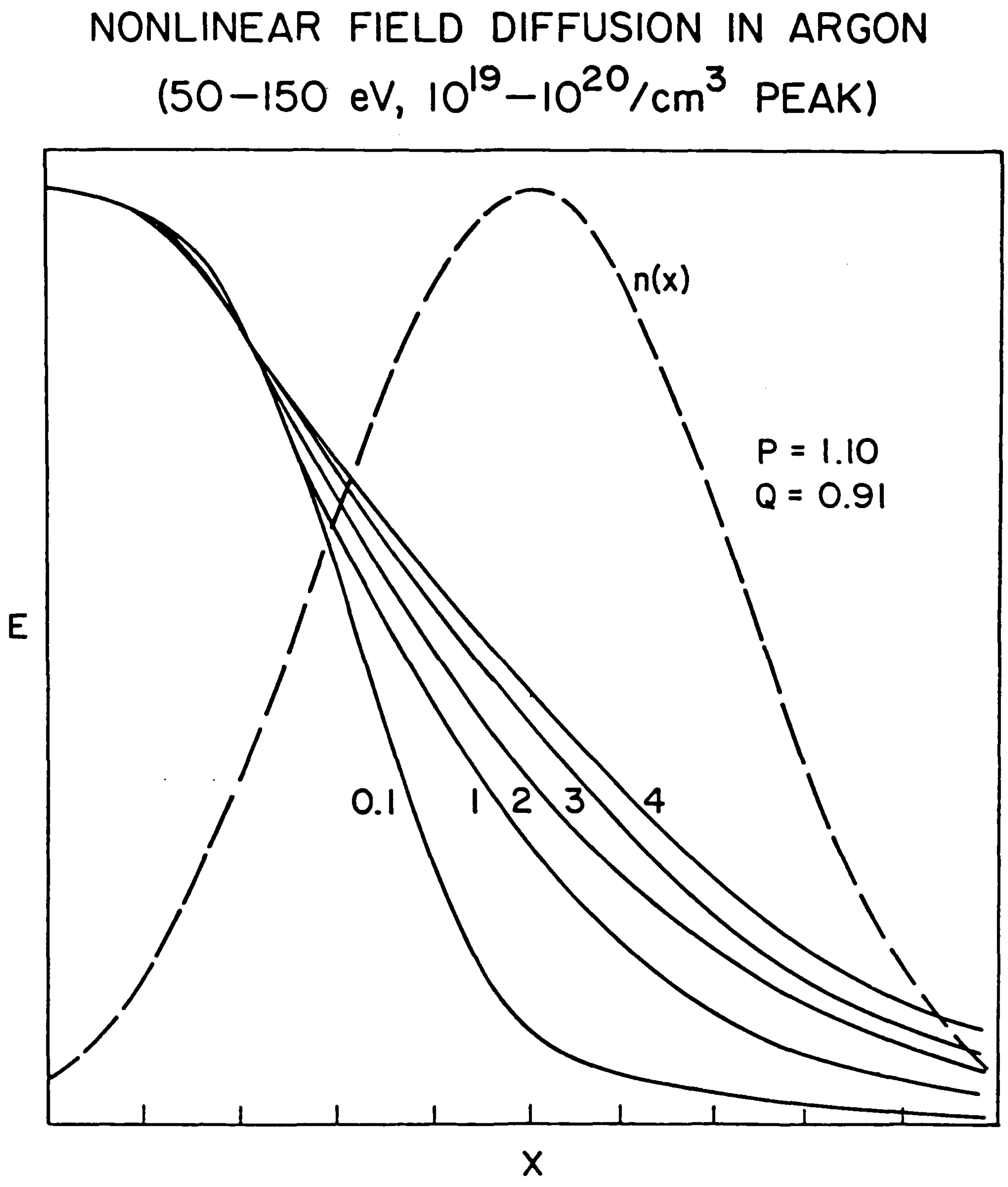
NONLINEAR FIELD DIFFUSION IN ARGON
(50–150 eV, 10^{19}–10^{20}/cm^3 PEAK)
n(x)
P = 1.10
Q = 0.91
E
0.1
1
2
3
4
X

Figure IV.1

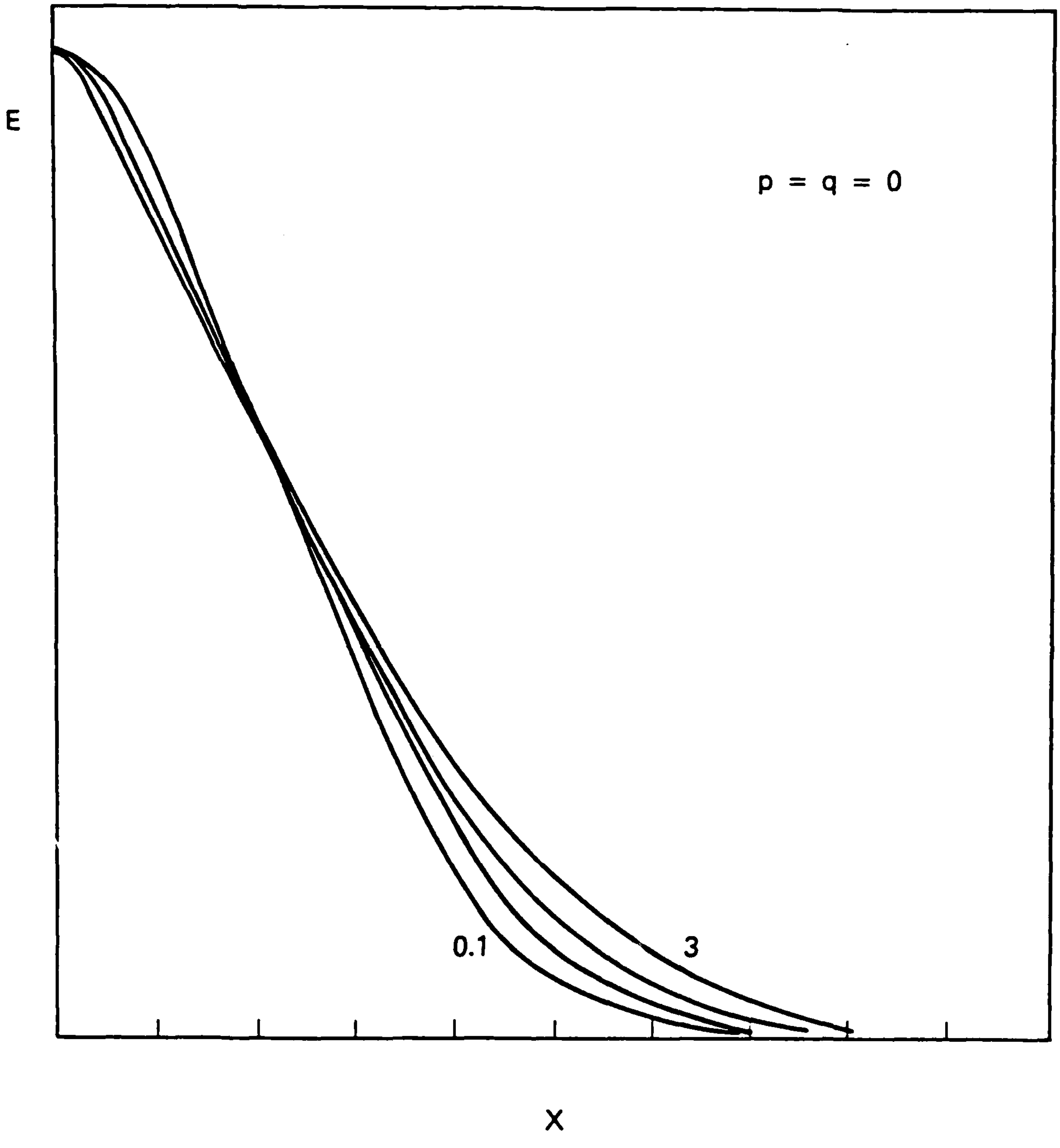

Figure IV.2. Normal diffusion (i.e., with density-independent, field-independent diffusion coefficient) into the Gaussian density profile of Figure IV.1.

This field model calculation was also applied to a weakly ionized region in a uniform neutral medium, with electron-neutral collisions dominating ($\gamma = 1$, $\delta = -1/2$, $\langle \sigma v \rangle \propto T^{1/2}$) and with excitation of neutrals ($\beta = 1$). Here $p = -1$ and $q = -1/(\alpha + 1/2)$. Again the diffusion was compared with the $\dot{\sigma} = 0$ case. Here increasing T_e reduces the conductivity and enhances the diffusion rate instead of impeding diffusion, but the nonlinearity is weaker.

At higher temperatures, when α is not much larger than δ, i.e., when the temperature-dependence of the excitation cooling is not much different from that of the conductivity, excitation fails to clamp the electron temperature at a well-defined value, and the $\dot{T}_e$ term in

$$n_e \dot{T}_e = G(T_e)\left(\sigma E^2 - K_x n_e^{\beta} T_e^{\alpha}\right) \qquad [IV.10]$$

is not necessarily small compared with the right-hand source and sink terms. The equation in this case may fail to specify a temperature algebraically, especially when $\sigma \propto n_e^{\beta}$ as well. and it must be integrated in time simultaneously with the E field equation.

With the more advanced MHD code discussed in Part II of this report, we are also exploring other effects, including those of self-consistent magnetization in the conductivity, thermal conduction, fluid motion, etc., which allow a broader range of penetration phenomena for the electric field.

D. CAVEATS TO THE FOREGOING NONLINEAR DIFFUSION STUDY

To assess the importance of ohmic heating and plasma blowoff, and to predict the dynamics of the assembled pinch plasma if ohmic heating is important, it is necessary to have some knowledge of the field penetration depth into the plasma. The process is clearly affected by nonlinear features as just described, but also by other features not included. Perhaps the most important of these is magnetization of the conductivity, which raises the effective resistivity just behind the field penetration front and hence favors current flow on the front where the field is still low. This probably tends to enhance the effective diffusion rate of field.

Second, preliminary results from the 1D code described in Part II of this report show that the plasma motion, not fully considered here, is important not only in reducing the effective electric field by v X B (which is easily included in this model, taken in the plasma moving frame) but also in causing compression (nonuniform motion) of the plasma. Finally, thermoelectric fields are set up, as shown by the 1D code and these tend to make a plasma which is overdriven (where E is large) transmit the force and cause generator action in its interior, setting up magnetic fields due to the resulting axial current filament. This may explain a feature commonly observed in the plasma focus, namely pitting of the cathode on the axis (presumably by an ion current filament); but such thermoelectric effects cannot be included in the simple model explored in this section.

In addition to these caveats there are the mathematical limitations of the model. Temperature is increased by ohmic heating but does not vanish at the field front where ohmic heating vanishes. The radiation, at interesting temperatures, often does not have a simple power-law fit.

The model above may be useful as a step in describing field penetration in massive higher-Z structures associated with plasma implosions but probably does not show the dominant features of field penetration versus field push in gas puff plasmas.

CHAPTER V

SUMMARY OF PART I

This half of the report describes a simple "scoping" code for describing imploding plasma radiators, scaling laws for energetic radiation from imploded plasmas, and an effort to model the nonlinear field penetration in the early stages of plasma implosion, as the plasma heats.

RUNIN CODE SUMMARY

Runs WIRES (optional), then BRIDGE (annular plasma), then SQUEEZE (pinch phase).

A. WIRES

1. Evolves position, size, temperature and current for N identical wire plasmas.
2. Pre-BBE: wires fatten at sound speed.
   BBBE: blackbody (BB) radiative cooling balances ohmic heating, and with Bennet equilibrium (BE), determines size and temperature of individual wire plasmas.
3. Wire centers move inward via $F = ma$, F determined by current I/N in each wire (N wires, total current I) and radius of centers r_c. Current I comes from given voltage V(t) via circuit equation including generator impedances.
4. Merge Condition: When wire plasmas touch.
   Merge: Replaces wires by annular shell of same mass, volume, temperature, RMS position and inward velocity.

B. BRIDGE

1. Evolves outer and inner radii, temperature and current of a uniform annular plasma shell driven by V(t) via circuit equation. Uses variable-timestep ODE solver DGEAR to advance the variables.
2. In force equation, current is treated as if acting at outer surface.
3. Inner radius evolved approximately by moving away from outer surface at a speed related to the sound speed (as one possible model).
4. Quasi-transparent radiative cooling (limited by blackbody rate), and ohmic and compressional heating, not necessarily in balance.
5. Keeps log of integrated radiated energy loss and energetic photon loss.
6. Closure condition: inner radius $< 10^{-6}$ cm.
   Closure: set inner radius to zero and go to SQUEEZE, passing it the outer raduis, velocity, temperature, current, etc.

C. SQUEEZE

1. Evolves compression of uniform plasma cylinder driven by voltage V(t) and circuit equation, including quasi-transparent radiative loss. (Uses DGEAR.)
2. Self-similar motion, driven by force at surface.
3. Temperature equation includes compressional, deceleration and ohmic heating, and quasi-transparent radiative cooling (limited by blackbody rate). As elsewhere, ionization state is controlled instantaneously by temperature.

4. Continues log of integrated radiative energy loss (Y^{TOT}) and energetic photon loss ($Y^{>}$).

RADIATIVE SCALING LAWS SUMMARY

Assumptions:

1. Almost all the interesting radiation occurs during the pinch phase.
2. The plasma is uniform (including isothermal).
3. Interesting radiation is transparent and instantaneous. Power $P_{rad} = \pi r^2 \ell\, n^2 g(T)$, where n = ion number density, T = electron and ion temperature, and $g(T)$ is a known function (e.g., from the NRL model).
4. Perturb about adiabatic (nonradiative) compression.
5. Initial pinch conditions depend on history of the annular plasma and wire plasma stages.
6. Current I is used (in lieu of voltage) as a scaling variable, since the compressional forces depend on I^2.

Fundamental Formula:

$$Y^{>} = \int_0^t n^2(t) g(T(t))\, \pi \ell r^2(t) dt = \frac{m/m_i}{\pi \ell} \int \frac{g(T(t))dt}{r^2(t)}$$

since $n = (m/m_i)/(\pi r^2 \ell)$. Here $Y^{>}$ is the time-integrated energetic-photon yield, ℓ is the pinch column length, $r(t)$ is the outer radius of the pinch cylinder, $T(t)$ is the temperature, $g(t)$ is the known radiation function, $n(t)$ is the ion number density, m is the total load mass and m_i is the mass of one ion.

Fundamental Approach:

1. Radius $r(t)$ and temperature $T(t)$ are given to first approximation by adiabatic compression. (Perturb about this.) Compression is driven by $b \equiv \ell I^2/m$, assumed nearly constant during the pinch phase.
2. Find conditions maximizing $Y^>$ and show how they scale with $\ell I^2/m$ and initial conditions of the pinch, to lowest order (quasi-adiabatically).
3. Extend to next order in non-adiabaticity.

Primary Results:

1. There is an optimum value of $\ell I^2/m$ for any atomic element:

$$I_{opt}(\mathrm{MA}) = 300\ \left[\frac{m}{\ell}\left(\frac{g}{cm}\right)\ T_{pk}(\mathrm{keV})\Delta^{-1}\right]^{1/2} \qquad [\mathrm{III.46}]$$

   where $\Delta = \varepsilon_1/b + \ln(T_{pk}/T_1)$ depends on initial conditions, and T_{pk} is the maximum of the given $g(T)$ curve for the element. ε_1 is the kinetic energy at the beginning of the pinch stage, and is roughly proportional to $b \equiv \ell I^2/m$.
2. If $\ell I^2/m$ is chosen to have its optimal value, $Y^>$ can be expressed as a function of either $\mu \equiv m/\ell$ or I. Doing the former,

$$Y^>_{opt}(J) = 0.2\mu^2 \ell (T_{pk}/T_1)^{N/2}\left[r_1(\mathrm{cm})\sqrt{T_1(\mathrm{ev})}\right]^{-1}$$

$$\left[10^{42} g_{pk}(\mathrm{W\ cm^3})\right] A_m^{-2}\ K \qquad [\mathrm{III.49}]$$

where A_m is the atomic mass number (a.m.u.), K is a dimensionless number of order unity (see text) and N is a constant or order 1/2, related to the adiabatic index. (If $T/T_1 = (r/r_1)^{-C}$, then $N = 2C^{-1} - 1$.)

3. If one chooses to express $Y^{>}_{opt}$ in terms of I rather than μ, one finds $Y^{>}_{opt} \propto I^4$, to zeroth order in the radiative loss. This agrees with observations and simpler scaling models[8].

4. In the next-order approximation, where radiative energy loss is a non-negligible perturbation of adiabatic behavior, $Y^{>}_{opt}$ falls below μ^2 or I^4 scaling. The ratio of $Y^{>}$ to the peak thermal energy content of the load is a natural scaling variable if the pinch phase is hot enough for energetic photons to dominate the radiative loss rate. Let this ratio be called Y. Then to first order in Y, the minimum radius (peak compression) of the pinch is unaltered, but the peak temperature is lowered by a factor

$$\exp -(Y/2)F \qquad [III.79]$$

where F depends on the adiabatic index C and on the peak temperature. A higher current is thus needed to reach the optimal radiating temperature than in the quasi-adiabatic limit, and this translates to a scaling slower than μ^2 or I^4 at large I or μ.

NONLINEAR DIFFUSION SUMMARY

For a noncompressing plasma in radiation equilibrium (i.e., where ohmic heating is balanced by radiative cooling), we examined classical field penetration, affected by the changing conductivity of the plasma as it is heated by the penetrating field. This diffusion, in a medium where the diffusion coefficient depends on the field, shows quantitative differences from the usual constant conductivity field diffusion problem. The differences depend of course on how the conductivity changes with field, and this in turn depends on the radiative properties. Field diffusion in Argon with a Gaussian density profile peaking at 10^{19} - 10^{20}cm^{-3} and with temperatures 50 - 150 eV was modeled with a 1D nonlinear diffusion code. Although conductivity build-up in the plasma somewhat steepened the diffusion front, the foot of the field profile moved more rapidly than for the constant σ case because the conductivity and temperature are low near the foot. This study may have some applicability to the early-time field penetration in gas-puff plasmas, and to the location, thickness, and freezing-in of the current layer, although in the real situation plasma compression (not modeled here) is probably equally important.

REFERENCES FOR PART I

1. J. Guillory and R.E. Terry, "Modeling of Imploded Annular Plasmas-Annual Report, April 1982." JAYCOR report J207-82-009.

2. D.A. Tidman and D.G. Colombant, "Diode Imploded Annular Plasmas and Coronal Superheating," JAYCOR Report J78-1069-JC, June 1978.

3. IMSL Library Reference Manual, IMSL LIB-0007, Vol. I, Chap. D. IMSL Corp., Houston, Texas, 1979.

4. D. Duston and J. Davis, "Soft X-ray and XUV Radiation from High Density Aluminum Plasmas," Phys. Rev. A21, May 1980.

5. R.E. Terry and J. Guillory, "Annual Report on Modeling of Imploded Annular Plasmas," JAYCOR Report J207-81-004, January, 1981.

6. R. Pol, D. Fisher, T. Wilcox, S. Wong, H. Sze, L. Deraad and W. Tsai, "Experiments on Multiple Wire Arrays," Report RDA-TR-113301-002, R and D Associates, February 1980.

7. P. Kepple, private communication; also see Part II of this report.

8. e.g., C. Gilman et al., Advanced Concepts Program, Quarterly Report Physics International Report PIQR - 1481 - 4, February 1982.

ACKNOWLEDGEMENT

It is a pleasure to acknowledge the assistance of Dr. Dan Spicer in the 1D nonlinear diffusion code used in Chapter IV.

PART II

CHAPTER I

OVERVIEW OF THE ELECTRODIFFUSIVE MHD MODEL FOR THE IMPLODING PLASMA RADIATOR

Present efforts in the modeling of imploding plasma radiators are centered on the study of electrodiffusive, radiatively coupled MHD theory as the basic tool needed to understand the role played by each of the plasma properties in shaping the implosion trajectory, emission profile, and radiation pulse observed in the laboratory. The primary points of interest in the plasma behavior are two-temperature effects during compression, chemical potential and ionization profiles, thermoelectric effects on axis at assembly, and the modes of current penetration. The main points of interest in the interaction between the plasma load and the diode are the validity of the diffusion approximation, the structure of the plasma-to-vacuum transition, the fraction of power absorbed by the load relative to that reflected, and the resolution in spacetime of various sources of reflected power. Of equal interest is the development appropriate computational techniques and software with which, first, to answer these questions and, then, to admit a smooth extension onto a much wider application domain. In order to obtain this kind of capability it is necessary (i) to select carefully the minimal set of fields to propagate, (ii) to optimize the time integrations with respect to the number of derivatives needed, and (iii) to encompass a wide dynamic range in number density and radius. All of the considerations just set forth interact and usually conflict to some degree. Moreover, as shown in later

PREVIOUS PAGE IS BLANK

sections, the acute nonlinearities in the physical theories both help and hinder various aspects of the task. The present means to all these ends is the implosion code ZDIPR (Z-Driven Imploding Plasma Radiator); the remainder of this chapter is devoted to a summary of its evolved configuration and performance over the past year.

A. ARCHITECTURE OF THE IMPLOSION CODE

ZDIPR may be rationally subdivided into three major subroutine groups - the physics package (FLUIDOTS/TETDOTS), the mesh integrator (GRIDROOT), and the subcycle integrator (GEARBOX/TETGEAR). The major portion of the code and the notation appearing in later discussions have been documented in Reference 1, referred to as the "original formulation" for the remainder of this report. The present discussion is intended to be a topical updating of specific points, although some recapitulation is included.

(1) The physics package consists of a plasma model and a field model. The plasma model employs both ion and electron temperatures, a radial flow field and complete, fully magnetized transport coefficients. Theromelectric fields and heat fluxes and appropriate drift speed limits on J_z have been included from the outset, and flux limits appropriate to thermal conduction and possible thermoelectric deficiencies have been added. The equation-of-state and radiation package is a faithful mimic of CRE results for ionization states and chemical potential, and utilizes a four frequency bin "probability-of-escape" radiation transport scheme. The field model discussed and explored here is the electro-diffusive option, which is a good first approximation when

detailed balance of incoming and outgoing waves does not fail[1]. The presently evolved forumlation also has the singular advantage of checking its own validity.

(2) The mesh integrator is now a new continuously-variable-step predictor/corrector accurate through second order. Corrector convergence is achieved through regula-falsi or replacement to high precision (10^{-8}). This purely iterative convergence scheme eliminates the need for a mesh Jacobian and the attendant machinery for factoring and substituting, in contrast to the present subcycle integrator.

(3) The subcycle integrator (TETGEAR) for the electro-diffusive option requires as input, at various t^* in the subcycle, the material derivatives generated by the physics package (TETDOTS), which in turn requires the advanced mesh and velocity fields generated at t^* by the mesh integrator (GRIDROOT). Each derivative call by the subcycle integrator thus requires a full update of the mesh to the intermediate time point--the primary motivation for the continuously variable step integrator.

This sort of subcycle derives from the observation that a spacetime p.d.e. which has the derivative operations represented by discrete differences on one domain of dependence appears as a coupled set of o.d.e. on the orthogonal domain. The particular case here is that of spatial differential operators, corresponding to finite difference operators (derived through conventional or smooth interpolants), producing a set of coupled equations on the time domain. In all such cases the coupling of the time derivates is expressed as a Jacobian matrix, implicitly dependent on the mesh used to discretize the spatial derivative operators. Here the time derivatives are the material derivatives $\{\dot{T}_e$,

$\dot{\theta}_e$, $\dot{E}_z$} and the underlying mesh motion {r, $\dot{r}$, $\ddot{r}$, $\dddot{r}$} is completely transparent to the subcycling algorithm.

For the electrodiffusive field model the subcycle variable set advanced by TETGEAR consists of ${}^{i}Y_j = \{\ldots {}^{i}_{c}T_{I,j}, {}^{i}_{c}E_{zj}, {}^{i}_{c}\theta_{ej} \ldots\}$ a total of 3·J initial/boundary value problems with J the number of hydrodynamic cells. The prescript "c" indicates evaluation at the spatial cell centers. All external driving terms enter as a boundary condition on ${}^{*}_{c}\dot{E}_j$ based on the circuit equation appropriate to the particular diode being modeled. In the environment seen by TETGEAR, the problem is specified completely by the input $\{{}^{i}Y_j\}$, the interior material derivatives $\{{}^{*}\dot{Y}_j\}$, the coupling matrix ${}^{*}(\partial\dot{Y}_i/\partial Y_j)$, and the intermediate time points τ^{*}.

The combined fluid evolution subroutine HYDROPUSH incorporates the three foregoing elements and forms the nucleus of ZDIPR-apart from startup, diagnostic and graphics modules. HYDROPUSH is concerned exclusively with the advance of <FLUID-STATE> over the variable major time step which it selects as appropriate. The only required inputs are the common blocks <FLUID-STATE> and <FIELDADVDATA> (containing the previous time slice of fluid variables and field variables) and the appropriate mesh dimension, scale factors and physical constants, obtained from a variety of sources. The output is an update of <FLUID-STATE>, and an increment of the variable MSI (Main Step Index) by 1. If a restart file is desired, it is created for later use and assigned a record number equal to the MSI. If any severe errors occur in the advance, dump files are created to allow examination of intermediate results, and a variety of reports at intermediate phases of the calculation are available as general diagnostics.

The sequence of processing begins by reading elements of the <FLUID-STATE> into <MESHADVDATA> and the subcycle vector $\{{}^{i}Y_{j}\}$. Once the appropriate data base is inferred a full complement of material derivatives is computed, by FLUIDOTS/HERTZDOTS or in the electrodiffusive mode by TETDOTS. These material derivatives are then used by STEPPER to select a major timestep. For restart purposes, the environment of either GEARBOX or TETGEAR is output at this point if requested. Then a single subcycle is done (advancing ${}^{i+1}Y_{j}$, ${}^{i+1}r_{j}$ and ${}^{i+1}\dot{r}_{j}$) and the new FLUID-STATE is output. The iterative refinement of the mesh evolution is now accomplished within the calls to derivative module. The general structure of HYDROPUSH is illustrated in Figure I.1; the details of the timestep selection algorithms are discussed in the original formulation.

B. MILESTONES AND ROADBLOCKS

To date we can report rather firm progress in bringing two of the major subroutine groups into a state of development which is adequate for the goals set forth above and in the original formulation. The calculation of self-consistent material derivatives is now routinely done to very high precision. This capability is documented below in Chapter II. A singular difficulty in obtaining this result was the strong nonlinearity in the Braginskii thermoelectric theory, but this has now been tamed and at least partially understood as a possible basis for corrections to that theory.

FLOW OF A SINGLE SUBCYCLE: *HYDROPUSH*

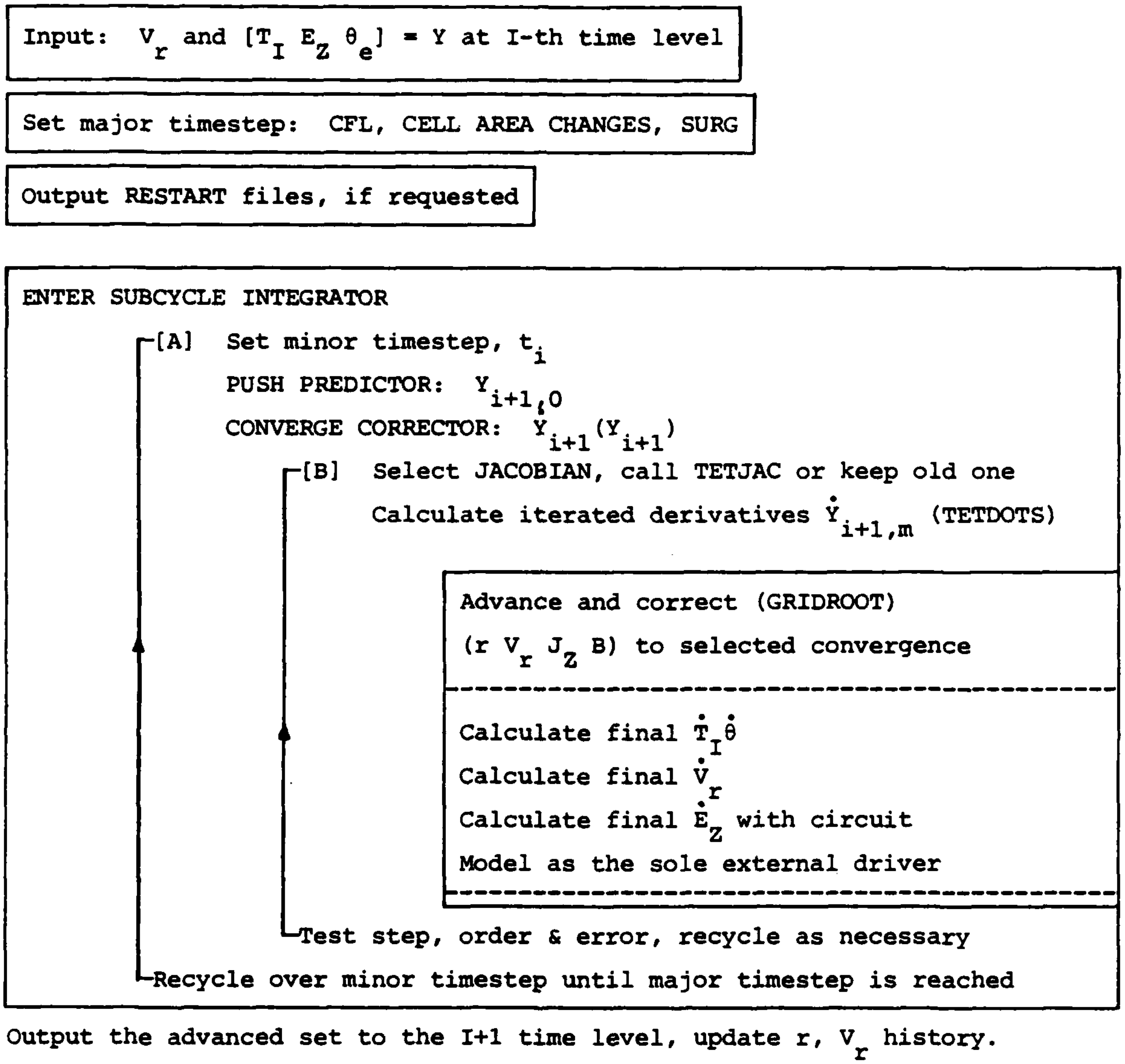

Input: V_r and $[T_I \; E_Z \; \theta_e] = Y$ at I-th time level

Set major timestep: CFL, CELL AREA CHANGES, SURG

Output RESTART files, if requested

ENTER SUBCYCLE INTEGRATOR

[A] Set minor timestep, t_i

PUSH PREDICTOR: $Y_{i+1,0}$

CONVERGE CORRECTOR: $Y_{i+1}(Y_{i+1})$

[B] Select JACOBIAN, call TETJAC or keep old one

Calculate iterated derivatives $\dot{Y}_{i+1,m}$ (TETDOTS)

Advance and correct (GRIDROOT)

$(r \; V_r \; J_Z \; B)$ to selected convergence

Calculate final $\dot{T}_I \dot{\theta}$

Calculate final $\dot{V}_r$

Calculate final $\dot{E}_Z$ with circuit

Model as the sole external driver

Test step, order & error, recycle as necessary

Recycle over minor timestep until major timestep is reached

Output the advanced set to the I+1 time level, update r, V_r history.

Figure I.1

Also completely operational is the mesh integrator, documented in Chapter III. The development of these new integration filters grew from the great sensitivity of the subcycle integration to the space-time jitter in the velocity field. Their subsequent introduction in a fully implicit implementation has improved the quality of the model significantly.

The primary obstacle to efficient operation is the subcycle integrator DGEAR, essentially unchanged from the version supplied by IMSL. While the integrator DGEAR offers several control parameters and considerable flexibility in the integration scheme, the most useful options have been the use of explicit Jacobians and the control of the local truncation error through a variable TOL. The explicit Jacobian is the most favorable option in this hydrodynamic application; but, since the physics detail in ZDIPR demands a very expensive analytical evaluation of this matrix, an estimate based only on finite differences is needed. We find that the choice of the differencing algorithm is a sensitive one relative to subcycle integrator performance. The variable TOL provides a natural and consistent means of specifying time integration parameters, but it does not split up into separate error bounds for truncation and corrector, and this causes trouble. The integration scheme can be selected as either an implicit Adams method of up to twelfth order or a backward differentiation method of up to fifth order (Gear's stiff method). Both methods are of the implicit linear multilevel type and require the solution of an algebraic system at each interior (subcycle) timestep. Here the optimal choice between the two seems to fall to Gear's stiff method. The motivation for its use-treatment of stiff terms in the heat and field diffusion equations-therefore appears well grounded; but the error estimates the step size controls, and the dependence on a Jacobian matrix (and its inverse) for corrector convergence appear to contain some systematic and serious difficulties in this application. The problems are being addressed by a variety of alternatives and the resolution of these questions will be best assured by careful further testing.

Despite the difficulties in obtaining efficient integration, the model can be fruitfully applied in short simulations. Chapter IV describes the results of one such calculation meant to examine the early boost phase of the plasma implosion.

CHAPTER II

SELF-CONSISTENT CALCULATION OF THE MATERIAL DERIVATIVES (FLUIDOTS/TETDOTS)

A number of modifications to the original formulation have been necessary in the course of the code development over this contract year. These changes have been motivated primarily by the need for high precision in the difference-equation image of the time derivatives. The better resolution of the global couplings (in space) for each temporally evolved quantity, as provided by this high precision, has been found very helpful in improving the subcycle integration.

A. STATEMENT OF THE PROBLEM

The physical content of this model has been laid out in the original formulation and in previous documents. However, in order to clarify the present discussion, the major fluid and field evolution relations are summarized below for the electrodiffusive limit that has been the central focus of recent efforts. The notation is unchanged from that introduced in the original formulation.

If one gives up some information concerning the details of the diode fields and makes the assumption that the incoming and outgoing wave components are in detailed balance, then the Hertz wave equation can be transformed to a diffusion equation

$$\frac{D}{D\tau} E = \{u^{-1} \partial_u \, u \partial_u E\} \frac{1}{4\pi\Sigma} - \hat{E}\partial_\tau \ell n \, \Sigma - \partial_\tau E_{th} - B\partial_\tau \beta, \quad [II.1]$$

where E_{th} is the dimensionless thermoelectric field, Σ is a dimensionless conductivity, $\beta = V_{fluid}/c$, $E' = E + \beta B$, $\hat{E} = E + \beta B + E_{th}$, and $D/D\tau = \partial_\tau + \beta\partial_u$.

The fluid response to the electromagnetic stresses and heating is embodied in the relations

$$\frac{D}{Dt} V_r = -\frac{\tilde{T}}{\tilde{m}} \partial_r \ell n \, n_I - \frac{\partial_r \tilde{T}}{\tilde{m}} - \frac{J_z B_\beta}{\tilde{m} c n_I} + \frac{\rho E_r}{\tilde{m} n_I} \quad [II.2]$$

and

$$\frac{D}{Dt} \Theta_e = -\frac{2}{3} T_e (\nabla \cdot V) + \{\nabla \cdot (\chi_e \partial_r T_e) + \nabla \cdot (\beta_\Lambda^{Tu} U_z)\} \left(\frac{3}{2} \mathfrak{Z} n_I\right)^{-1}$$

$$+ \frac{2}{3\mathfrak{Z} n_I} (J_z \cdot E_z') + \frac{2m_e}{m_I} \left(\frac{T_I - T_e}{\tau_e}\right) + Q_{Rad}, \quad [II.3a]$$

$$\frac{D}{Dt} T_I = -\frac{2}{3} T_I (\nabla \cdot V) + \left(\frac{3}{2} n_I\right)^{-1} \nabla \cdot (\chi_I \partial_r T_I) + \frac{2\mathfrak{Z} m_e}{m_I} \left(\frac{T_e - T_I}{\tau_e}\right) \quad [II.3b]$$

In these expressions $\theta_e = T_e + 2/3\varepsilon_I/\mathfrak{Z}$, $\tilde{T} = T_I + \mathfrak{Z} T_e$, $\tilde{m} = m_I + \mathfrak{Z}_{max} m_e$; $\chi_{e,I}$ is the thermal conductivity, τ_e the plasma relaxation time, E_r the ambipolar radial field (with ρ its induced charge density), and Q_{rad} is the net (local) radiative heating or cooling. The dimensional version of fields are subscripted with a vector component; dimensionless fields are not. The radial electric field is established as a solution to an integral equation derived from the radial component of Ohm's law. The drift-speed-limited current condition is supplemented by a (nonlinear) change in Σ where the local E field requires it.

The (nonuniform) time levels for any variable are indexed with a leading superscript; the Lagrangian fluid mesh is denoted by r, and its material derivatives by a superscripted dot (or dots). Spatial indexing is denoted by trailing subscript and various cell-to-cell averaging operations are denoted by an overbar or by angle brackets.

The data base for all the hydrodynamic calculations is the common block <FLUID-STATE>, containing $\{N_j, {}^{c}_{i}T_{I,j}, {}^{i}_{c}\theta_{e,j}, {}^{i}r_j, {}^{i}\dot{r}_j\}$ and $\{{}^{i}_{c}E_{z,j}\}$, the diffusing electric field. An update of the <FLUID-STATE> and E_z is the central result of a major timestep. The relationships among the basic fluid variables on the Lagrangian mesh are illustrated in Figure II.1. The simple two and three point area-weighted differencing schemes for such a mesh were discussed previously. The numbers of cell ions $\{N_j\}$ are a conserved vector of ions/cm resident in the (compressible) cell $[{}^{i}r_j, {}^{i}r_{j+1}]$, assuring strict particle conservation and a solution of the equation of continuity limited in accuracy only by the evolved values of $\{{}^{i}r_j\}$. The elements of $\{N_j\}$ are assigned spatial locations given by the cell center position (defined by the equal area point) ${}^{i}_{c}r_j = (1/2({}^{i}r^2_{j+1} + {}^{i}r^2_{j+1})/2)^{1/2}$.

In general, at any point t^* (selected by the subcycle integrator) within the subcycle $[t_{lo}, t_{hi}]$, one must map $\{{}^{*}t, {}^{*}_{c}T_{Ij}, {}^{*}_{c}E_{zj}, {}^{*}_{c}\theta_{ej}\} \rightarrow \{{}^{*}_{j}\dot{T}_{Ij}, {}^{*}_{c}\dot{E}_{cj}, {}^{*}_{c}\dot{\theta}_{ej}\}$ in such a way that the intermediate fields $\{{}^{*}r_j\ {}^{*}V_{rj}\ {}^{*}_{c}B_{\theta j}\ {}^{*}J_{zj}\}$ are all consistent with one another. Only the time can enter as a generator of ${}^{*}r_j$ and ${}^{*}V_{rj}$, however these fields are calculated, because of the Lagrangian nature of the mesh. The calculation of these position and velocity coordinates is discussed in Chapter III and they will be considered given for the remainder of this discussion. Although the ${}^{*}V_{rj}$ and ${}^{*}_{c}B_{\theta j}$ calculations must be considered coupled problems, a magnetic field calculation from any given velocity profile is the pivotal element in achieving the desired self-consistency.

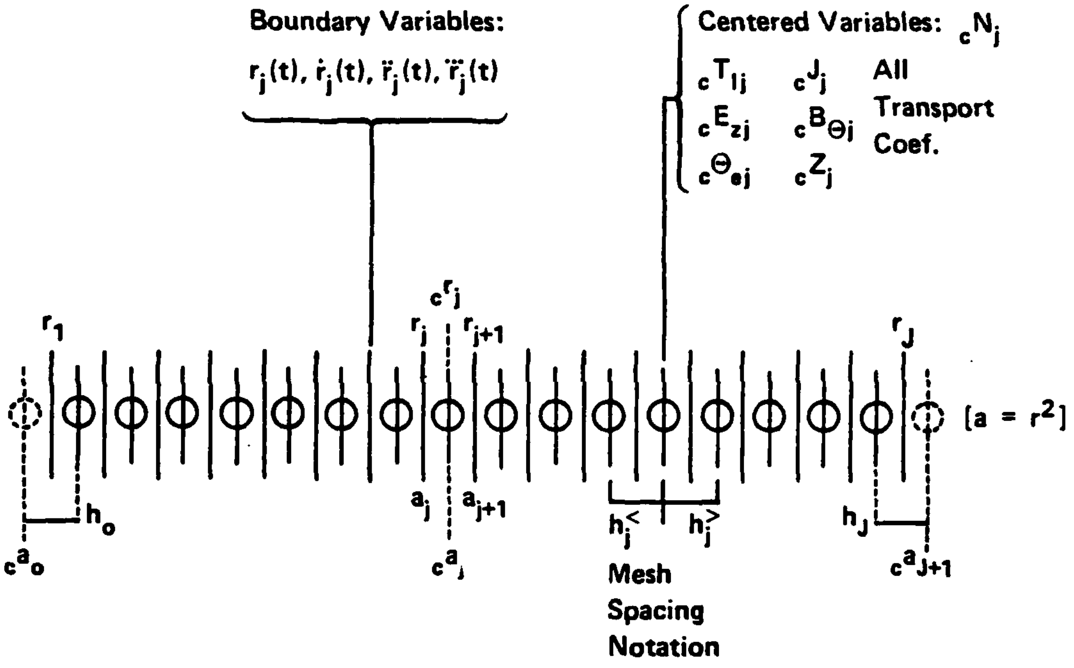
Boundary Variables:
$r_j(t), \dot{r}_j(t), \ddot{r}_j(t), \dddot{r}_j(t)$
Centered Variables: $_cN_j$
$_cT_{Ij}$
$_cJ_j$
All Transport Coef.
$_cE_{zj}$
$_cB_{\Theta j}$
$_c\Theta_{ej}$
$_cZ_j$
r_1
$_cr_j$
r_j
r_{j+1}
r_J
$[a = r^2]$
h_o
$_ca_o$
a_j
a_{j+1}
$_ca_j$
$h_j^<$
$h_j^>$
Mesh Spacing Notation
h_J
$_ca_{J+1}$

Figure II.1. The Lagrangian Fluid Mesh.

B. THE MAGNETIC FIELD COMPUTATION

If the mesh and its velocity are presumed given, or at least provisionally established subject to iterative refinement, then there is just one magnetic field profile (and its curl, the current density) which is compatible with this mesh and the input electric and temperature fields. Because of the great sensitivity of the transport coefficients (in this often highly magnetized model plasma) to the value of ${}_c\overset{*}{B}_{\theta j}$, the stability and accuracy of the fluid integration is improved considerbly as the resolution of ${}_c\overset{*}{B}_{\theta j}$ is improved. This calculation however always introduces a nonlocal constraint into the model.

For the plane parallel waveguide, one may derive either electric or magnetic diffusion relationships from the Hertz potential wave equation in the limit of detailed balance between incoming and outgoing waves. This limit is also equivalent to the neglect of displacement current relative to conduction current. Because both E and B are solenoidal, the resolution of the "companion" field (E when B is diffused, B when E is diffused) always involves the calculation of the field from its curl. It is this calculation which produces the nonlocal constraints that supplement the local diffusive evolution relationships. Whether one chooses electric or magnetic diffusion, it is easy to see that this nonlocal constraint is always equivalent to a single integral equation.

Turning first to magnetic diffusion, the evolution relation

$$\frac{D}{D\tau}B_\theta = \frac{1}{4\pi\Sigma}\{u^{-1}\partial_u(u\partial_u B_\theta) - \hat{E}\partial_u \ell n\ \Sigma - B_\theta\partial_u\beta_r - \partial_u E_{th} \quad [II.4]$$

is obtained by recovering the curl of Ampere's law from the Hertz potential wave equation, writing $J = \Sigma_{Braginskii}\hat{E}$, and eliminating $\partial_\tau E$. The fields B, β_r, $\hat{E}$, radial coordinate u, time τ, and conductivity Σ are in the dimensionless form of the original formulation. The contribution required from Braginskii's kinetic theory and transport coefficients is the constituitive relation

$$J_z = \Sigma(E_z + \beta_r B_\theta + E_{th}) \equiv \Sigma \hat{E} , \qquad [II.5]$$

where Σ and E_{th} are functions of B_θ and the plasma relaxation time, τ_e. On its face [II.4] is a fully local relationship, but one needs a complete profile $E_z(u)$ given at all times in order to calculate the material derivative on the left. Since B_θ and $\partial\tau B_\theta$ are the only fields available one must use Faraday's law to obtain $E_z(u) = \int_0^u d\Omega(\partial_\tau B_\theta)$, a nonlocal operation. This forces one to solve an integral equation for $D/D_\tau\ B_\theta$, viz. [II.4] is now an integral equation for the spatial profile of the material derivative. The value of $D/D_\tau\ B_\theta$ at $u = u_1$ depends upon the values established on the domain $(o,\ u_1)$ through the field $E_z(u)$. Because [II.4] is in fact equivalent to Ampere's law, however, to solve it as an integral equation is to establish that profile J_z which satisfies the constituitive relation [II.5]. The only difference is that it is $D/D_\tau\ B_\theta$, rather than J_z itself, which is adjusted to obtain agreement. One can equally well view [II.5] therefore as the integral equation being solved in a magnetic diffusion calculation; the two are equivalent, interchangeable problems.

For electric diffusion, on the other hand, the evolution relationship is derived by applying the Laplacian to the Hertz potential wave equation, eliminating the $\partial_\tau^2 \nabla^2 Z$ contribution, and introducing [II.5] as the constituitive relation. The evolution relation obtained,

$$\frac{D}{D\tau} E_z = \frac{1}{4\pi_\Sigma} (u^{-1} \partial u\ u \partial_u E_z) - \hat{E} \partial_\tau \ell n\ \Sigma - \partial_\tau E_{th} - B_\theta \partial_\tau \beta_r , \qquad [II.6]$$

is equivalent to [II.4] in all respects. The nonlocal constraint however now enters directly in the form [II.5] because the additional needed profile is now B_θ which must be evaluated from its curl, $4\pi J$, so one must solve [II.5] as an integral equation in order to estabish the profile DE_z/D_τ.

Having established [II.5] as the needed integral equation for either form of the field diffusion theory, it is natural to ask whether or not a particular constituitive relation, in this case Braginskii's, poses a soluble problem in the practical context of a known discrete mesh, and given discrete images of the input fields. If an accurate, unique, and continuous solution cannot be established on a given mesh then the constituitive relation is possibly in error - for what [II.5] establishes is that a B_θ field and its curl, J, are related in a particular way. A result well-known from first principles is that these fields are related uniquely whatever the particular details imposed by the medium; any ambiguity in the solution raises the choice between giving up on a Lagrangian formulation or questioning the accuracy of the constituitive relation.

Using Braginskii's notation (cf. Reference 2, p. 268 (Eq. 6.18-6.20) and p. 249 (Eq. 4.32 and 4.35)) and casting the remaining discussion in CGS units, the axial components of the "Ohm's law" comprising [II.5] can be written

$$J_z = \sigma_B \hat{E}_z$$

$$\hat{E}_z = E_z + \beta_r B_\theta + E_{th} \qquad [II.7]$$

$$E_{th,z} = - \frac{1}{en_e} R_{T,z}$$

with the further reduction

$$E_{th,z} = \left(\frac{1}{e}\nabla_r T_e\right) \times \frac{\beta_0'' + \beta_1'' x^2}{\delta_0 + \delta_1 x^2 + x^4}$$

[II.8]

$$x \equiv -\,(1.7588.10^7\ \tau_e)\ B_\theta$$

obtained when all the substitutions are carried out. The coefficients β_0'', β_1'', δ_0, δ_1 are functions of the ionization state only. When E_z, J_z and B_θ are all negative (the usual convention in ZDIPR) or all positive, and β_r is negative, the domains of positive ${}_rT_e$ weaken the net field by opposing the applied E_z. The domains of negative ${}_rT_e$, in contrast, strengthen the net field because E_{th} is parallel to E_z. In this way the E_{th} tends to oppose, through the J_z component it induces, changes in the flow β_r arising from the temperature gradient.

Using these results the basic constraint relation [II.5] becomes

$$J_z = \sigma_\perp(T_e, n_e, B_\theta)\left(E_z + \beta_r B_\theta + (\frac{1}{e}\ {}_rT_e\right) \times \frac{\beta_0'' + \beta_1''\ x^2}{\delta_0 + \delta_1\ x^2 + x^4} \quad [II.9]$$

with $B_\theta = 2/cr \int_0^r (2\pi r_1 J_z)\ dr_1$, and $x = -(1.7588 \cdot 10^7\ \tau_e)\ B_\theta$, making manifest its characterization as a nonlinear integral equation.

C. APPLICATION OF THE CONSTRAINT RELATION

The nonlocal constraint requires in many cases some new modifications to the field diffusion due to large and quite possibly unphysical thermoelectric fluxes.

In a spatially inhomogeneous magnetoplasma the process of radial implosion forced by axial currents produces radial temperature gradients. These gradients feedback either positively or negatively on the originating axial current (J_z) by means of thermoelectric momentum fluxes arising in the magnetized portions of the annular load. All such thermoelectric momentum transfers originate in differing mean rates of electron (r-z) gyration (in the local magnetic field) on the "up hill" and "down hill" sides of any phase space point. As noted above, the explicit calculation of these imbalanced mean fluxes constitutes a major contribution of plasma kinetic theory to the expected response of the fluid $J_z(E_z,B_\theta,\beta_r,T_e)$ in applied electromagnetic fields.

The constraint [II.9] discussed above can be viewed as a check or any constituitive relation proposed from kinetic theory (or another source). If one fails to find a continuous and single-valued solution, then the proposed response $J_z(E_z,B_\theta,\beta_r,T_e)$ is suspect or non-integrable. In the course of testing the present 1D implosion code (ZDIPR) the integral equation for J_z implied by Braginskii theory was examined in this light and found to cause integrating failures when large temperature gradients were encountered and when thermoelectric fields began to add to the applied E_z. These are unfortunately conditions which are quite common in the implosion solutions examined to date, and it was thus necessary to find a remedy if any progress was to be made in the physical understanding of the current penetration process. The failure in integrating Braginskii's theory manifests itself in a multivalued solution of the $J_z(r,t)$ problem when given a set of profiles ($\sigma(r,t)$, $\beta_r(r,t)$, $T_e(r,t)$ and $E_z(r,t)$).

This must be rejected immediately as a violation of uniqueness and a closer examination shows that continuity in the solution is failing as well. The net result is that for a given non-uniform fluid mesh there always exists an upper limit to the value of $|\partial_r T_e|$ that can be admitted in calculating the thermoelectric fields, E_{th}, by any implicit scheme over the spatial mesh. Somewhat less obvious is the result that this upper limit depends on the radial flow β_r— Braginskii's kinetic theory treatment completely decouples β_r and E_{th}.

It is also easy to verify that the usual validity conditions on Braginskii's theory are not violated when this kind of failure arises. For example, in one ZDIPR calculation the thermoelectric field was limited to $-0.03 \cdot E_{th}$, Braginskii's on a weakly magnetized ($\omega_e \tau_e -10^{-6}$) interior domain of the mesh in order to avoid multivalued roots for J_z. On this same domain, the Coulomb logarithm $\Lambda=9.87$; the thermal gradient scale length $L=0.2194$ (cm) is large compared to the mean free path $\ell=4.795 \times 10^{-3}$ (cm); and the time scale for temperature change $\tau=3.356$ (ns) is large compared to the electron relaxation time $\tau_e=4.221 \cdot 10^{-3}$ (ns). On another, highly magnetized, exterior domain, the thermoelectric field was limited to $-0.0023\ E_{th' Braginskii}$ in the presence of a less stiff temperature gradient $L\ =0.3518$ (cm), and a very small gyroradius $r_e\sim .84 \cdot 10^{-4}$ (cm). In short it would not be possible to anticipate this failure on the basis of the constraints on validity given by Braginskii. Even though similar kinds of limits to ∇T_e apply in thermal conduction, the problem here cannot be formulated with reference to only one process, such as the formation of a heat flux in the presence of a given magnetic field. Here the difficulty is not local, but global, and arises only when the fluid and field models are coupled.

This limit on the practical integrability (to some reliable accuracy) of Braginskii's theory is a serious obstacle to its inclusion in the implosion model. If one accepts the theory as valid and resorts to an explicit integrator, then the accuracy will suffer and color the results in a very subtle way. If one modifies the Braginskii picture explicitly to prevent the problem and to allow the more accurate implicit integrator then the physical content of the model may be hurt but the extent and degree of the inaccuracy is known. The source of the difficulty is the very positive nonlinear feedback of the thermoelectric field on itself, and it is worth asking if this should be so.

If the nonlinear Braginskii picture of the thermoelectric effect is in error as the temperature gradient increases relative to β_r, the correct expression for E_{th} must contain the same symmetries, however it is derived. Since the primary source of this effect is the thermal gradient, one solution is to limit the momentum flux produced by this gradient while not altering the gradient per se, in common with similar treatments for heat conduction. Because the magnetic field serves only to redirect the thermally generated momentum flux and to limit the phase space volume contributing to the mean flux (sought as a source for E_{th}), a plausible model would be to replace

$$E_{th} = \left(\frac{1}{e}\,\partial_r T_e\right)\,\beta_{\wedge}(x)$$

with

$$E_{th} = F(\frac{1}{e}\, \partial_r T_e)\ \beta_\wedge(x),$$

where F is an odd, saturating function of $1/e\ \partial_r T_e$ (the basic measure of source strength) and $x=\omega_e \tau_e$. In general F must couple to the flow field β_r and to the external field E_z. The product of separately odd functions, $F(1/e\nabla T_e)$ and $\beta_\wedge(x)$, is preserved by the cross product nature of the transport.

The general expectation one has for F is that it should be linear for small values of the argument, and bounded above for those situations where $1/e\ \partial_r T_e \rightarrow \infty$. The value $F(\lambda)$ that constitutes this upper bound can be set from the requirement that no multivalued roots occur in the local response curve: $J_z = \sigma(E_z + \beta_r B_\theta + E_{th})$. In general one would expect modifications in $\beta_\wedge(x)$ also, but the qualitative form should be the same. At least the $\beta_\wedge(x)$ dependence calculated by Braginskii provides a reasonably straightforward method for limiting $F(\lambda)$.

A complete and necessarily elaborate investigation of this limiting effect is certainly needed, but it is a very large effort. In order to achieve the new required couplings (to the mean flow β_r and the imposed E_z) one must keep more terms in the collision integral, retain some nonlinear features, and probably include density gradients as well. Such a calculation is most fruitful on a large scale, obtaining corrections to all the transport processes. The choice here, to limit the effective magnitude of $\partial_r T_e$, is ad hoc but physically and numerically reasonable in the face of such gross violations of the electrodynamic constraints discussed above. Moreover, this limit can be incorporated smoothly into the other thermoelectric terms, viz. the thermoelectric heat flux and the $\partial_\tau E_{th}$ required in the electric diffusion equation, and it can be extended easily to 2D models.

The solution of the integral Equation [II.9] proceeds from the mesh interior outward, seeking to establish, from the current densities already known, a local current density, ζ, as the next additional element in the solution vector.

The limit is derived by constraining the

$$\sup_{\zeta} \frac{dJ_z}{d\zeta}(E_z, B_\theta, \beta_r, T_e) < 1,$$

where ζ is the added local current density at any spatial point, and $J_z(E_z, B_\theta, \beta_r, T_e)$ is the response curve given by the transport theory. The saturated amplitude for $F(1/e\nabla T_e)$ is replaced by $(\lambda/e)\ \partial_r T_e$ *and* a value for λ is calculated from the constraint on J_z'. If this λ value is in [0,1] then the thermal gradient $\partial_r T_e$ is limited to $\lambda\ \partial_r T_e$ in that spatial domain for all thermoelectric effects. Limits on the collisional thermal flux are treated separately in a similar manner, and employ a different limit.

Once implemented, one finds that this limit arises under conditions quite easy to interpret physically: (1) the $(ExB)_r$ drift speed (from $E_{th,z} x B_\theta$) in the given thermal gradient must tend to exceed the radial flow β_r; or (2) the thermoelectric E x B drift speed must exceed the local diffusion speed of B_θ; and finally, (3) the thermoelectric field must produce a positive feedback on the current in the plasma. This is very much the situation upon closure of the fluid annulus for example. Particularly interesting among these criteria for the flux limit λ is the involvement of the new E x B drift speed. It is therefore at least a plausible conjecture that Braginskii's theory produces this extreme and perhaps incorrect nonlinearity because the E_{th}xB drift is not properly included in the orbit integrals of the Landau collision term—this collision term in fact neglects all external fields.

These modifications to E_{th} have a significant impact on the physical predictions of the ZDIPR model as well as the numerical techniques required for either electric or magnetic diffusion. The most significant physical result is the level of enhanced current predicted on axis when the annulus closes at high velocity. Under these conditions the (perhaps small) initial value of B_θ in the plasma interior is amplified by the thermoelectric effect because the temperature gradient is negative and, since E_z and E_{th} are therefore parallel, a positive feedback on J_z is generatd by E_{th}. This produces no more J • E heating because the thermoelectric heat flux will tend to cool the axis, but it does tend to increase B_θ near the axis and accrete incoming plasma on a radially growing central filament because the resulting $J_z B_\theta$ stress rises to overcome the outward pressure gradient force, which might ordinarily slow or reflect the incoming plasma. Of course very large currents on axis tend to magnetically insulate those imploding regions just outside and soften the effect. In ZDIPR test runs with the modified E_{th} the axial current peak was still quite high but the cells outside the minimum in T_e did not tend to insulate as much as before the effective temperature gradient was limited. This produced a more persistent, narrower, and stable peak feature in the current density profile and number density profile, indicating a (quite reasonable) coupled compression of particle density and current density. The thermal current source simply tries to preserve the ratio B_θ/n as the plasma stagnates, a result familiar from magnetic diffusion theory in the limit of high conductivity quite appropriate to the hot axial plasma. Alternately viewed, the source term $\propto -B\ {}_r\beta_r$ in DB_θ/Dt, tends to dominate the hot, stagnating plasma and requires current density to rise inside any given radius in order to increase the B_θ value at that radius. In an electric diffusion solution this is done only by generating a strong enough electric field to support the needed J_z, and the thermoelectric field (properly limited as shown above) is the source of this current until the corresponding sources in the electric diffusion equation, viz. $-\partial_\tau E_{th}$ and $-B\partial_\tau\beta$ can build up the "external" field sufficiently to do the job. Such high axial current densities are likely to produce anode damage in small areas corresponding to the spatial extent of the central current filament. Their evolution is therfore a high priority in future work.

A second physical result occurs at the exterior edge of the annulus where the thermoelectric field tends to cancel, rather than to enhance, the applied E. Here the limit on $\partial_r T_e$ is invoked during compression of the outer layers with λ [0.800 → 0.900]. This is a consequence of the required odd parity of F $(1/e\ \partial_r T_e)$ discussed above, because there is really no danger of multiple roots when $\partial_r T_e > 0$ and $\beta_r < 0$. The limit here forces the plasma model to be less effective in shielding out the applied E_z and can be expected to alter the all-important field penetration process when integrated over the run-in phase of a typical implosion.

AD-A154 375 PLASMA RADIATION SOURCES QUASI-ADIABATIC THEORY AND NUMERICAL MODELING IN..(U) JAYCOR ALEXANDRIA VA J U GUILLORY ET AL. 16 JUL 84 JAYCOR-J800-83-003 2/2

UNCLASSIFIED DNA-6304F DNA001-79-C-0189 F/G 20/9 NL

END

FILMED

DTIC

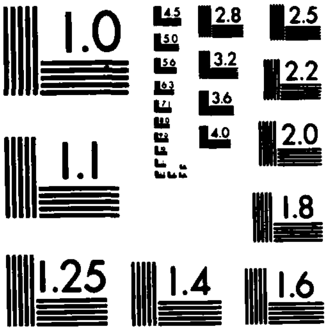
1.0
4.5
5.0
5.6
6.3
2.8
3.2
3.6
4.0
2.5
2.2
2.0
1.1
1.8
1.25
1.4
1.6

MICROCOPY RESOLUTION TEST CHART
NATIONAL BUREAU OF STANDARDS-1963-A

D. PROCESSING SEQUENCE FOR THE MATERIAL DERIVATIVES: FLUIDOTS/TETDOTS

When one combines the foregoing results with the requirements stemming from the basic algebraic structure of the derivatives, there remains very little latitude in the processing sequence required. The first task is to establish the new mesh $\{{}^{*}r_j, {}^{*}V_{rj}\}$ and the second, the appropriate magnetic field ${}^{*}_{c}B_{\theta j}$. These problems are both implicit requiring the solution of a nonlinear system of equations arising from the integration filters selected for space and time. These problems are also both coupled, because ${}^{*}_{c}B_{\theta j}$ depends on ${}^{*}_{c}J_{zj}(E_z, \beta_r, \nabla T_e)$ and the mesh itself. As the only area of choice in the processing sequence, one has therefore the option of nesting the iterations for ${}^{*}V_{rj}$ and ${}^{*}_{c}B_{\theta j}$ in one of two ways: velocity loop inside magnetic field loop, or velocity loop outside magnetic field loop.

Since the velocity loop is the most critical the present implementation puts it outermost, the latter option. This has several advantages for a subcycled architecture. First, the most recent solution of the mesh problem $\{{}^{*}V_{rj}\}$ at a previous call becomes a good seed guess for the new source configuration as well, since it combines all the information about the system. In contrast, because the mesh is very sensitive to the local JxB stresses, the new velocity solution can be far the previous one in the case of arbitrary ${}_{c}J_{zj}$ which arises when the velocity loop is inside the magnetic field loop. Second the Jacobian of the mesh problem is more nearly band-diagonal if the magnetic field is assumed given. In contrast, the Jacobian for the magnetic problem is lower-Hessenberg for a given velocity field. Third, the iteration of the mesh problem for fixed {${}^*_cT_{Ij}$, ${}^*_c\theta_{ej}$, ${}^*_cE_{zj}$} requires a fresh set of densities ${}^*_cn_{Ij}$, intermediate velocities ${}^*_c\beta_j$, thermal gradients, ionization states ${}^*_c\partial_j$, and all active transport coefficients at each evaluation of the acceleration. In contrast, the iteration of the magnetic problem requires fewer fresh transport coefficients, constant densities and thermal gradients, and no equation of state updates. Fourth, the mesh problem has more latitude in the boundary conditions - momentum flux being legislated only if the Lagrangian zone intercepts some fixed wall or the origin in radius. In contrast, the magnetic field problem has a firm boundary condition at the origin which determines the preferential direction of search as the integral equation is resolved.

In view of the considerations just set forth, the computational advantages of putting the velocity loop outermost are:

(1) fewer total iterations, because the mesh problem can be solved by "corrector only" methods and the magnetic problem resolves quickly for a wide range of "seed" fields ${}_cJ_{zj}$,

(2) more accurate applicable matrix-based methods for ${}^*V_{rj}$ because the banded Jacobians can be factored more accurately,

(3) fewer total calculations, because the intermediate fields needed are fewer for the magnetic loop, and

(4) more efficient root searching because of the preferred direction of solution in the innermost loop.

These advantages translate into a fully self-consistent solution of the velocity and magnetic problems in an average of 5 outer and 6 inner iterations for a total of 30 evaluations of the derivatives $D^{*}V_{rj}/D\tau$ and ${}^{*}_{c}J_{zj}$, respectively. The magnitude of relative error in the velocity corrector solution is usually bounded above by 10^{-8}, over all cells, while that in the magnetic field corrector solution is bounded above by 10^{-15}, nearly full machine precision. The errors in the solution of these nonlinear difference equations can be driven to underflow if desired, of course, but the experience to date is that this level of convergence is adequate until the hydrodynamic timesteps can be lengthened.

Once the mesh and magnetic field problems are resolved to a preselected error bound, the remaining tasks are readily performed in the order dictated by the fluid equations. Working from the highest velocity moment downward, and from the interior to exterior in position domains, the first calculation is that for thermal sources and sinks ($\nabla \cdot V_r$, $J_z \cdot E'_z$. Q_{photo}). This is followed by the calculation of dissipative transfers using the flux-limited forms of the thermoelectric and conduction processes recently developed. From the foregoing, the material derivatives ${}^{*}_{c}\dot{T}_{Ij}$ and ${}^{*}_{c}\dot{\theta}_{ej}$ can be formed. The next calculation is an evaluation (if needed) of $D/D\tau \; {}^{*}V_{rj}$ from the mesh configuration and appropriate sources; usually it is sufficient to accept the last value evaluated in the root search for the ${}^{*}V_{rj}$ solution. Finally, the calculation of $D_{c*}E_{zj}/D\tau$ is done, using the acceleration field as a source term and coupling self-consistently to the external circuit relation with a relative error of 10^{-16}. The final output is a very accurate picture of these material derivatives.

E. THE SPATIAL STRUCTURE OF CHANGE

As an example of the kind of processes one must resolve within the plasma load, Figures II.2, II.3, and II.4 have been extracted from the early phases of an implosion calculation. All three are depicted on the same spatial scale a 2.48 ns after the start of test calculation. While the initial configuration was a strictly isothermal (25 eV) Gaussian density and isoelectric ($E_z \sim 3$ StV/cm) profile expanding about r=0.55 at a low velocity ($|\beta_r| \leq 5.0\mathrm{x}10^{-6}$), the later fluid state intercepted these graphs depicts a velocity field (β_r - Figure II.1) negative over most of the domains and a strongly skewed E_z profile; with the outer plasma field of 44.0 StV/cm on order of magnitude than originally given. Owing to the electromagnetic stresses, a very slight crushing is distorting the outer domains of the original Gaussian, while the interior domains begin to execute a rarefaction fan in ignorance of the piston. The exterior velocities have come down considerably and the electron temperature on the surface is beginning to rise.

From this basic configuration $\{n_I, \beta_r, E_z, T_e$ and $T_I\}$,[2] Figure II.2 is completed with the self consistent current density profile as resolved from the integral equation discussed at length above. This structure is essentially barren of any thermoelectric effects and shows the early formation of a peak in J_z, drawn in the domain where E_z decays, due to magnetic insulation effects. The peak value is typical of the current density one might expect in a stationary plasma for these conditions and is contrasted clearly with

---

[2] $T_I(r)$ is not shown in Figure II.2, being essentially indistinguishable from $T_e(r)$.

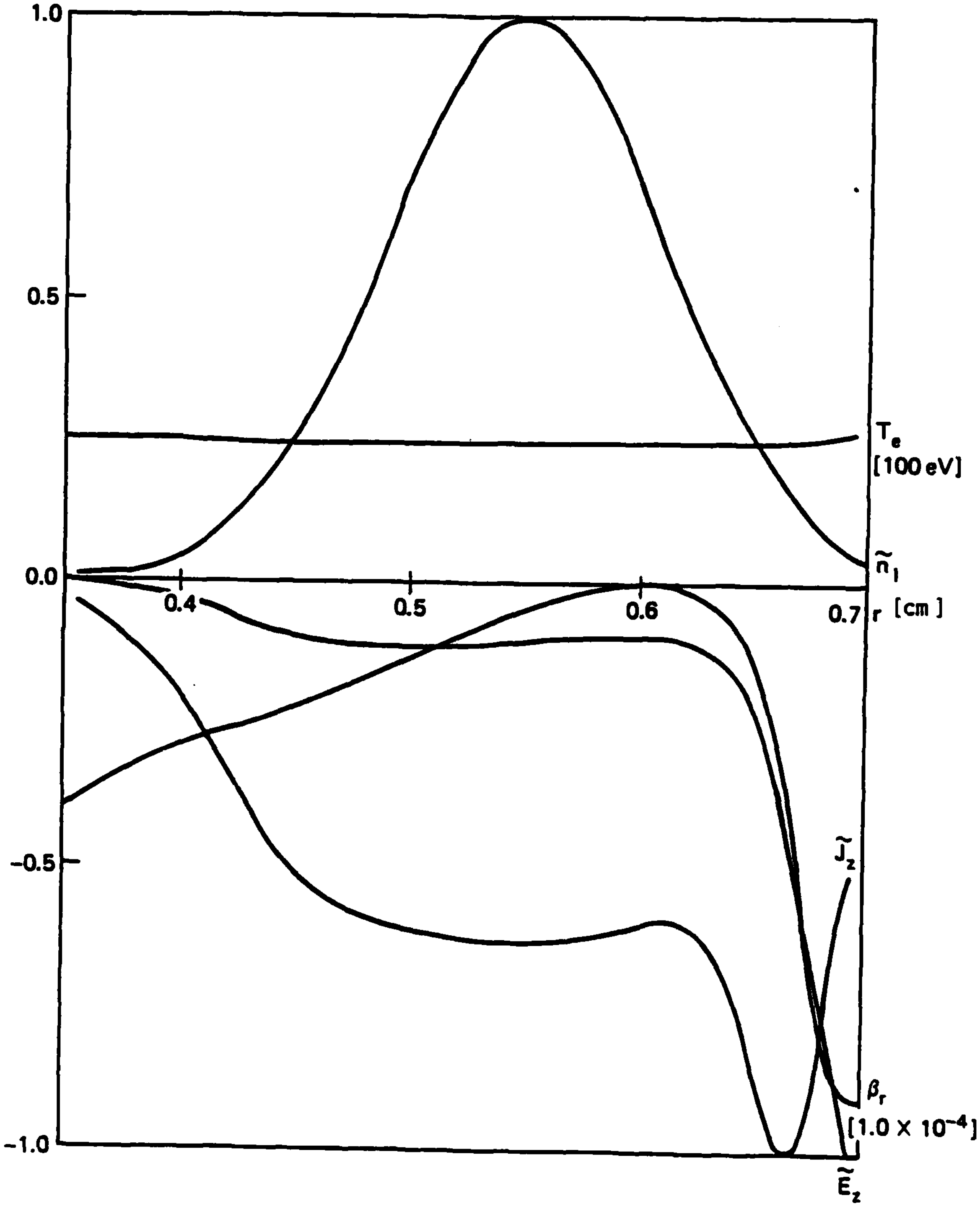

Figure II.2. Plasma profiles at 2.48 ns.

that current actually drawn as one finds more magnetic insulation in the exterior. Note also in this context coincidence of the peak in J_z with the sharp negative excursion in β_r at r~0.67 cm. The relative magnitude of current densities interior to the main peak, and the more gentle downturn in magnitude over the interval [0.49, 0.61] in r, reflects the same magnetic insulation process obtained for a gentler velocity field gradient in a smaller interior $|E_z|$.

The next graph [Figure II.3] shows the spatial structure of the important source terms in the electron temperature equation. The radiative loss profile Q_{rad}, being dominated by thin recombination continiuum and Bremmstrahlung and hence reflecting the density, is broad in space. It also proclaims its thin character by exhibiting a mild kink where the density compression is beginning. In contrast, the ohmic heating profile $Q_{J \cdot E}$ is clearly peaked at the innermost "insulation front" pointed out above; while, at the exterior, the corresponding insulation front peak has blended with the general upturn in ohmic heating associated with the high E_z, low density region, the so-called corona plasma. At this point, therefore, the electromechanical shock has just begun to emerge from the "vacuum" and to accelerate the load. The structure of the shock heating profile Q_{pdV} clearly exhibits this, underwriting as it were, the wider structure in the ohmic heating curve. The acceleration profile $|DV_r/Dt|$ completes the graph and shows a minimum coincident with the slowest portion of the load. At this minimum the contest between incoming E_z with its attendant $J_z B_\theta$ stress) and the pressure gradient is played out; while inside it, the rarefaction fan dominates the motion.

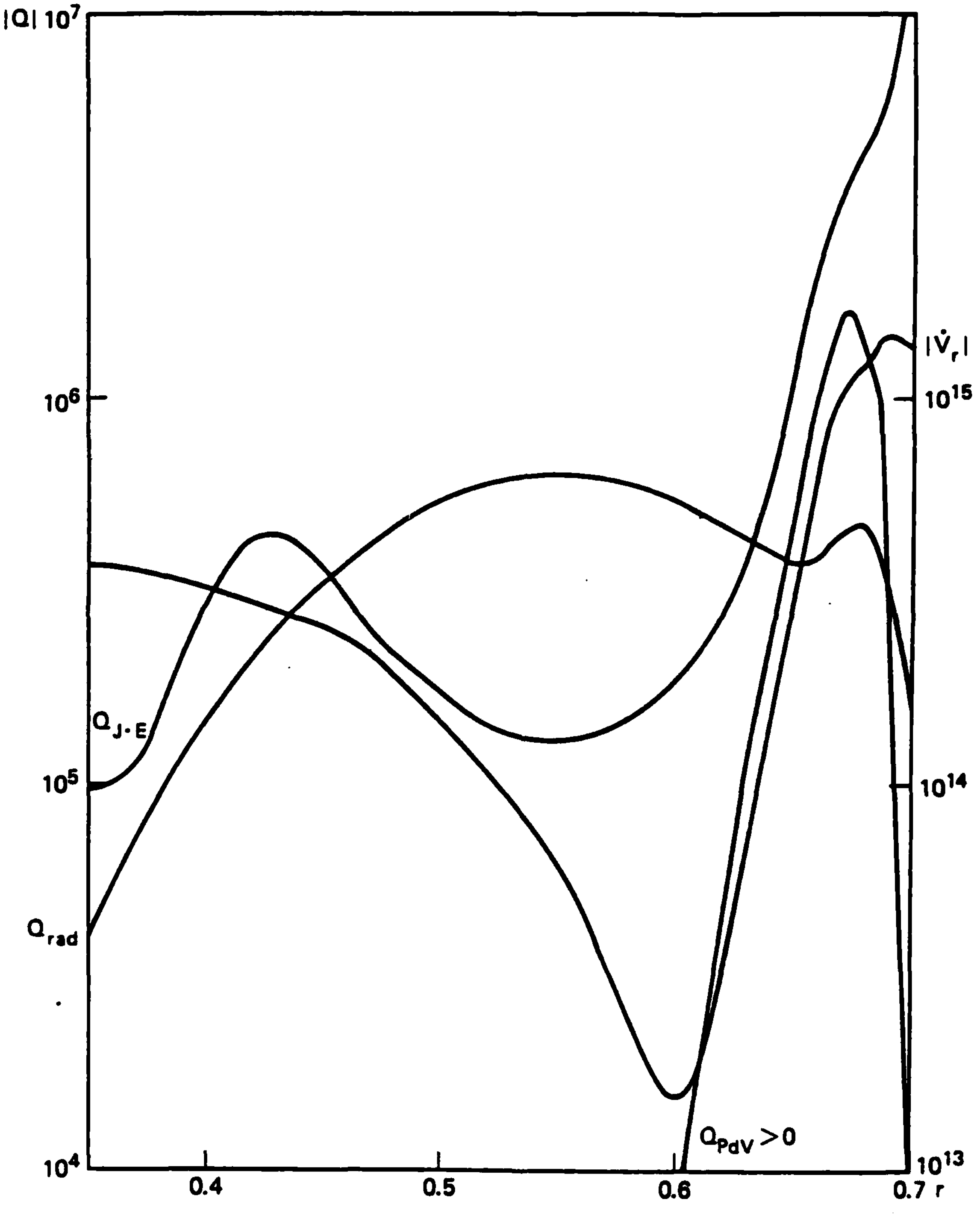

Figure II.3. Plasma source and acceleration profiles at 2.48 ns.

When all these effects are included with the other dissipative processes of thermal and electric diffusion the plasma response contained is that of Figure II.4. The remaining material derivatives are shown and one can see readily the various regions of change and the primary sources in each. Outside the slowest velocity ($r>0.6$), the ion and electron temperatures are being driven apart by ohmic heating, but both are rising due to compression and ohmic effects. In the dense interior, radiation and expansion are cooling the fluid, making field diffusion marginally faster; but in the underdense interior a slight preponderance of ohmic heating arising from the weak initial field begins to warm the plasma. The material derivative of E_z, on the other hand, shows the processes of field penetration. Just inside the peak in J_z the primary source of incoming E_z is the term — ($_\tau\beta$)B_θ, which represents an inductive recoil — allowing more E_z to the conductor when the flow field rises to produce more insulation. This recoil effect is superposed with normal diffusion and in fact dominates the peak $\dot{E}_z$ shown at $r \sim 0.65$. On the exterior, where the gradient $_r\beta_r$ and the gross acceleration are somewhat weaker, the diffusive term proper is competitive as is also the cancellation rate term $\hat{E}\cdot\ _\tau \ell n\Sigma$; but at the shock itself the E_z is moving past the moving fluid predominantly because of the accelerations it gives the fluid. As the velocity field is boosted inward, it would appear that the E_z profile will simply follow this acceleration front along and completely penetrate the load.

In the calculation of this structure of change, it is obvious that an accurate resolution of J_z is central to all of the important physics just discussed: the insulation

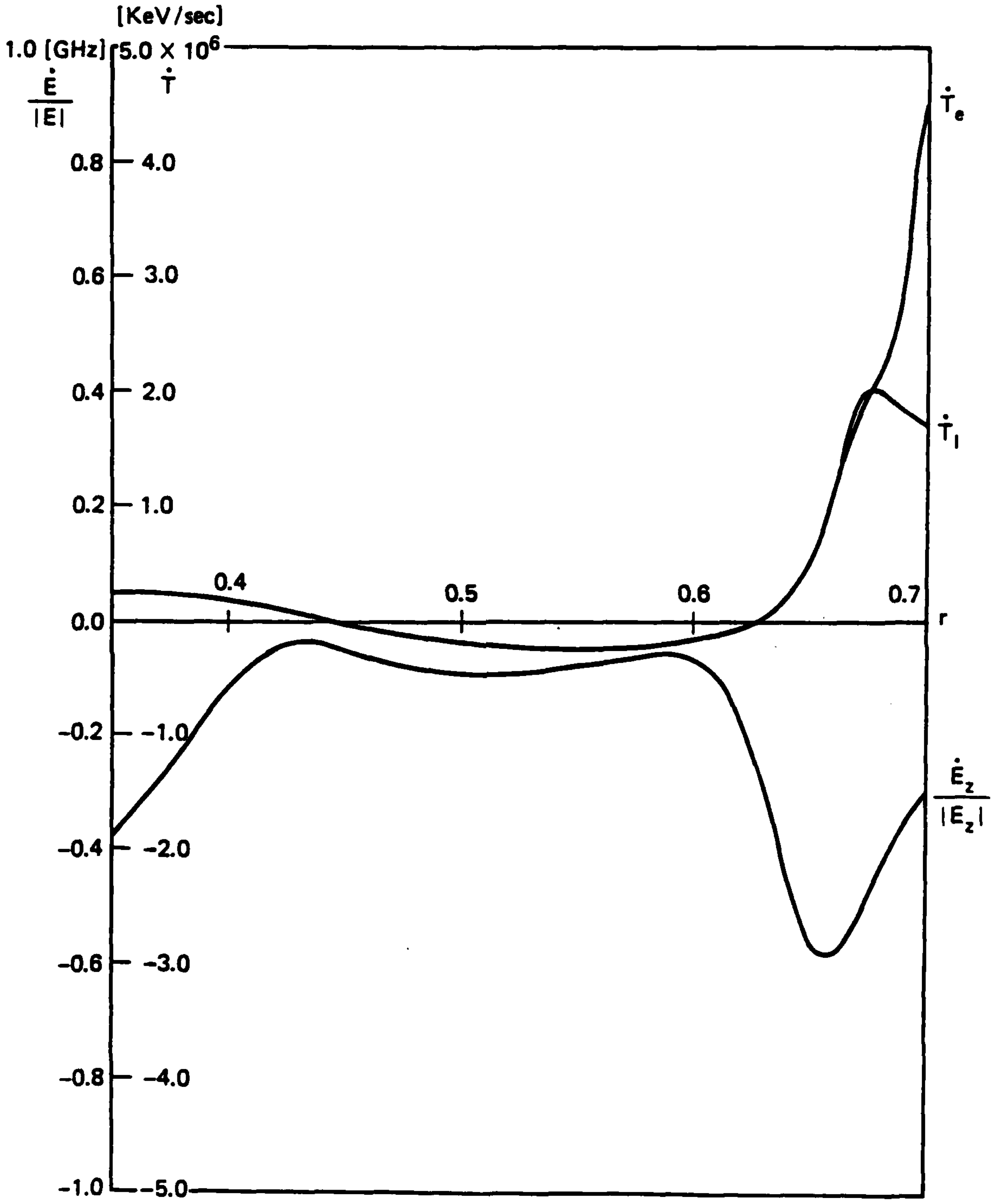

Figure II.4. Material derivative profiles at 2.48 ns.

front, the recoil source for $\dot{E}_z$, and the regions of ohmic heating. It is very important to know the interplay of all the effects discussed above and to incorporate the non-local character of the magnetic insulation process in the field diffusion equation.

CHAPTER III

THE INTEGRATION OF THE FLUID MESH TRAJECTORIES

In the original formulation of this implosion model, correction of the mesh was intended to occur outside the subcycle integration, allowing the explicit calculation of mesh positions inside the subcycle derivative routine itself for any input time argument. However, this scheme allowed too much noise to enter the velocity profile because the feedback from thermal to flow reservoirs tended to come too late. As a means of controlling such noise one is naturally led to a predictor/corrector scheme, of necessity fully implicit. On the other hand, within a subcycle process, the totally arbitrary time coordinate voids the use of customary formulas for the mesh predictor/corrector because the time levels are no longer evenly spaced.

A. CONTINUOUSLY VARIABLE TIMESTEPS AND FILTER THEORY

In order to address the problem of uneven meshes, consider a sequence of time levels $({}^{i-1}t < {}^{i}t < {}^{*}t)$ together with some corresponding velocity and acceleration values $\{{}^{i-1}u, {}^{i}u, {}^{*}u, {}^{i-1}a, {}^{i}a, {}^{*}a\}$. The forward most time, t^*, can be parameterized by a step size ratio

$$\epsilon \equiv ({}^{*}t - {}^{i}t)/({}^{i}t - {}^{i-1}t)$$

relative to the step fixed, defined in the history array, $h \equiv {}^{i}t - {}^{i-1}t$.

If one seeks an integrating filter of the form

$$ {}^{*}u = A_0\,{}^{i}u + A_1\,{}^{i-1}u + h(\epsilon B_{-1}\,{}^{*}a + B_0\,{}^{i}a + B_1\,{}^{i-1}a), \qquad [\mathrm{III.1}]$$

how can the five coefficients be related to the error characteristics and the timestep ratio ε? It is useful to address this topic with a straightforward extension of the transfer function as commonly defined in Fourier or z-transform theory. Let the accelerations be limited to harmonic components $a = {}^{i}A_{In} e^{j\omega}(t - {}^{i}t)$ and seek a particular solution $u = {}^{i}A_{out} e^{j\omega}(t - {}^{i}t)$, the filter is then charcterized uniquely by the ratio

$$\frac{A_{out}}{A_{in}} = \frac{h(z^{\varepsilon} \cdot \varepsilon B_{-1} + B_0 + B_1 Z^{-1})}{z^{\varepsilon} - A_0 - A_1 z^{-1}} \qquad \text{[III.2]}$$

where $Z \equiv e^{j\omega h}$.

For a perfect integrator [III.2] must equal $1/j\omega$ and the selection of coefficients $\{A_0,\ A_1,\ B_{-1},\ B_0,\ B_1\}$ must be a compromise process which produces optimal accuracy and stability as a function of the step ratio ε. Let the phase $\zeta \equiv \omega h$ be an expansion parameter and require that the perfect integrator be approximated through some order in ζ. One must have

$$1 = j\zeta \left\{ \frac{\varepsilon B_{-1}\ z^{\varepsilon} + B_0 + B_1\ z^{-1}}{z^{\varepsilon} - A_0 - A_1\ z^{-1}} \right\} + E(O[\zeta^n]) \qquad \text{[III.3]}$$

where the error term E is bounded by ζ^n, $n \geq 3$ if one wishes a second order or higher integrator. Since $z^{\varepsilon} = e^{i\zeta\varepsilon}$ the sequential orders in ζ arise by expanding the right hand side of III.3 and equating real and imaginary parts. This yields at each order a new element in the set of constraints on the coefficeints in the formula, viz.

$$O[\zeta^0]: \quad 0 = 1 - A_0 - A_1$$

$$O[\zeta^1]: \quad B_0 + B_1 = A_1 + \varepsilon\,(1 - B_{-1})$$

$$O[\zeta^2]: \quad B_0 - B_1 = \varepsilon^2 - 2B_{-1} + \varepsilon(1 - B_{-1})$$

$$O[\zeta^3]: \quad B_{-1} = \frac{(2\varepsilon^4 + 3\varepsilon^3 - \varepsilon A_1)(1 + A_1) - (1 - \varepsilon)A_1^2}{6\varepsilon(\varepsilon + 1)(1 + \varepsilon A_1)}.$$

These expressions already contain some eliminations, e.g., A_0, but as a set they specify all of the formula as a function of A_1. In the case that $\varepsilon=1$ these constraints reduce to a well-known class of formulas due to Hamming. The new extension here is to arrange the theory in such a way as to produce uniform truncation error ($o[\zeta^3]$) in the integrating filter for a continuum of timestep ratios ε.

As in the fixed-step case, the choice of A_1 represents a trade-off between accuracy, stability and noise propagation. The introduction of the ζ^4 constraint could provide a unique function $A_1(\varepsilon)$ but, after some investigation of the quartic equation involved, it appears the real solutions with the property $A_1(0)=0$ may not exist. This property is importrant because it assures precise continuity of the velocity value $^*u$ forward from ^1u, i.e., the filter collapses to an identity transformation as $\varepsilon \rightarrow 0$ when A_1 also vanishes. A second point in favor of avoiding the ζ^4 constraint is that such high accuracy usually pushes one onto the stability boundary. In examining the present fomulas over the entire A_1/ε domain for those cases with $A_1 \sim \pm 1$ and $\varepsilon \sim 1$, the response curve showed a small imaginary part, corresponding to a better approximation to the perfect integrator. These regions are known stability boundaries for the fixed step formulas of Hamming, therefore, such high accuracy can be traded here in order to guarantee stability. A third point in favor of leaving A_1 free is the possible control of noise propagation. A priori it is of interest to produce an integrating filter with a sharp or even tunable low pass response because the local hydro cell sizes determine those frequencies too high to be physical. The choice $A_1(\varepsilon)$ may have some bearing on this question as well. The character of the response curves will be discussed at more length in the next section.

The filters compared in later sections differ in only one respect - the functional dependence $A_1(\varepsilon)$. They are arbitrarily designated Class A and Class B, representing two qualitatively distinct types of integrating filter.

The Class A filter is generated by the rule $A_1 = 0.25\ \varepsilon$ and is characterized on $(0<\varepsilon<1.2)$ by three features:

(1) coefficients of largest magnitude remaining positive for all ε,

(2) εB_{-1} uniformly smaller than B_0 for all ε,

(3) $B_1>0$ over most of the ε domain.

This particular filter does not mix ${}^{*}a$ and ${}^{i}a$ with equal weights until $\varepsilon>1.2$ and has ia predominating by a factor of 2 or more for $\varepsilon<1$.

The Class B filter is generated by a more complicated rule:

$$A_1 = [-0.4 + 0.2\ f(\varepsilon)]\ \varepsilon$$

with $f(\varepsilon)$ a smooth step function $[0<\varepsilon<1.2]$ bounded above by 1 and below by 0. This rule is selected to track, roughly, a peak in the value of εB_{-1} at small ε until the maximum blends into a general rise for ε - 0.45. Thereafter the rule keeps A_1 well above the stability boundary at -1 for

$\varepsilon<1.2$. In comparison this Class B filter is charcterized on $0<\varepsilon<1.2$ by

(1) positive εB_{-1} for all ε,

(2) εB_1 exceeding B_0 for larger $\varepsilon>1.05$,

(3) $B_1<0$ over the domain studied.

Hence the Class B filter tends to use the history as a derivative estimate for the surge ($B_0>0$, $B_1<0$), while the Class A filter tends to average previous accelerations. The following sections are devoted to the comparison of these integration filters and to the implications of these results for the hydrodynamic code.

B. RESPONSE STABILITY AND ACCURACY

If the transfer function is decomposed into real and imaginary parts one obtains a picture of the propagation characteristics of the filter on the frequency domain defining the time dependence of the acceleration, a(t). The more useful object however is the scaled difference of the transfer function from the perfect integrator $1/j\omega$, i.e., $H(\zeta) \equiv j\zeta A_{out}/A_{in}{}^{-1}$. A comparison of $R_e\ H(\zeta)$ and $I_m\ H(\zeta)$ for various values of ε (between the two classes of integrators defined above) is a helpful summary of their differences. The typical frequency response one finds is illustrated in Figures III.(1-2) for the Class A integrator and in Figures III.(3-4) for the Class B integrator. The plots show the real part (R) imaginary part (I) and modulus (M) of $H(\zeta)$ at two values of ε in each case. For $\varepsilon=1.1$ the Class A formula has a slightly broader pass band in the real part but a flatter low frequency response. The Class A formula shows a larger magnitude in the imaginary part for all ζ, but this

CLASS A:

Re H(ξ), Im H(ξ), |H(ξ)| at ε = 1.10

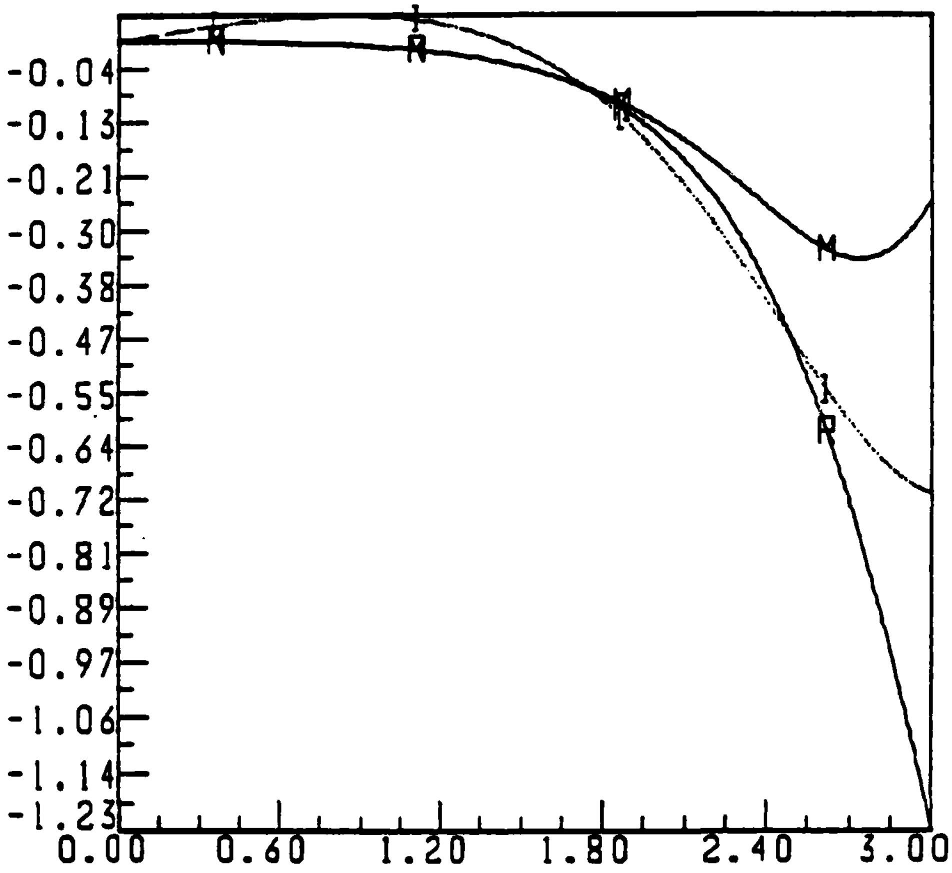

ξ [Phase in Radians]

Figure III.1

CLASS A:

Re H(ξ), Im H(ξ), |H(ξ)| at ε = 0.50

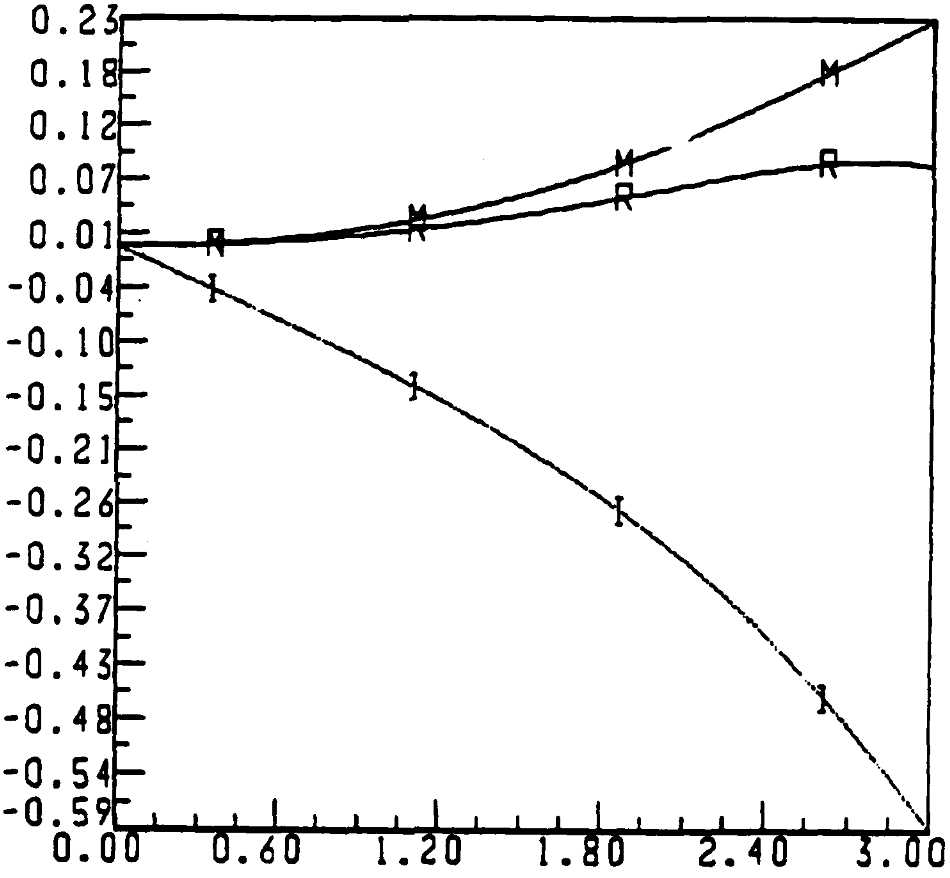

ξ [Phase in Radians]

Figure III.2

CLASS B:

Re H(ξ), Im H(ξ), |H(ξ)| at ε = 1.10

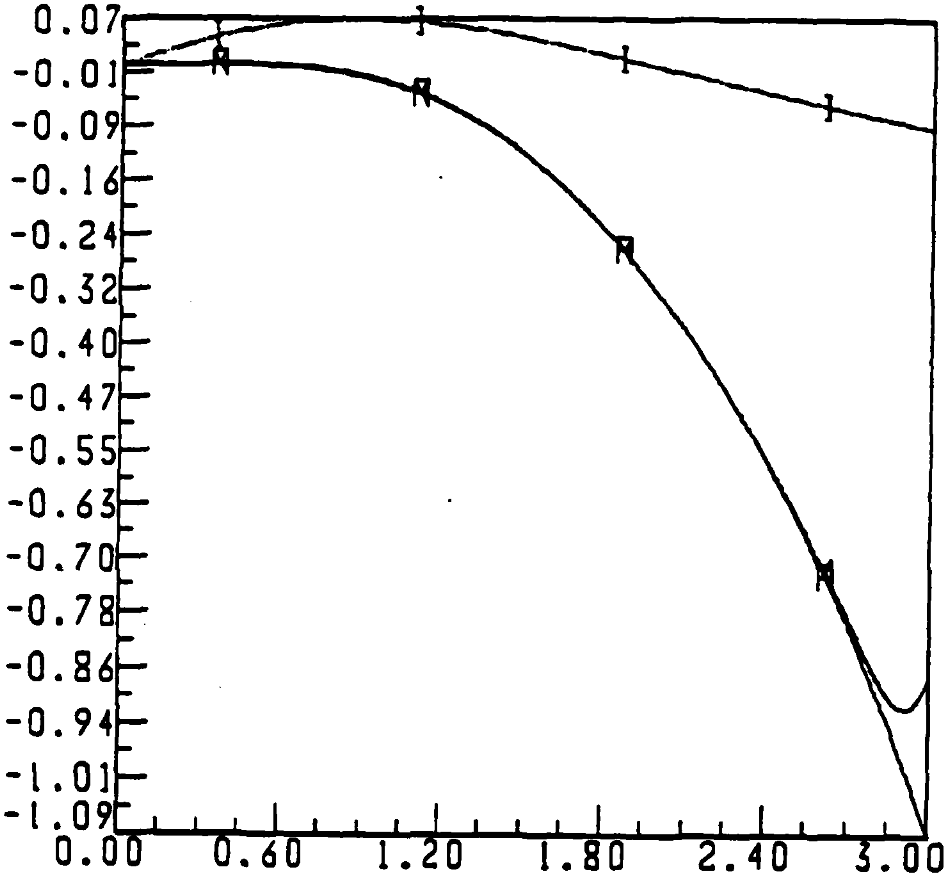

ξ [Phase in Radians]

Figure III.3

CLASS B:

Re H(ξ), Im H(ξ), |H(ξ)| at ε = 0.50

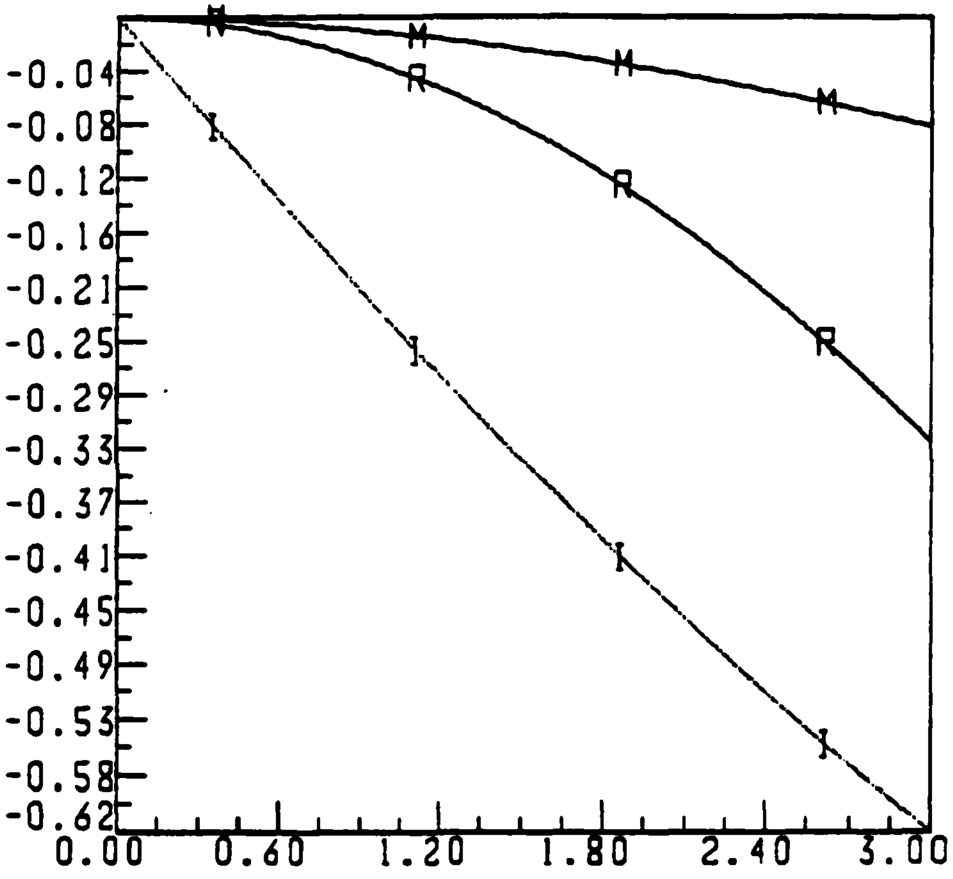

ξ [Phase in Radians]

Figure III.4

imaginary part is negative at high frequencies. For $\epsilon=0.5$ the Class B formula retains its rather slowly decaying low pass character, while the Class A formula exhibits a mild rise in the real part before assuming the usual downturn at higher frequencies. Both integration filters have similar negative imaginary parts. From this comparison (which persists for all ϵ) one might expect the Class A formula to be slightly more susceptible to noise but more accurate and the Class B formula to be more likely to propagate growing parasitic solutions due to the more positive imaginary parts.

A second analytic tool is the relative stability criteria for each of the integrators. This test is somewhat limited in its scope because the root conditions apply only to even meshes and, while solutions for $\epsilon\neq1$ exist, the interpretation is not particularly clear. The first root condition is independent of timestep and involves only A_1 and A_0. It requires essentially that the denominator of the transfer function possess no zeros for $z>1$. For the Class A formula the roots at $\epsilon=1$ are $z=\{1.0, -0.25\}$; for Class B, $z=\{1.0, 0.2\}$. In both cases absolute stability is assured. The second root condition involves the phase also and speaks to the stability of propagated errors, the relative stability of the scheme. Since phase values greater than 0.2 are not likely to be used on a single step $\zeta=0.2$ is taken as the phase in the test. The corresponding roots at $\epsilon=1$ for the Class A formula are $z=\{1.219, -0.2256\}$; while for class B, $z=\{1.221, 0.2091\}$. Again in both cases, relative stability seems assured with Class A perhaps a bit more stable as expected.

It is a well-known result that stable consistent methods are convergent integrators for even timesteps. Certainly one expects this property to generalize smoothly for the continuously variable step methods examined here. The best kind of test is therefore an integration of some known and (preferably) relevant problem. For the integration of imploding trajectories the natural test bed is the Gaussian implosion a self-similar isothermal (in space) fully time dependent hydrodynamic flow. To summarize the fluid density, temperature, Lagrangian position and flow velocity, and acceleration are specified by:

$$n(r,\ t) = \frac{N_0}{\pi r_s^2(t)}\ e^{-r^2/r_s^2(t)},$$

$$T(t) = T_0/u(\tau),$$

$$r(t) = r(0)\ u^{1/2}(\tau)\ (\text{for } r_s(t) \text{ also}), \qquad [\text{III.4}]$$

$$V(t) = V(0)\ u^{-1/2}(\tau)\ (\text{at } r(t)),$$

$$\dot{V}(t) = a(0)\ u^{-3/2}(\tau)\ (\text{at } r(t)),$$

where the generating function

$$u(\tau) = \frac{\gamma_E + [1 + (1 + \gamma_E)\tau]^2}{\gamma_E + 1} \qquad [\text{III.5}]$$

depends on the initial velocity scale and kinetic to thermal energy ratio,

$$\tau = K_i t/2$$

$$\gamma_E = 8\ T_0/m r_0^2 K_i^2$$

$$K_i = V(0) \cdot 2/r_s(0) \qquad [\text{III.6}]$$

$$a(0) = 2\ T_0/m r_s(0).$$

The test consists in selecting K_i, γ_E and, using the filter [III.1] with $\dot{V}(t)$ calculated analytically from [III.4-6], comparing the known velocity to the filter output and the known position to the corresponding second intergal of [III.1], viz.

$$*r = {}^{i}r + \epsilon h(*u + {}^{i}u)/2 \qquad [\mathrm{III}.7]$$

This kind of check tests only the filter, the analytical accelerations remove any errors propagated when the filter is combined with some algorithm for corrector convergence e.g., regula-falsi. A fully implicit scheme for this problem does exist and will be examined later if it is of interest. As a second exercise the acceleration is perturbed by a sinusoidal ripple, $a = a_{flu}(t) + \delta \sin \omega \tau$. This allows a check of the frequency response in terms of complete throughput as opposed to the single-step analysis above.

The timestepping for these checks is controlled by a relative tolerance for single step velocity changes which progressively slows the step as the turning point is reached due to ever-increasing accelerations. For very small tolerances the step usually sinks to a given floor sufficient to limit the number of steps over a full implosion to about 30,000. The relative error in r and V is reported every 0.1 ns — γ_E and K_i being appropriate to 60 ns overall implosion/expansion times. The time supremum (in absolute value) of r and V errors at full step, and 1/3-, 1/2-, 2/3-step test subcycles is also accumulated on every push.

The results are summarized in Tables III.1 and III.2. The Class A formula is decidedly superior on all counts over a wide domain in the implosion phase space (γ_E, K_i). The Class B formula wins only in the suppression of very high

TABLE III.1

Gaussian Implosion Trajectory Integration
at Single-step $\delta V/V = 5.0\cdot10^{-4}$

$\delta x \equiv x_{filter} - x_{analytical}$

(κ_i, γ_E)	Class A		Class B	
	$\sup_t (\frac{\delta r}{r})$	$\sup_t (\frac{\delta V}{V})$ [§]	$\sup_t (\frac{\delta r}{r})$	$\sup_t (\frac{\delta V}{V})$ [§]
(-0.2, 0.1)	$2.10\cdot10^{-5}$	$5.60\cdot10^{-2}$	$3.52\cdot10^{-5}$	$9.90\cdot10^{-2}$
(-0.1, 0.1)	$1.86\cdot10^{-5}$	$6.87\cdot10^{-2}$	$3.10\cdot10^{-5}$	0.121
(-0.1, 0.01)	$1.01\cdot10^{-4}$	0.304	$1.55\cdot10^{-4}$	0.553
(-0.1, 0.001)	$7.59\cdot10^{-4}$	0.558	$1.11\cdot10^{-3}$	1.137

[§] Relative velocity errors are dominated by the behavior near the turning point, elsewhere they are comparable to $(\delta r/r)$.

TABLE III.2

Noisy Gaussian Implosion Trajectory Integration
$[\kappa = -0.2, \gamma_E = 0.1$, Same Tolerance$]$

δ - Noise Amplitude: 0.15

Ripple cycles/ timestep $\delta\Delta t$	Class A $\sup_t (\delta r/r)$	Class B $\sup_t (\delta r/r)$
.0411	$3.155\cdot10^{-4}$	$9.31\cdot10^{-4}$
.2405	$3.39\cdot10^{-4}$	$4.54\cdot10^{-4}$
.8065	$2.28\cdot10^{-3}$ •	$9.92\cdot10^{-4}$ •
4.032	$4.14\cdot10^{-4}$	$5.17\cdot10^{-4}$
8.064	$1.75\cdot10^{-3}$ •	$6.84\cdot10^{-4}$ •
43.20	$2.93\cdot10^{-4}$	$1.24\cdot10^{-3}$ •
86.30	$1.50\cdot10^{-3}$ •	$1.83\cdot10^{-3}$ •

frequency noise above the Nyquist frequency and hence of only minimal interest. The Class A formula exhibits isolated resonances in this domain while the Class B first damps them and then admits a single large one.

CHAPTER IV

SNOWPLOW FORMATION -- THE BOOST PHASE

At the close of Chapter II the spatial structures in the material derivatives of temperature and electric field pointed out some of the fundamental responses of a plasma load to its pulse power environment. Following that same example for a short time the present discussion focuses on the evolution of the snowplow or magnetic piston as a primary feature of the run-in plasma. These thoughts are necessarily preliminary and such results as can be obtained will be followed up in greater detail as the code's operation and efficiency are improved.

One can see the emergence of the snowplow most clearly in the sequence of ion density and electric field profiles shown in Figure IV.1. The configuration at 3.3 ns is scarcely distinguished from the example of Section II.E at 2.48 ns except that the exterior field has now risen to around 50 StV/cm. By 10.8 ns, however a new density peak has emerged and the exterior domains are strongly crushed by the electromagnetic stresses; the E_z field has followed the compression and risen significantly in magnitude. The final state, at 18.8 ns, shows the new density peak inside the original and a signifcant distortion of the E_z profile with an exterior field of 167 StV/cm.

If one characterizes the E_z profile by its half-relative-amplitude point $r_{1/2E}$, then this point is found to move in quickly, successively overtaking comoving fluid zones in response to the impressed sources for E_z. In the early times $r_{1/2E}$ is just inside the budding or emergent new

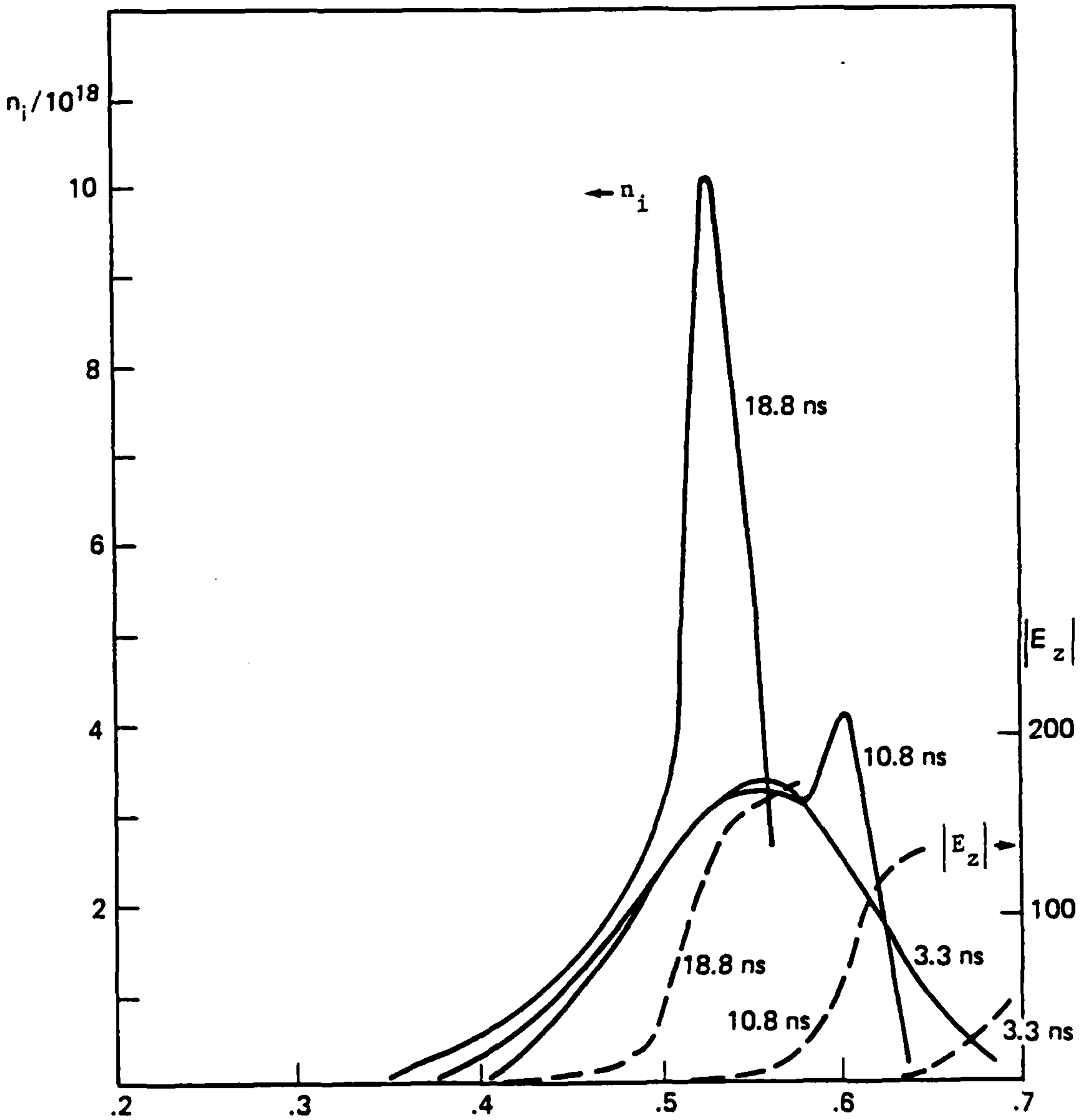

Figure IV.1. Sequential density and field profiles.

density peak $r_{n,peak}$, while in the last configuration it has moved well inside this peak. The slowest-velocity point $r_{\beta max}$, and the half-amplitude velocity point (relative to the outer surface velocity) $r_{1/2\beta}$ are also seen to move in a similar manner, overtaking the calculation zones as part of a general acceleration or "boost" front which is propagating through the plasma.

A more detailed graph of the model plasma at 18.8 ns (Figure IV.2) shows the fully developed snowplow configuration. The current density now peaks more sharply, at a deeper radius and the width of the current carrying layer has doubled over that in the intial state. The progress of the boost front is marked by the slowest velocity point (0.476 cm) as compared to 0.62 cm at 2.48 ns. In step with this are both $r_{1/2E}$ and $r_{1/2\beta}$ at -0.52 cm (in from -0.66 cm at 2.48 ns) and the velocity profile for $r>0.5245$ cm is flattened in conjunction with a quasi-equilibrium configuration of the stresses. The ion and electron temperatures show a peak at the location of the compression maximum which is in turn essentially coincident with the peak acceleration and located just outside the boost front, cf. Figure IV.3. The minimum acceleration magnitude lies inside the minimum velocity magnitude as in the earlier graphs and both lie inside the temperature peak associated with the shock. The radiative loss profile (cf. Figure IV.3) now reflects this in its triple peak: the interior peak in T_e, the density maximum, and the product of decaying density and rising temperature in the near corona. It is still dominated by thin continuum and Bremmstrahlung.

The field penetration process is still dominated by the recoil mechanism $-(\partial_\tau \beta_r)B_\theta$ at the boost front but is given

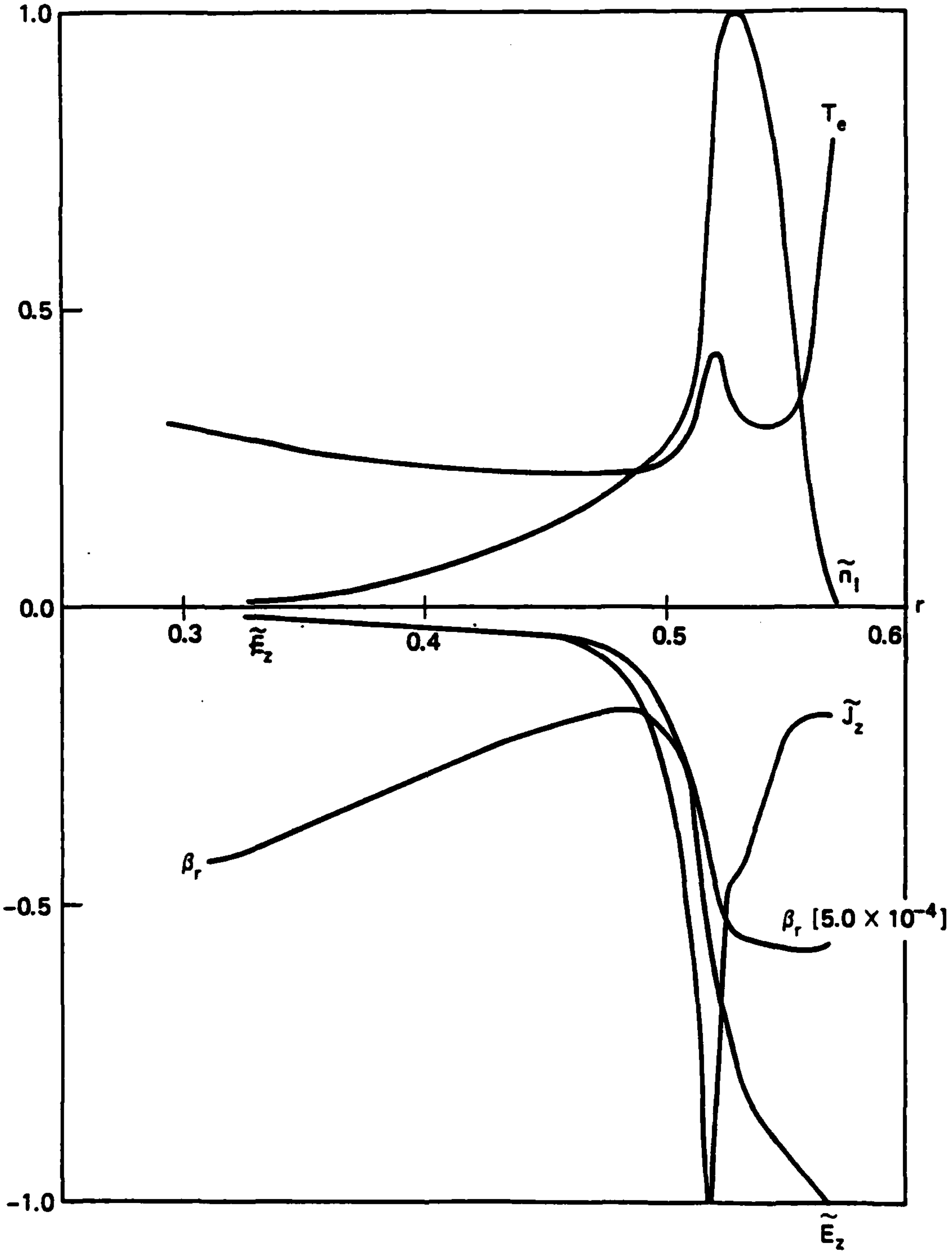

Figure IV.2. Plasma profiles at 18.8 ns.

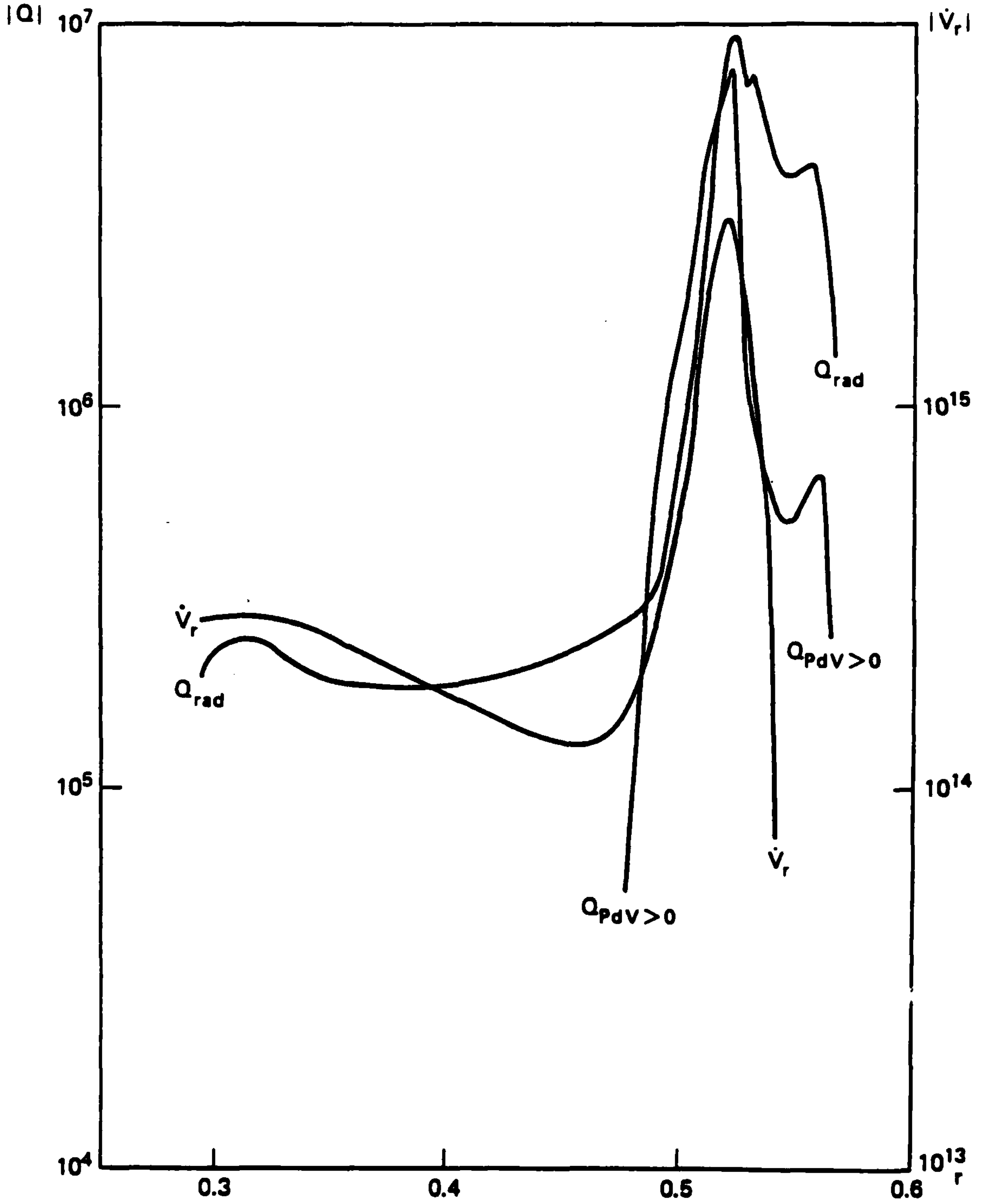

Figure IV.3. Plasma source and acceleration profiles at 18.8 ns.

by a mix of effects inside and outside this point. The configuration of $\tilde{J}$, $\tilde{E}$, and β_r has not changed its character since its formation at early times, cf. Figure II.2. The structure in the vicinity of the field decay radius $r_{1/2E}$ is just moving across the plasma load dragging the E_z field inward at a rate fast compared to that of pure diffusion. Spatially the penetration can be characterized by an invariant ordering of radii with perhaps time dependent relative separation among them. Innermost is the minimum of acceleration magnitude $r_{\max\dot{\beta}}$; next outermost the minimum flow speed $r_{\max\beta}$; followed by the field decay radius $r_{1/2E}$ and completed by the onset of quasi-equilibrium flow r_{QSV}. The $\tilde{J}$ profile and the velocity half amplitude $r_{1/2\beta}$ tend to oscillate around $r_{1/2E}$, so that no one ordering of these radii is appropriate.

The onset of quasi-equilibrium flow at r_{QSV} can be expected to continue into the corona plasma. The linear equilibrium near r_{QSV} arises when $\nabla(nT) \sim \sigma B(E_z + E_{th} + \beta B)$; the saturated equilibrium will onset when $\nabla(nT) - B \cdot$ enecs obtains as E_z grows in the "vacuum" region and βB is held to moderate levels by the cap $|\beta| \leq |\beta_{QS}|$ and the saturation of J_z at larger radius. The complete ordering of radii, apparently invariant during the early run-in or boost phases is then $\{r_{\max\dot{\beta}} < r_{\max\beta} < r_{1/2E} < r_{QSV} < r_{Corona}\}$. The calculation of the equilibrium density profiles falling on this domain may prove a valuable modeling asset both in simple applications and in the smoothing and rezoning of implosion problems. In this connection however it is worth noting that the full nonlinear complexity of the thermoelectric field must be included as can be seen in Figure IV.4. Any such calculation of a quasi-equilibrium $\{n_I, B, J\}$ given

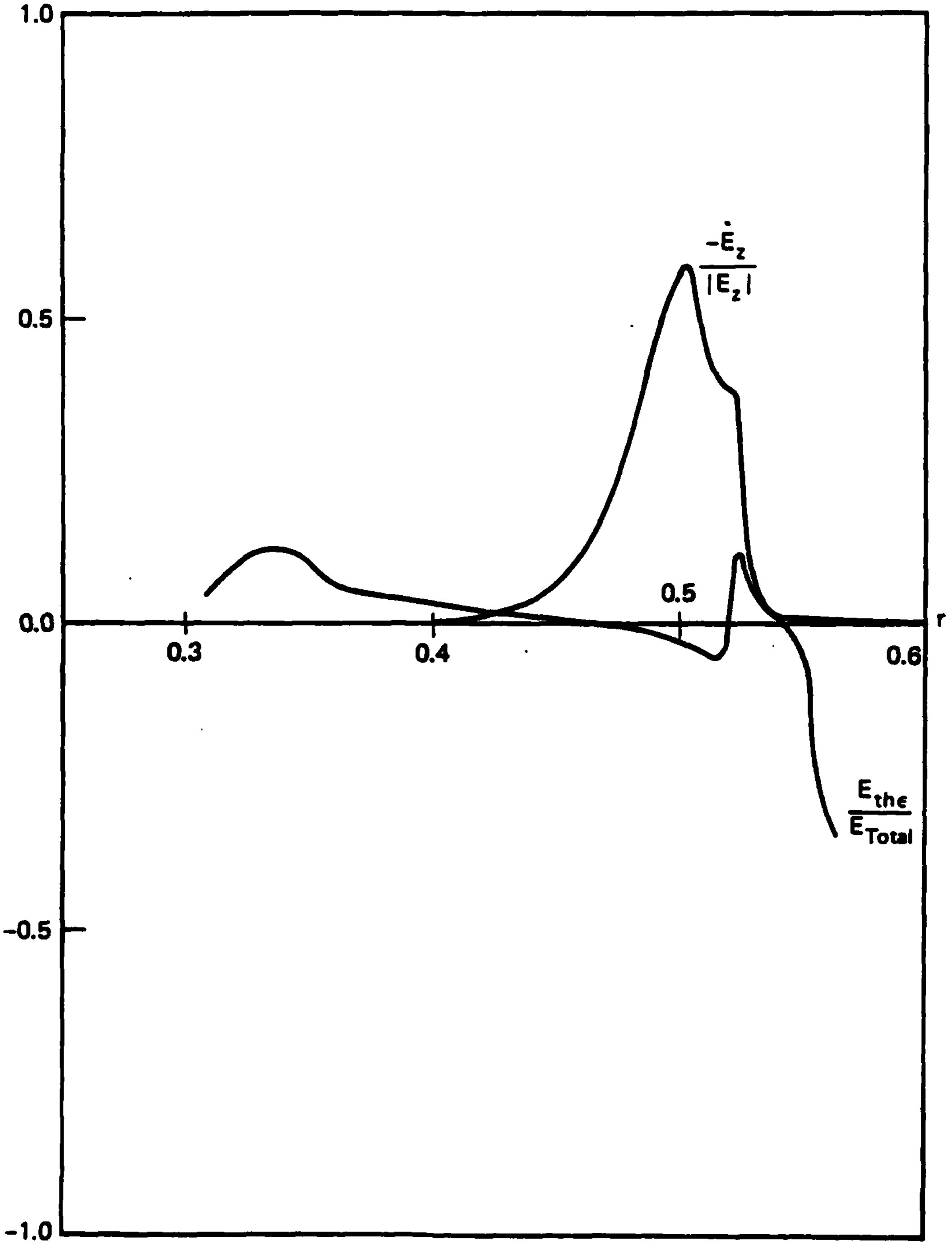

Figure IV.4. Field structure at 18.8 ns.

typical $\{T_e, \beta, E_z\}$ will find E_{th} a 30-50 percent effect as one approaches the corona. Note also the impact of the thermoelectric field on the structure of $\dot{E}$. The main peak in $\dot{E}$ is due to recoil and diffusion; the inward foot is mainly due to recoil; but the outer wing comes from $\partial_\tau E_{th}$ and the magnitude of the effect is beginning to approach the saturated or flux-limited domain (discussed in Section II.C) at the outer radius of this calculation. One may perhaps take some consolation in the fact that the saturated domain of E_{th} does not have a great impact on $\dot{E}$ but the thermoelectric effect is rather important in these plasmas.

The completion of this rapid penetration of E_z into the plasma load has not yet been calculated but the limiting factors will be the disappearance of the sharp gradient in velocity and the weakening of the accelerations generally as the insulation front is allowed deeper into the load. If what occurs here is corroborated by wider numerical exerience then a general picture of the boost phase of a run-in can be formulated. One would expect an early field penetration determined by a contest of rates and the initial density profile — E_z (with J_z peaked at an insulation front) will penetrate the load until the local velocities of the interior are comparable to the outer surface. At this time the penetration will become mainly diffusive — at rate characteristic of the radiatively cooled interior plasma not the hot corona however. When the penetration settles down into diffusion, the width of the effective current carrying layer may be quite large although the stresses may not be reduced proportionately because of the peaked nature of the J profile near the insulation front. The investigation of this process is therefore a high priority for future work.

CHAPTER V

SUMMARY OF PART II

In the foregoing discussion, the structure and performance of the electrodiffusive model of a 1D imploding plasma radiator has been detailed. Some modifications to the original formulation have become necessary in order to achieve a self consistent picture of the fluid motion and more modifications are clearly needed to the integration package in order to obtain a useful performance with respect to DNA objectives.

On the methodological side, a new integrator for the fluid mesh has been developed and applied successfully to known trajectories. Certain discretization difficulties in the Braginskii thermoelectric field model have been identified in the context of E-field diffusion and removed by the development of a simple flux limit on the thermal gradient used as a source of this field.

From the physical standpoint, the novel E-diffusion formulation has shown a sensible performance over short time intervals and resolved some fundamental features of the load acceleration processes in a speculative but plausible initial condition for present DNA sponsored experiments. The novel equation of state involving generalized electron temperature θ_e has been shown a useful formulation as well.

REFERENCES FOR PART II

1. R.E. Terry and J. Guillory, JAYCOR Report J207-82-002.
2. S.I. Braginskii, in Review of Plasma Physics, ed. M.A. Leontovich (Consultants Bureau, New York 1965).

DISTRIBUTION LIST

DEPARTMENT OF DEFENSE

Asst to the Sec of Def, Atomic Energy
ATTN: J. Rubell
ATTN: Executive Assistant

Defense Intelligence Agency
ATTN: DT-18, R. Rubenstein

Defense Nuclear Agency
ATTN: RAAE
ATTN: RAEE
ATTN: STNA
2 cys ATTN: RAEV
4 cys ATTN: STTI/CA

Defense Tech Info Center
12 cys ATTN: DD

Field Command, DNA, Det 1
Lawrence Livermore National Lab
ATTN: FC-1

Field Command, Defense Nuclear Agency
ATTN: FCTT, W. Summa
ATTN: FCTT
ATTN: FCTXE
ATTN: FCPR

Under Secy of Def for Rsch & Engrg
ATTN: Strat & Space Sys (OS)

DEPARTMENT OF THE ARMY

Harry Diamond Laboratories
ATTN: DELHD-NW-RA
ATTN: DELHD-NW-P
ATTN: DELHD-NW-RI, Kervis
ATTN: DELHD-TA-L

US Army Nuclear & Chemical Agency
ATTN: Library

US Army Test & Evaluation Comd
ATTN: DRSTE-CT-C

USA Missile Command
ATTN: Doc Section

DEPARTMENT OF THE NAVY

Naval Rsch Laboratory
ATTN: Code 4720, J. Davis
ATTN: Code 2000, J. Brown
ATTN: Code 4700, S. Ossakow
ATTN: Code 4770, G. Cooperstein
ATTN: Code 4701, I. Vitokovitsky

Naval Surface Weapons Center
ATTN: Code R40
ATTN: Code F31
ATTN: Code F34

Naval Weapons Center
ATTN: Code 343, FKA6A2, Tech Svcs

DEPARTMENT OF THE AIR FORCE

Air Force Weapons Laboratory
ATTN: NTYP
ATTN: CA
ATTN: NT
ATTN: SUL

Ballistic Missile Office/DAA
ATTN: ENSN

Dep Ch of Staff, Rsch, Dev & Acq
ATTN: AFRDQI

Space Division
ATTN: XR
ATTN: YEZ
ATTN: YGJ
ATTN: YKF
ATTN: YKS, P. Stadler
ATTN: YKM
ATTN: YNV

Strategic Air Command
ATTN: XPFS
ATTN: DOTP

DEPARTMENT OF ENERGY

Department of Energy
Ofc of Military Application, GTN
Attention Ofc of Inert Fusion for
ATTN: C. Hilland
ATTN: T. Godlove
ATTN: S. Kahalas

OTHER GOVERNMENT AGENCY

Central Intelligence Agency
ATTN: OSWR/NED

DEPARTMENT OF ENERGY CONTRACTORS

University of California
Lawrence Livermore National Lab
ATTN: W. Pickles, L-401
ATTN: L-47, L. Wouters
ATTN: Tech Info Dept Library
ATTN: L-153
ATTN: L-13, D. Meeker
ATTN: L-545, J. Nuckolls, Class L-33

Los Alamos National Laboratory
ATTN: MS222, J. Brownell

Sandia National Laboratories
ATTN: M. Clauser, Org 5241
ATTN: G. Kuswa, Org 5240
ATTN: Tech Lib, 3141
ATTN: G. Yonas
ATTN: J. Powell
ATTN: Org 9336, D. Allen

PREVIOUS PAGE
IS BLANK

DEPARTMENT OF DEFENSE CONTRACTORS

Advanced Rsch & Applications Corp
ATTN: R. Armistead

Aerospace Corp
ATTN: Library Acquisition, M1/100
ATTN: V. Josephson
ATTN: S. Bower

BDM Corp
ATTN: Corporate Lib

BDM Corp
ATTN: L. Hoeft

Boeing Co
ATTN: Aerospace Library

Dikewood Corp
ATTN: Tech Lib for D. Pirio

EG&G Wash Analytical Svcs Ctr, Inc
ATTN: Library

General Electric Co
ATTN: J. Peden
ATTN: H. O'Donnell

IRT Corp
ATTN: R. Mertz

JAYCOR
ATTN: E. Wenaas

JAYCOR
ATTN: R. Sullivan
ATTN: E. Alcaraz
2 cys ATTN: J. Guillory
2 cys ATTN: R. Terry

Kaman Sciences Corp
ATTN: S. Face

Kaman Sciences Corp
ATTN: E. Conrad

Kaman Tempo
ATTN: DASIAC

Kaman Tempo
ATTN: DASIAC

Lockheed Missiles & Space Co, Inc
ATTN: L. Chase

Maxwell Labs, Inc
ATTN: A. Kolb
ATTN: O. Cole
ATTN: D. Tanimoto
ATTN: A. Miller

DEPARTMENT OF DEFENSE CONTRACTORS (Continued)

Lockheed Missiles & Space Co, Inc
ATTN: S. Taimuty, Dept 81-74/154

McDonnell Douglas Corp
ATTN: S. Schneider

Mission Research Corp
ATTN: C. Longmire

Mission Research Corp
ATTN: B. Godfrey

Mission Research Corp
ATTN: V. Van Lint

Pacific-Sierra Research Corp
ATTN: L. Schlessinger
ATTN: H. Borde, Chairman SAGE

Physics International Co
ATTN: C. Gilman
ATTN: G. Frazier
ATTN: C. Stallings

Pulse Sciences, Inc
ATTN: P. Spence
ATTN: I. Smith
ATTN: S. Putnom

R&D Associates
ATTN: P. Haas
ATTN: A. Latter

R&D Associates
ATTN: P. Turchi

Rand Corp
ATTN: P. Davis

Rand Corp
ATTN: B. Bennett

S-CUBED
ATTN: A. Wilson

Science Applications, Inc
ATTN: W. Chadsey
ATTN: M. Schmidt

Science Applications, Inc
ATTN: K. Sites

TRW Electronics & Defense Sector
ATTN: D. Clement
ATTN: Tech Info Center

END

FILMED

6-85

DTIC